

THERMOELECTRIC PROPERTIES OF NITRIDE AND OXIDE THIN FILMS FOR DEVICE APPLICATIONS

*Thesis submitted to the University of Calicut for the partial fulfillment of
the requirements for the award of the degree of*

Doctor of Philosophy in Physics
Under the Faculty of Science

by

MUHAMMED SABEER N.A.

Under the guidance of

Prof. Dr. P.P. PRADYUMNAN



**DEPARTMENT OF PHYSICS
UNIVERSITY OF CALICUT
KERALA-673635
INDIA**

September-2020



**Department of Physics
UNIVERSITY OF CALICUT**

Dr. P.P. Pradyumnan

Professor

Calicut University P.O

Kerala, India-673 635

Tel: +91 9895961751

Fax: +91494 2400269

E-mail: drpradyumnan@gmail.com

15th February, 2021

CERTIFICATION OF SUPERVISOR

This is to certify that all the corrections/suggestions recommended by the adjudicators have been incorporated in the thesis entitled 'Thermoelectric Properties of Nitride and Oxide Thin Films for Device Applications', submitted to the University of Calicut in partial fulfillment of the requirements for the award of the degree of Doctor of Philosophy in Physics by Mr. Muhammed Sabeer N. A., Department of Physics, University of Calicut and the contents in the thesis and the soft copy are one and the same.

Dr. P.P. Pradyumnan

**Prof. (Dr.) P.P. PRADYUMNAN
Professor
Department of Physics
University of Calicut
Kerala - 673635, India**



Department of Physics
UNIVERSITY OF CALICUT

Dr. P.P. Pradyumnan

Professor

Calicut University P.O

Kerala, India-673 635

Tel: +91 9895961751

Fax: +91494 2400269

E-mail: drpradyumnan@gmail.com

25th September, 2020

CERTIFICATE

Certified that the thesis entitled 'Thermoelectric Properties of Nitride and Oxide Thin Films for Device Applications' submitted to the University of Calicut in partial fulfillment of the requirements for the award of the degree of Doctor of Philosophy in Physics is a record of original research work done by Mr. Muhammed Sabeer N.A. during the period 2014-2020 of his research under my guidance in the Department of Physics, University of Calicut and the thesis has not formed the basis for the award of any Degree/Diploma and has undergone plagiarism check using URKUND software at CHMK Library, University of Calicut.

Dr. P.P. Pradyumnan

Prof. (Dr.) P.P. PRADYUMNAN

Professor

Department of Physics

University of Calicut

Kerala - 673635, India



**Department of Physics
UNIVERSITY OF CALICUT**

Dr. P.P. Pradyumnan

Professor

Calicut University P.O

Kerala, India-673 635

Tel: +91 9895961751

Fax: +91494 2400269

E-mail: drpradyumnan@gmail.com

15th February, 2021

CERTIFICATION OF SUPERVISOR

This is to certify that all the corrections/suggestions recommended by the adjudicators have been incorporated in the thesis entitled 'Thermoelectric Properties of Nitride and Oxide Thin Films for Device Applications', submitted to the University of Calicut in partial fulfillment of the requirements for the award of the degree of Doctor of Philosophy in Physics by Mr. Muhammed Sabeer N. A., Department of Physics, University of Calicut and the contents in the thesis and the soft copy are one and the same.

Dr. P.P. Pradyumnan

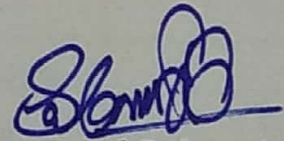
Prof. (Dr.) P.P. PRADYUMNAN
Professor
Department of Physics
University of Calicut
Kerala - 673635, India

DECLARATION

I, Muhammed Sabeer N.A., hereby declare that this dissertation work entitled 'Thermoelectric Properties of Nitride and Oxide Thin Films for Device Applications' submitted to the Department of Physics, University of Calicut is a record of the original work done by me under the guidance of Dr. P.P. Pradyumnan, Professor, Department of Physics, University of Calicut and this work has not been included in any other thesis submitted previously for the award of any degree.

Calicut University

25th September, 2020



Muhammed Sabeer N.A.

Dedicated to

My Family...

Acknowledgments

The tenure of my Ph.D. research is an amazing journey of my life and I would like to take this opportunity to express my special gratitude to everyone who rendered a helping hand for the successful realization of the thesis and also I would like to express my apology that I couldn't mention them personally.

First and foremost, with deep sense of gratitude, I express my heartfelt and sincere thanks to my guide and supervisor Dr. P.P. Pradyumnan, Professor, Department of Physics, University of Calicut, Kerala for his tremendous effort in guiding, helping and encouraging me during the course of my research. This thesis has been kept on track and been seen through to completion only with his expert guidance, fresh insights about experimental observations and eternal encouragement which will always be appreciated with wholeheartedly. I thankfully remember the way he supported throughout my years of study by patiently listening to me, forgiving my lapses and providing immense freedom to work.

I would like to extend my sincere gratitude to Dr. A.M. Vinodkumar, Professor & Head, Department of Physics, University of Calicut for his support and valuable suggestions especially the comments during departmental presentations.

I am extremely grateful to all the former H.O.Ds, Department of Physics, University of Calicut, Prof. (Dr.) Antony Joseph and Prof. (Dr.) M.M. Musthafa for providing support and for extending facilities to carry out my research work.

I am deeply indebted to the other faculty members of our department during the tenure of my Ph.D., Prof. (Dr.) Vishnu Mayya Bannur, Dr. C.D. Ravikumar, Dr. Libu K Alexander and Dr. Mohamed Shahin Thayyil for their love and friendly talks.

I wish to express my sincere gratitude to all non-teaching staff of the Department of Physics and Directorate of Research for their continuous support throughout the course of the research.

It's my fortune to gratefully acknowledge the support of some special individuals. With heartfelt gratitude and pleasure, I express my sincere thanks to my dear friends, Mr. Jemshihias A.P., Dr. Jaya T.P., Ms. Anju Paulson, Ms. Soumya C, Ms. Shabeeba P, Dr. Vidya Rajan and Muhammed Shan P.T. for their care, love and support.

I express my warm thanks to my 'mosque & tea team', Dr. Musammil N.M., Dr. Ahmed Raseen N, Abdul Irshad M, Vishnu V and Sebastian K who have made these years enjoyable and memorable.

With special mention, many thanks to my labmates and friends including seniors, Dr. T. Ramachandran, Dr. Binitha M.P, Dr. Divya, Dr. Jumanath E.C, Ms. Shyni P, Ms. Vineetha V.S., Ms. Nabeela K.V, Ms. Parvathy T, Mr. Hashir P, Mr. Midhun Shah and Ms. Jamshina Sanam, Dr. Bintu Thomas Ms. Anju K and Mr. Sravan Das for providing joyful working environment.

I am deeply indebted to CeNSE, IISc, Bengaluru, funded by the Ministry of Electronics and Information Technology (MeitY), Govt. of India, for providing hands-on training on many sophisticated techniques and accepting the proposal for executing major characterizations of the research work. I acknowledge the Central Sophisticated Instrumentation Facility (CSIF), University of Calicut and the technicians to provide characterization facilities for the research work. I wish to extend my sincere gratitude to Dr. S. Sindhu, Head, Department of Nano Science & Technology, University of Calicut and to the research scholars in the department for their support by providing characterization facilities.

I would like to acknowledge UGC-SAP and FIST2 (DST, Government of India), for providing the research facilities and DST SERB (Government of India) for providing the major research Project SB/EMEQ-002/2013 in the Department of Physics, University of Calicut.

I would like to acknowledge UGC (Government of India), for their supporting with JRF and SRF.

I express my warm thanks to the staff of Fortune Restaurant & Caterers, Hotel Alakapuri, Hotel Grand Arabian and S.R. Bakery for serving unadulterated food with love for several years.

With heartfelt gratitude, I remember my father, mother, brothers and their families who are my true strength and lifting me to this phase of life with endless love and encouragement throughout all the ups and downs in my life. Besides this, I extend my heartfelt gratitude to my son, wife and her father, mother and sisters for their love, consideration and adjustments in the short span of our togetherness.

Finally, I bow my head with reverence to God Almighty that has showered the blessings on me to get through the whole task of my Ph.D.

-Muhammed Sabeer N.A.-

Preface

The current and future global energy management system is mainly fuelled from depleting resources. The dependence of energy production on fossil fuels results in increasing environmental pollution and global warming. Hence, the energy system based on renewable resources is a key factor for healthy and quality life of population. Hence, high priority and support have been given by the researchers for the research and development of future promising renewable energy techniques. Thermoelectric energy conversion method is eco-friendly and sustainable technique for electrical power generation. Thermoelectric generators convert thermal energy into electricity using thermoelectric materials by means of solid state techniques. It can generate electricity by scavenging waste heat which is emitted to the environment during various energy processes.

The thesis entitled '*Thermoelectric Properties of Nitride and Oxide Thin Films for Device Applications*' deals with the transformation of earth abundant and non-toxic nitrides and oxide semiconductor thin films as efficient thermoelectric materials for device applications. The work focuses on the enhancement of thermoelectric power factor of n-type of tin nitride (Sn_3N_4) and zinc tin nitride (ZnSnN_2) and p-type of chromium nitride (CrN) and nickel oxide (NiO) thermoelectric materials by advanced techniques like band convergence, resonant levels, point defects and nanostructuring. Moreover, the fabrication and electrical characterization of the four TEGs of different couples of the thin film materials, (1) $\text{Sn}_3\text{N}_4/\text{CrN}$, (2) $\text{Sn}_3\text{N}_4/\text{NiO}$, (3) $\text{ZnSnN}_2/\text{CrN}$ and (4) $\text{ZnSnN}_2/\text{NiO}$ are discussed in detail to validate the thermoelectric properties of the thin films and stable output power of the devices made up of these thin films. The thesis comprises eight chapters; the division of the chapters with a brief outline of the contents is as follows.

The critical role of promising renewable energy techniques in view of the latest trends in global energy management system and its environmental impacts are pointed out in chapter 1 of the thesis. An overview of the history and fundamental physics behind thermoelectrics is included in this chapter along with an introduction to the state of the art thermoelectric materials and devices for power generation. The motivation and objectives of the research work carried out are also described.

Chapter 2 deals with the various aspects of reactive radio frequency magnetron sputtering which is the deposition technique used to fabricate the thin films in this study. It also discusses the nucleation and growth of crystallites and the optimization of fabrication parameters of thin films, since these parameters have great influence on physical properties of the thin films. The characterization techniques which are employed to analyze the crystallographic, microstructural, surface, optical and microscopic transport parameter features are briefly mentioned. The analysis of thermoelectric properties by ULVAC-ZEM3 (M8) and the evaluation of output power characteristics of thermoelectric generators are also described.

In chapter 3, the enhancement of thermoelectric power factor of tin nitride (Sn_3N_4) thin films by conduction band convergence is reported. It discusses the experimental strategy to precisely tune the defect chemistry and growth kinetics of crystallites of the thin films for the optimization of bandgap and preferred orientation respectively. These concurrent variations gradually converge the conduction bands in accordance with bandgap reduction. These features of band evolution were explored by merging the optical analyses with thermoelectric transport parameters. In addition to this, various characterization results which are employed to explore the physical aspects behind the correlation between thermoelectric properties and band parameters are also reported.

The investigation on the formation of resonant energy states in the zinc tin nitride (ZnSnN_2) thin films by intrinsic point defects instead of conventional resonant impurity doping to enhance the thermoelectric power factor is reported in chapter 4. This is the first attempt ever in resonant level scheme, formation of resonant energy states in the conduction band by intrinsic point defects instead of resonant impurity doping. The positioning of the Fermi level and resonant states independently with respect to conduction band minimum to achieve maximum benefit from resonant levels for an enhanced thermoelectric power factor is the core aspect of the study. Moreover, it point out the advantages of formation of resonant states in the conduction band by intrinsic defect strategy instead of resonant elemental doping. Hence, the defect chemistry of ZnSnN_2 opens a new window into resonant level induced thermoelectrics. It also discusses the method to ensure the presence of point defect

induced resonant energy levels in the conduction band of a material by electronic spectrum.

In chapter 5, the transformation of the type of conductivity of chromium nitride (CrN) thin film by inducing metal vacancy point defects is described in detail. The formation and optimization of Cr vacancies and N antisites acceptor point defects transform the n-type conductivity of CrN to p-type by controlling the growth kinetics during the thin film deposition. The improvisation of the p-type conductivity and hence the thermoelectric power factor by changing the orientation of the crystallites are also discussed. Also, the remarkable increase in the spread of the charge carriers in each particle which is the root cause behind the improvement in conductivity of CrN thin films with orientation of crystallites along (220) plane was explored by surface charge density mapping.

The strategy of nanostructuring for the concurrent enhancement of thermoelectric power factor and optical bandgap of nickel oxide (NiO) thin films is described in chapter 6. It discusses the fabrication of NiO thin films having nanoparticles and the optimization of its size to transform the thin films as an efficient wide bandgap thermoelectric material. The transformation of the energy band structure as a result of the quantum confinement effect originated from reduced particle size and its effect on the physical properties of the NiO thin films are also explored.

To ensure the energy conversion performance of the investigated n- and p-type thin films in a device form, the electrical characterizations of TEGs made up of different couples of these materials are necessary. Chapter 7 describes the fabrication and electrical characterizations of four thermoelectric generators; (1) $\text{Sn}_3\text{N}_4/\text{CrN}$, (2) $\text{Sn}_3\text{N}_4/\text{NiO}$, (3) $\text{ZnSnN}_2/\text{CrN}$ and (4) $\text{ZnSnN}_2/\text{NiO}$ made up of different couples of the thin film leg materials which have been already discussed in the previous chapters. The electrical characterizations comprises the evaluation of the dependence of temperature gradient on output power of the devices by estimating the open circuit voltage and short circuit current by varying the temperature difference across the TEGs and the estimation of device operating voltage and operating power as a function of electrical current at matched load by varying the external load resistance.

Hence, it validates the thermoelectric properties of the individual n- and p-type thin films and the energy conversion capability of the devices.

Finally, chapter 8 presents a summary of the important results and conclusions of the whole research conducted on nitride and oxide thin films for thermoelectric device applications. It also provides a precise direction for the future research works on the present investigations.

* * * * *

Research Publications

1. **N.A. Muhammed Sabeer**, Anju Paulson, P.P. Pradyumnan, *Band modification of tin nitride thin films for green energy generation*, J. Phys. Chem. Solids. 138 (2020) 109294.
2. **N.A. Muhammed Sabeer**, Anju Paulson, P.P. Pradyumnan, *Doubling the thermoelectric power factor of earth abundant tin nitride thin films through tuned (311) orientation by magnetron sputtering*, J. Appl. Phys. 124 (2018) 185107.
3. **Muhammed Sabeer N.A.**, Anju Paulson, P.P. Pradyumnan, *An experimental approach of decoupling Seebeck coefficient and electrical resistivity*, AIP Conf. Proc. 1942 (2018) 110054.
4. Anju Paulson, **N.A. Muhammed Sabeer**, P.P. Pradyumnan, *Enhancement of optical and thermoelectric properties in dysprosium doped ZnO thin films as an impact of non-parabolic band structure*, Mater. Sci. Eng. B 262 (2020) 114745.
5. Anju Paulson, **N.A. Muhammed Sabeer**, P.P. Pradyumnan, *A synergetic approach of band gap engineering and reduced lattice thermal conductivity for the enhanced thermoelectric property in Dy ion doped ZnO*, J. Alloys Compd. 786 (2019) 581–587.
6. Anju Paulson, **N.A. Muhammed Sabeer**, P.P. Pradyumnan, *Enhanced thermoelectric property of oxygen deficient nickel doped SnO₂ for high temperature application*, Mater. Res. Express. 5 (2018) 045511.
7. P. Maneesha, Anju Paulson, **N.A. Muhammed Sabeer**, P.P. Pradyumnan, *Thermoelectric measurement of nanocrystalline cobalt doped copper sulfide for energy generation*, Mater. Lett. 225 (2018) 57-61.
8. P.P. Pradyumnan, Anju Paulson, and **Muhammed Sabeer N.A.**, *Cobalt doped SnO₂: A new material for thermoelectric applications*, Adv. Mater. Proc. 3 (2018) 8-12.
9. P.P. Pradyumnan, Anju Paulson, **Muhammed Sabeer N.A.**, and N. Deepthy, *Enhanced power factor in Ho³⁺ doped ZnO: A new material for thermoelectric applications*, AIP Conf. Proc. 1832, (2017) 110055.

Research Papers Communicated

1. **N.A. Muhammed Sabeer**, Anju Paulson, P.P. Pradyumnan, *ZnSnN₂/NiO thermoelectric power generator: Effect of point defect induced resonant levels, Physical Review Applied.* (Under Review)
2. **N.A. Muhammed Sabeer**, P.P. Pradyumnan, *Augmentation of thermoelectric power factor of p-type chromium nitride thin films for device applications, Material Science & Engineering B.* (Under Review)

Paper Presented Conferences

1. **Solid State Physics Symposium** organized by *Department of Atomic Energy-Govt. of India* held at Bhabha Atomic Research Centre, Mumbai on December-2017.
2. **International Conference on Thin Films** organized by *Indian Vacuum Society* held at CSIR-National Physical Laboratory, New Delhi on November-2017.
3. **International Conference on Advances in Functional Materials** organised by *UGC-India & University of Oslo-Norway* held at Anna University, Chennai on January-2017.
4. **International Conference on Material Science and Technology** organised by *International Association of Advanced Materials-Sweden* held at University of Delhi, New Delhi on March, 2016.
5. **International Conference on Recent Trends in Physics** organised by *Department of Physics* held at *Govt. College, Kodanchery* on January-2015.
6. **National Seminar on Science & Technology for New Materials for Sustainable Future** organised by *Department of Physics* held at *University of Calicut, Calicut* on February-2018.
7. **National Conference on Modern Optics & Material Science** organised by *Department of Physics* held at *Farook College, Calicut* on December-2015.

Contents

Chapter 1. Thermoelectrics

1.1	Introduction.....	2
1.2	Thermoelectrics: History and physics.....	4
1.3	The Seebeck effect for power generation-Fundamental principles.....	7
1.4	Thermoelectric materials.....	11
1.5	Thermoelectric devices.....	13
1.6	Motivation and objectives of the thesis	15
	References.....	16

Chapter 2. Thin Film Deposition and Characterization Techniques

2.1	Introduction.....	19
2.2	Fabrication of thin films.....	19
2.2.1	The thin film deposition techniques.....	19
2.2.2	Sputtering.....	20
2.2.2.1	Reactive radio frequency magnetron sputtering.....	22
2.2.2.2	Growth kinetics of thin films.....	23
2.2.2.3	Optimization of sputtering parameters.....	25
2.2.3	Factors considered to select the deposition technique.....	28
2.3	Characterization techniques.....	30
2.3.1	X-ray diffraction.....	30
2.3.1.1	Instrumentation.....	31
2.3.2	Atomic force microscopy.....	33
2.3.2.1	Instrumentation.....	34
2.3.3	Hall measurement.....	36
2.3.3.1	Instrumentation.....	37
2.3.4	UV-Visible spectroscopy.....	37
2.3.4.1	Instrumentation.....	39
2.3.5	Thermoelectric measurement.....	40

2.3.5.1	Instrumentation	41
2.3.6	Thermoelectric generator characteristics.....	43
2.3.6.1	Instrumentation	43
	References.....	44

Chapter 3. Enhancement of Thermoelectric Properties of Tin Nitride Thin Films by Band Convergence

3.1	Introduction	47
3.2	Fabrication of preferentially oriented Sn ₃ N ₄ thin films.....	50
3.3	Results.....	51
3.3.1	Phase and crystallographic features.....	51
3.3.2	Electronic transport parameters	55
3.3.3	Thermoelectric properties	56
3.3.4	Surface features	58
3.3.5	Optical properties	61
3.4	Discussion.....	64
3.5	Conclusion.....	68
	References.....	69

Chapter 4. Effect of Point Defect Induced Resonant Levels Thermoelectric properties of Zinc Tin Nitride Thin Films

4.1	Introduction.....	72
4.2	Fabrication of ZnSnN ₂ thin films	75
4.3	Results.....	76
4.3.1	Phase and crystallographic features.....	76
4.3.2	Thickness.....	77
4.3.3	Surface features	78
4.3.4	Electronic transport parameters	80
4.3.5	Thermoelectric properties	81
4.3.6	Optical properties	82
4.4	Discussion.....	83
4.5	Conclusion.....	87
	References.....	87

Chapter 5. Augmentation of p-Type Conductivity of Chromium Nitride Thin Films for Device Applications

5.1	Introduction.....	91
5.2	Fabrication of CrN thin films.....	93
5.3	Results.....	94
5.3.1	Phase and crystallographic features.....	94
5.3.2	Thickness.....	95
5.3.3	Surface features	96
5.3.4	Electronic transport parameters	98
5.3.5	Thermoelectric properties	101
5.4	Discussion.....	103
5.5	Conclusion.....	109
	References.....	110

Chapter 6. Nanocrystalline NiO Thin Films: A p-type Thermoelectric Material with Wide Bandgap

6.1	Introduction.....	113
6.2	Fabrication of nanocrystalline NiO thin films	115
6.3	Results.....	116
6.3.1	Phase and crystallographic features.....	116
6.3.2	Thickness.....	116
6.3.3	Surface features	117
6.3.4	Thermoelectric properties	121
6.3.5	Surface charge distribution.....	122
6.3.6	Optical properties	124
6.4	Discussion.....	125
6.5	Conclusion.....	128
	References.....	128

Chapter 7. Thin Film Thermoelectric Generators

7.1	Introduction.....	131
7.2	Fabrication and characterization of thin film thermoelectric generators.....	131

7.3	Results and discussion.....	133
7.3.1	Electrical characteristics with temperature gradient.....	133
7.3.2	Electrical characteristics with load resistance.....	136
7.4	Conclusion.....	138
	References.....	138

Chapter 8. Summary and Future Scope

8.1	Introduction.....	141
8.2	Summary of the thesis	141
8.2.1	Investigations of n-type thermoelectric thin films.....	142
8.2.2	Investigations of p-type thermoelectric thin films.....	143
8.2.3	Thermoelectric generator characteristics.....	145
8.3	Future scope	146
	References.....	147

List of Figures

1.1	Thomas Johann Seebeck (1770-1831) and the experimental setup used to observe the deflection of magnetic needle due to temperature gradient.....	4
1.2	Heinrich Gustav Magnus (1802-1870) and the schematic representation of the thermoelectric open circuit voltage.....	5
1.3	Jean Charles Athanase Peltier (1785-1845) and the schematic representation of the thermoelectric refrigeration.....	6
1.4	Lord Kelvin (1824-1907) and the schematic representation of Thomson effect.....	6
1.5	The optimized carrier concentration for highest power factor.....	8
1.6	The figure of merit of the state of the art thermoelectric materials.....	11
1.7	The Seebeck effect for power generation in (a) a thermoelectric couple (b) serially connected thermoelectric couples and (c) a thermoelectric module.....	14
2.1	Classification of thin film deposition techniques.....	20
2.2	Basic sputtering processes.....	21
2.3	The layer by layer growth under Frank-van der Merwe mode.....	23
2.4	The island growth under Volmer-Weber mode.....	24
2.5	The layer by layer followed island growth under Stransky-Krastanov mode.....	24
2.6	The RF magnetron sputtering system.....	29
2.7	The schematic interpretation of Bragg reflection.....	31
2.8	Bragg-Brentano geometry of XRD instrumentation.....	32
2.9	Rigaku-MiniFlex 600 X-ray diffractometer.....	32
2.10	Schematic representation of CAFM.....	35
2.11	The schematic representation of Hall effect.....	36
2.12	Schematic representation of (a) transmittance and (b) reflectance configurations of UV-Vis spectrophotometer.....	40
2.13	(a) The schematic representation of probe configuration used in (b)	

	ULVAC ZEM-3 thermoelctric measurement system.....	42
2.14	The electrical characterization system for thin film thermoelectric generators.....	44
3.1	Crystal structure of Sn ₃ N ₄ compound.....	48
3.2	XRD of sputtered Sn ₃ N ₄ thin films with PO.....	52
3.3	Texture Coefficient of Sn ₃ N ₄ thin films with reference to (a) ICDD file (b) XRD data of thin film sputtered at 4x10 ⁻² mbar.....	53
3.4	Variation of preferred orientation of Sn ₃ N ₄ thin film with the energy of bombarding particles.....	54
3.5	Variation of carrier concentration and mobility of Sn ₃ N ₄ thin films with N ₂ gas pressure.....	56
3.6	Temperature dependent (a) resistivity (b) Seebeck coefficient and (c) power factor of Sn ₃ N ₄ thin films.....	57
3.7	(a) Surface topography and (b) thickness analysis of the partially coated Sn ₃ N ₄ thin film.....	58
3.8	AFM 3D images of sputtered Sn ₃ N ₄ thin films with average surface roughness.....	58
3.9	Transmittance and reflectance of spectra of Sn ₃ N ₄ thin films as functions of the wavelength.....	62
3.10	Refractive index of Sn ₃ N ₄ thin films as a function of wavelength.....	62
3.11	The variation of optical absorption coefficient of Sn ₃ N ₄ thin films with incident wavelength.....	63
3.12	The variation of optical bandgap of Sn ₃ N ₄ thin films with N ₂ gas pressure.....	63
3.13	The variation of conductivity and Seebeck coefficient of Sn ₃ N ₄ thin films with bandgap.....	65
3.14	The variation of effective mass of Sn ₃ N ₄ thin films with bandgap.....	66
3.15	The schematic representation of conduction band convergence.....	67
4.1	Crystal structure of ZnSnN ₂ compound.....	73
4.2	The resonant energy levels in a conduction band of an n-type material..	74
4.3	XRD of ZnSnN ₂ thin films sputtered with different nitrogen partial pressure.....	77

4.4	(a) Surface topography and (b) step parameters of partially masked ZnSnN ₂ thin film.....	78
4.5	AFM surface profile of ZnSnN ₂ thin films with average surface roughness.....	79
4.6	Variation of carrier concentration and mobility of ZnSnN ₂ thin films with N ₂ gas pressure.....	80
4.7	The variation of temperature dependant (a) resistivity, (b) Seebeck coefficient and (c) power factor of ZnSnN ₂ thin films with nitrogen partial pressure.....	82
4.8	Transmittance and reflectance spectra of ZnSnN ₂ thin films as functions of wavelength.....	83
4.9	(a) The variation of bandgap with nitrogen partial pressure and (b) the Burstein-Moss shift in the optical bandgap of ZnSnN ₂ thin films having resonant energy levels.....	86
5.1	Crystal structure of CrN compound.....	91
5.2	XRD of sputtered CrN thin films with PO.....	95
5.3	(a) Surface topography and (b) step parameters of partially coated CrN thin film.....	96
5.4	CAFM topography of CrN thin films with average Surface roughness	97
5.5	Variation of carrier concentration and mobility of CrN thin films with N ₂ gas pressure.....	99
5.6	CAFM 3D current distribution profile of CrN thin films.....	100
5.7	Temperature dependent (a) resistivity (b) Seebeck coefficient and (c) power factor of CrN thin films.....	102
5.8	XRD of sputtered CrN thin films with (220) PO.....	105
5.9	CAFM 2D images of topographic (a & e) and current distribution (other than a & e) profile of CrN thin films with (200) PO (first column) and (220) PO (second column)	107
5.10	CAFM current distribution profile of a particle of CrN thin films with (200) PO (first column) and (220) PO (second column)	108
6.1	Crystal structure of NiO compound.....	113
6.2	XRD of sputtered nanocrystalline NiO thin films.....	116

6.3	(a) Surface topography and (b) step parameters of partially coated NiO thin film.....	117
6.4	AFM 3D (left) and 2D (right) topography of NiO thin films with average surface roughness.....	119
6.5	AFM 2D grain distribution (left) and grain length and volume histograms (right) of NiO thin films with substrate temperature.....	121
6.6	Temperature dependent (a) resistivity and (b) Seebeck coefficient of NiO thin films.....	122
6.7	CAFM 3D current distribution profile of NiO thin films.....	124
6.8	Transmittance and reflectance of spectra of NiO thin films as functions of wavelength.....	125
6.9	Temperature dependent power factor of NiO thin films.....	126
6.10	The variation of bandgap of NiO thin films with substrate temperature.....	126
7.1	The schematic representation of prototype thin film thermoelectric generator.....	132
7.2	The variation of open circuit voltage and short circuit current with temperature gradient of TEGs.....	134
7.3	The variation of output power of TEGs with temperature gradient.....	135
7.4	The electrical equivalent circuit of a TEG.....	136
7.5	The variation of operating voltage and power of TEGs with circuit current.....	137

List of Tables

3.1	The optimized deposition parameters for Sn ₃ N ₄ reactive sputtering.....	50
3.2	Optical and electronic transport parameters at RT of Sn ₃ N ₄ thin films sputtered with different N ₂ gas pressures.....	66
4.1	The optimized deposition parameters for ZnSnN ₂ reactive sputtering....	76
4.2	Optical and electronic transport parameters of ZnSnN ₂ thin films sputtered at various nitrogen partial pressures	85
5.1	Deposition parameters optimized for CrN reactive sputtering.....	94
5.2	Thermoelectric parameters of CrN thin films at RT sputtered with various N ₂ pressures.....	104
5.3	The TE parameters of CrN thin films at RT with different PO.....	106
6.1	Deposition parameters optimized for NiO reactive sputtering	115
7.1	The sputtering parameters of p-type and n-type thin films as thermoelectric legs for the fabrication of TEGs	132
7.2	The maximum V_{OC} , I_{SC} , P_{OUT} and P_{MAX} of TEGs at a temperature gradient of 200°C	136

THERMOELECTRICS

Contents

-
- 1.1 Introduction
 - 1.2 Thermoelectrics: history and physics
 - 1.3 The Seebeck effect for power generation
 - 1.4 Thermoelectric materials
 - 1.5 Thermoelectric devices
 - 1.6 Motivation and objectives of the thesis
-

This chapter outlines the history and fundamental physics behind thermoelectrics. It presents an introduction to thermoelectric materials and devices for power generation. The motivation and objectives of the research work carried out are also described.

1.1 Introduction

Energy is one of the most important factors in human development and hence acts as central pillar of the socio-economic development of a country. The energy consumption per capita is considered as one of the indicators of development progress of a country. According to the energy reports 2019 of International Energy Agency (IEA), the rising incomes and human population increases the global energy demand by more than 25% to 2040. The energy requirement of the developing economies in Asia, led by India will be doubled at 2040 by increasing from 20% of the total global energy demand to 40% [1,2]. Since the fossil fuels accounted for 81% of the total global energy production with an annual average growth rate of 2.2%, the increasing demand of energy leads to the production and consumption of huge amount of fossil fuels. The consumption of fossil fuels is responsible for various issues such as environmental pollution, global warming, etc., which adversely affect the health and quality of life of population [3,4]. As per the statistical report of carbon dioxide emissions 2019 by IEA, global energy related carbon dioxide emission started to rise resulting in a 1.6% increase in annual average after showing a three years of stable emission of 2.1 %. India registered annual carbon dioxide emission growth rate of above 4% [5]. Moreover, the fuel mining related environmental challenges include mining accidents, land subsidence, damage to water and air environment and mining waste disposal [6]. The energy related issues continuous to result in millions of premature deaths each year. This situation will become more worst if we do not address energy security and sustainability concerns globally [7,8].

The harness of energy from various renewable resources for different needs is possible by using advanced technologies. Since the renewable energy resources are sustainable, abundant and environmental friendly, the world is gradually building a different kind of energy management system by placing renewable energy generation techniques as the key pillars [9]. The biofuels is the largest renewable energy source, representing the 68% of global renewable energy supply. The second largest source, hydro power provides 18.5% and the remaining share of the renewables is furnished by wind, geothermal, solar and tidal energy systems. The global renewable energy production increasing in each year but still accounted for 13.5% of total global primary energy production. Among the renewable energies, the solar photovoltaics shows highest annual average change in global production of +35% [10]. When considering

the status of our country, India, remarkable progress has been achieved in its energy sustainability. According to 2018 climatescope report, India ranked second among the emerging economies which lead to transition to clean energy. India is ranked 5th in installed solar photovoltaics and renewable power as of 2018. As of June 2019, the installed renewable energy capacity is 80 GW in which solar comprises 30 GW. The government of India aims to achieve 175 GW of installed renewable energy by 2022, which includes 100 GW of solar power [11].

From the above data the current and future energy management status is very clear. Most of the energy generation techniques are fuelled by unsustainable resources and raising environmental issues. The continuing effort to improve the energy efficiency and the convergence of cheaper renewable energy technologies are the central solutions to overcome these challenges. Hence considerable motivation has to be given for the utilization of sustainable resources for energy production and the green energy conversion techniques. Moreover, high priority and support to be given for the research and development of future promising renewable energy techniques like thermoelectrics and photovoltaics [12,13].

The studies revealed that 63% of global primary consumption is lost during energy conversion and processing in which electricity generation has the largest share followed by transportation and industry [14]. The waste heat causes for the increased impact of green house gases and global warming. Also, it significantly exacerbates the efficiency of the systems. In this context, conversion of this waste heat into electrical energy supplement to improve the efficiency of the systems as well as to reduce the utility of conventional fuels. One of the efficient techniques among various methods to scavenge waste heat into electricity is thermoelectrics. It is an eco-friendly and sustainable technique, hence attracted significant interest in power generation. Moreover, the thermoelectrics greatly supplements to reduce environmental pollution, since it utilizes waste heat as the input fuel [15].

The application and commercialization of thermoelectric energy generation technique are distinct from that of photovoltaics and other renewable energy conversion methods. The commercial interest and investment in thermoelectrics is far behind that of photovoltaics [16]. The reliability and reproducibility of the performance of thermoelectric prototype devices are the major hurdles in the commercialization of this technology. Further, the environmental stability of the

conversion material during the operation at high temperatures limited its widespread applications. However, the thermoelectric energy conversion technique has wide range of applications as standalone power generators from waste heat. It is used on vehicles for generating electricity from waste heat to improve overall engine efficiency. It has been used for the power in miniaturized devices such as sensors, mobile phones, watches, pacemakers, etc. Radioisotope thermoelectric generators are used as power sources in satellites and space probes. Among the various ways to commercialize this technology, automotive industry would be the biggest market. The application of the technology in automotive industry not only improves the efficiency of the vehicles but also gives a strong support to achieve clean energy mission [17]. As per a NITI Aayog proposal, India intended to almost completely switch the transport sector in to electric by 2030 to reduce the polluting oil consumption. In this scenario, thermoelectric generators have great role in the development of a country having strong view about clean energy mission.

1.2 Thermoelectrics: History and physics

In 1821, the Estonian physicist Thomas Seebeck found that a system made by two dissimilar metal junctions with a temperature gradient would deflect the magnetic compass. He used an experimental setup as shown in fig. 1.1 to observe the deflection of magnetic needle due to temperature gradient exist between the junctions of two dissimilar metals. In the experimental setup, *op* is a base strip made up of bismuth, *mn*

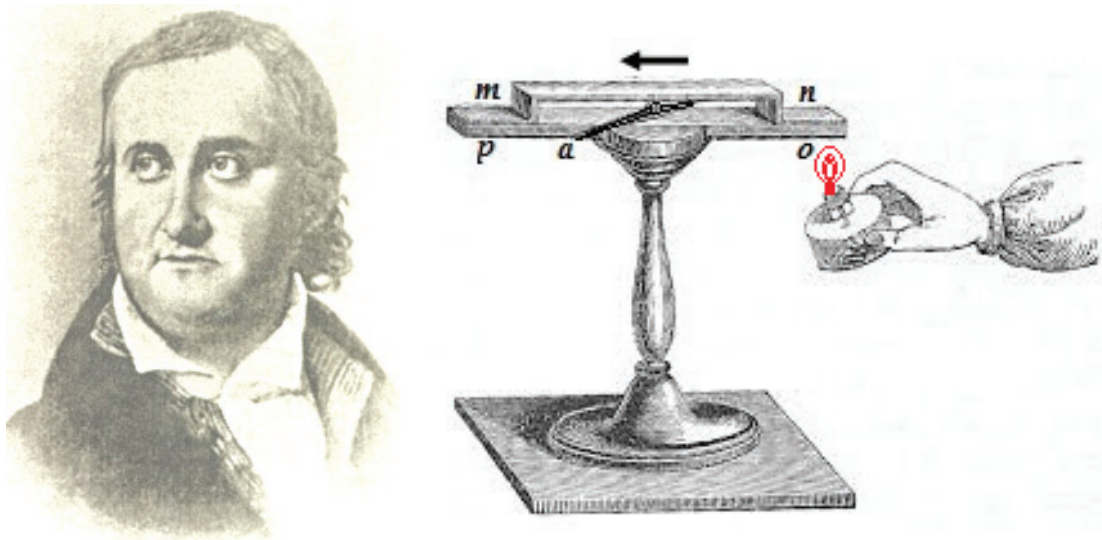


FIGURE 1.1. Thomas Johann Seebeck (1770-1831) and the experimental setup used to observe the deflection of magnetic needle due to temperature gradient

is an arc made up of copper and a is a magnetic needle. He attributed the phenomenon to magnetism induced by the temperature gradient exist between the junctions. But, the interpretation was wrong and later it was realized that the temperature gradient generates an electric potential which drives the electric current through the closed loop. Even though he interpreted the phenomenon incorrectly, after the discovery of thermoelectricity and thermocouple, he was honored with the discovery and named Seebeck effect after him [18].

The generation of a voltage across the two junctions made up of a pair of dissimilar metals when a temperature gradient exists between the junctions is known as Seebeck effect. The generated voltage is proportional to the temperature gradient exists between the two junctions. The proportionality constant is known as Seebeck coefficient and often referred as thermopower. In 1851, German experimental scientist, Gustav Magnus discovered that the voltage produced by Seebeck effect does not depend on the temperature distribution along the metals between the junctions, instead, it is a function related with the thermodynamic state of the system. In fig. 1.2, a temperature gradient exists across the two junctions of a dissimilar metals ‘A and B’, then the potential difference between the open terminals is directly proportional to the temperature difference between the hot and cold junctions. This is the physical basis of the temperature measurement by thermocouple [19].

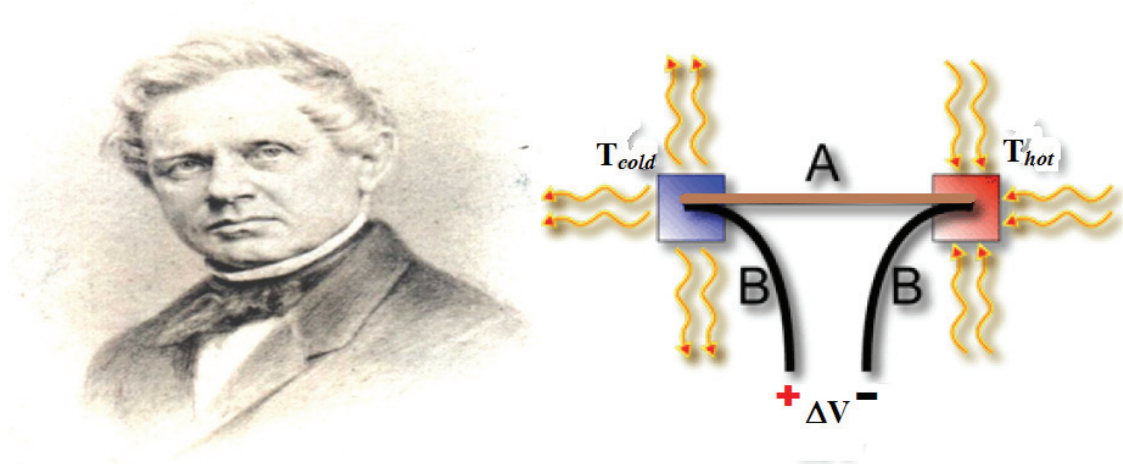


FIGURE 1.2. Heinrich Gustav Magnus (1802-1870) and the schematic representation of the thermoelectric open circuit voltage

In 1831, Jean Peltier, the French physicist found that electrical current can produce heating or cooling with the aid of two junctions made up of two dissimilar metals. The Peltier effect is the basis of thermoelectric refrigeration. In 1838, Lenz

showed that the heating and cooling at the junctions depending on the direction of current flow through the metals as shown in fig. 1.3. Also, the heat absorbed or generated at the junctions is proportional to the strength of the electric current. The proportionality constant is known as Peltier coefficient [20].

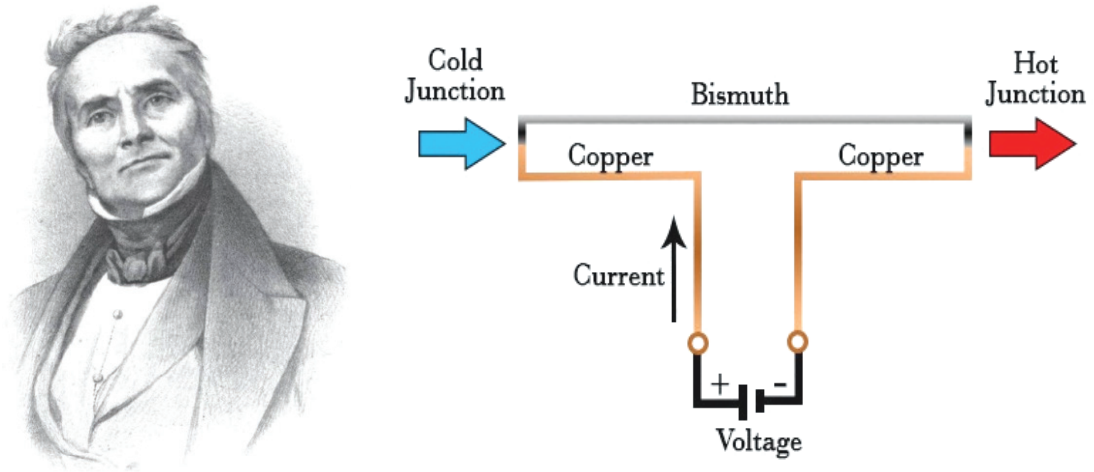


FIGURE 1.3. Jean Charles Athanase Peltier (1785-1845) and the schematic representation of the thermoelectric refrigeration

In 1851, Lord Kelvin (William Thomson) described the interrelationship between the Seebeck and Peltier effects through thermodynamics. The relation, Peltier coefficient is equal to the product of Seebeck coefficient and absolute temperature led to the prediction of third thermoelectric effect, known as Thomson effect. As shown in fig. 1.4, the heat is absorbed or generated in a material with a temperature gradient when an electric current is flowing through it and the heat is proportional to both the electric current and temperature difference and the constant of proportionality is known as Thomson coefficient [20].

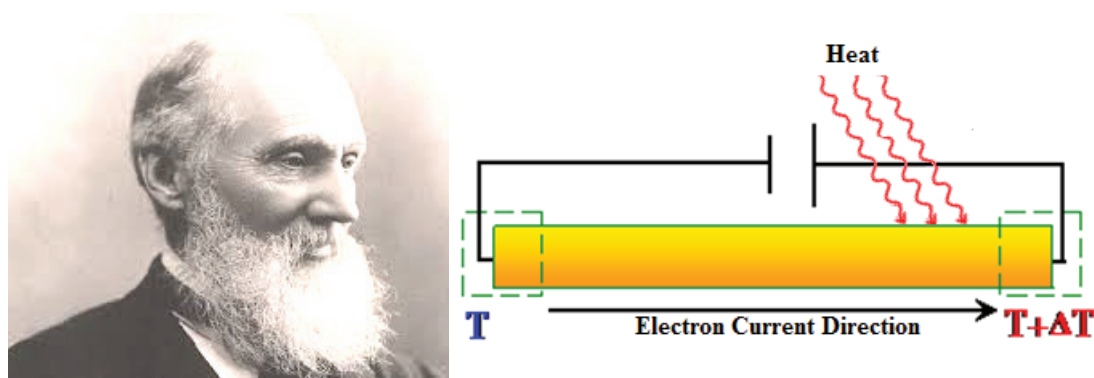


FIGURE 1.4. Lord Kelvin (1824-1907) and the schematic representation of Thomson effect

1.3 The Seebeck effect for power generation-Fundamental principles

Thermoelectrics has attracted significant interest in power generation by scavenging the waste heat to electricity using solid state devices made up of efficient semiconductor materials [21]. A temperature gradient exists over an electrically conductive material; there is a net diffusion of electrons from the hot end towards the cold end or vice versa. It generates an electric field and in equilibrium, this field causes a voltage over the material. This Seebeck voltage is much larger in semiconductors than in metals [22]. The net direction of electron diffusion depends on the difference of Fermi function of cold side of the material from that of hot side and the density of states of the material. The difference between the Fermi functions is positive above the Fermi level and it is negative below the Fermi level. In n-type materials, the density of states increases with energy and it decreases in p-type materials. These differences in the material band parameters impart a net electron diffusion from hot to cold for n-type materials and that from cold to hot for p-type materials. Hence the sign of the Seebeck coefficient is negative for n-type and that is positive for p-type materials [23]. In 1909, Edmund Altenkirch introduced the concept of figure of merit to estimate the efficiency of a thermoelectric generator. ZT , the thermoelectric figure of merit, is a dimensionless quantity, used to estimate the performance of a thermoelectric material and qualifies its application in the field of TE generation. It is defined as, $ZT = S^2\sigma T/\kappa$, where S [V/K] is the Seebeck coefficient (also called as thermo power), σ [S/m] is the electrical conductivity, ($S^2\sigma$ is referred to as the power factor), κ [W/m K] is the total thermal conductivity of the material ($\kappa = \kappa_l + \kappa_e$; the lattice and electronic contributions respectively) and T is the absolute temperature as given below [24].

$$ZT = \frac{S^2 \sigma T}{\kappa}$$

The diagram shows the equation $ZT = \frac{S^2 \sigma T}{\kappa}$ with red arrows pointing to labels for each part:

- ZT is labeled as "Figure of merit".
- S is labeled as "Seebeck coefficient".
- $S^2 \sigma$ is labeled as "Power factor".
- T is labeled as "Absolute temperature".
- κ is labeled as "Thermal conductivity".

The efficiency of a TE generator can be estimated based on ZT . The power generation efficiency reaches about 10 % at $ZT = 1$, hence the materials with $ZT \geq 1$ are desirable for the application of TE devices. The materials which show good electrical conductivity and low thermal conductivity with increasing temperature considered as good TE materials. According to Wiedemann-Franz law, electrical resistivity and thermal conductivity are co-responsive to temperature changes, which confine the good TE materials in semiconductor regime [25]. The effort to enhance power factor or to reduce thermal conductivity, both will lead to the improvement in the figure of merit of the material. The fundamental challenge of designing high efficient thermoelectric materials is the strong correlation of S , σ , and κ through carrier concentration (n). The electronic part of the total thermal conductivity has direct dependence on n . The large S is usually found in semiconductors with low n , and with increasing n , S drops significantly. But, to ensure large σ , n should be high. So, the maximum power factor, $S^2\sigma$ of an efficient thermoelectric material lies in a precise carrier concentration range of a balanced S and σ as shown in fig. 1.5 [26].

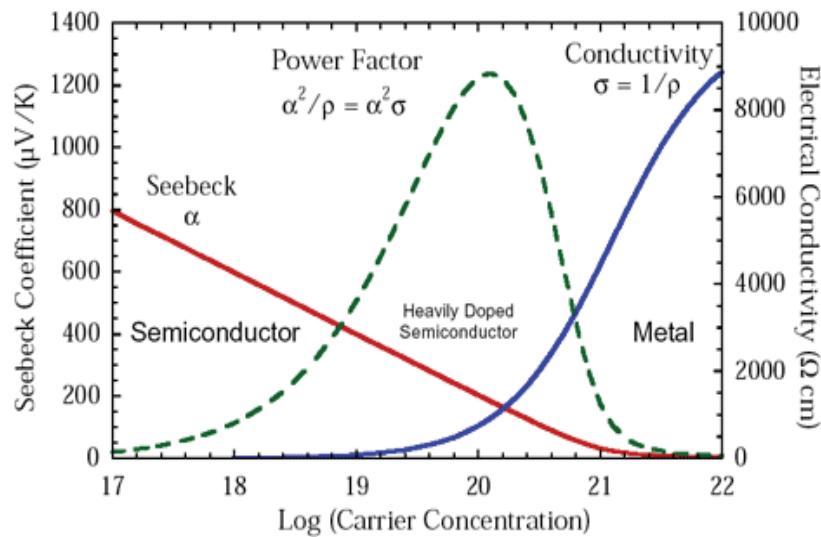


FIGURE 1.5. The optimized carrier concentration for highest power factor

TE transport parameters are often evaluated by solving the Boltzmann transport equation (BTE) [27]. The Landauer formalism, an alternative approach, has been widely applied for mesoscopic thermoelectric studies. It can also be used for macroscopic thermoelectrics [28]. The advantage of the application of Landauer approach includes providing a clear physical interpretation about TE parameters and

conventional results. Also, it provides a convenient way to explain the relationship between various material parameters and TE properties.

According to Landauer formalism, the electrical conductivity is expressed as,

$$\sigma(E) = \frac{2q^2}{h} \int_{-\infty}^{+\infty} T(E)M(E) \left(-\frac{\partial f_0}{\partial E}\right) dE \quad \dots\dots\dots (1.1)$$

where, q is the electron charge, h is the Planck constant and f_0 is the equilibrium Fermi-Dirac distribution [29].

The transmission, $T(E)$ is closely associated with scattering,

$$T(E) = \frac{\lambda(E)}{(\lambda(E)+L)} \approx \frac{\lambda(E)}{L} \quad \dots\dots\dots (1.2)$$

where, $\lambda(E)$ is the energy dependent mean free path and L is the length of the conductor.

In case of 2D materials like thin films,

$$\lambda(E) = (\pi/2) \vartheta(E)\tau(E) \quad \dots\dots\dots (1.3)$$

where, $\vartheta(E)$ is the carrier velocity and $\tau(E)$ is the momentum relaxation time [29].

Also, the number of conducting channels at energy, E in 2D materials,

$$M_{2D}(E) = W \frac{\sqrt{2m^*(E-\varepsilon_1)}}{\pi h} \quad \dots\dots\dots (1.4)$$

where, m^* is the electron effective mass and ε_1 is the bottom of the conduction band and W is the width of the 2D conductor [30].

Also, Seebeck coefficient is expressed as,

$$S = \left(\frac{k_B}{-q}\right) \frac{\int_{-\infty}^{+\infty} T(E)M(E)[(E-E_F)/k_B T] \left(-\frac{\partial f_0}{\partial E}\right) dE}{\int_{-\infty}^{+\infty} T(E)M(E) \left(-\frac{\partial f_0}{\partial E}\right) dE} \dots\dots\dots (1.5)$$

where, k_B is the Boltzmann constant, E is the energy at which the current flow and E_F is the Fermi energy of the material [29]. The equations (1.1) and (1.5) clearly explore that enhancement of power factor of a thermoelectric material can be achieved by creating a best band structure from an optimized tradeoff between electrical conductivity and Seebeck coefficient. This is the basic strategy for the enhancement of power factor of thermoelectric materials.

In addition to the optimization of carrier concentration, advanced techniques such as intrinsic point defects, band convergence, resonant energy levels and nanostructuring can also be employed to improve the thermoelectric conversion capability of various compounds according to their crystallographic and electronic structures. These techniques are mainly based on the engineering of distortions of the electronic density of states (DOS) near the Fermi energy. The larger DOS and the stronger its dependence on energy, the higher Seebeck coefficient will be for a given carrier concentration. The application of each method has unique advantages on different scenarios. In conduction band convergence, the increase in conduction band valleys associated with the transport mechanism results in significant improvement of power factor. This is an easy way to decouple the interdependence of Seebeck coefficient and electrical resistivity. In resonant energy levels, the enhancement of Seebeck coefficient is supplemented by two ways. Both the triggered peak in the DOS and selective scattering of charge carriers by resonant levels influence the power factor. The particle size in nanoregimes can also influence the DOS by quantum confinement effect. The success of these approaches lie in the realization of the experimental condition which is required to distort and increase DOS near the Fermi level of the prepared materials. Hence, optimization of experimental parameters for the material preparation is important when adopting these techniques [31].

1.4 Thermoelectric materials

The development of a high efficient thermoelectric system requires the energy conversion materials with high capability for converting heat into electricity. A good thermoelectric material must possess high power factor along with low thermal conductivity. In mid 1990s, Glen A Slack introduced ‘Phonon Glass Electron Crystal’ (PGEC) concept for ideal thermoelectric materials. The materials which conduct electrons like crystals and restrict phonon like glass concurrently can efficiently perform as a thermoelectric converter. The materials with $ZT > 1$ are considered as thermoelectric materials. The materials having $ZT \geq 2$ are normally considered for commercial thermoelectric materials. However, the materials showing moderate conversion capability can also be utilized if it is earth abundant and thermally stable [32]. The state of the art thermoelectric materials are shown in fig. 1.6.

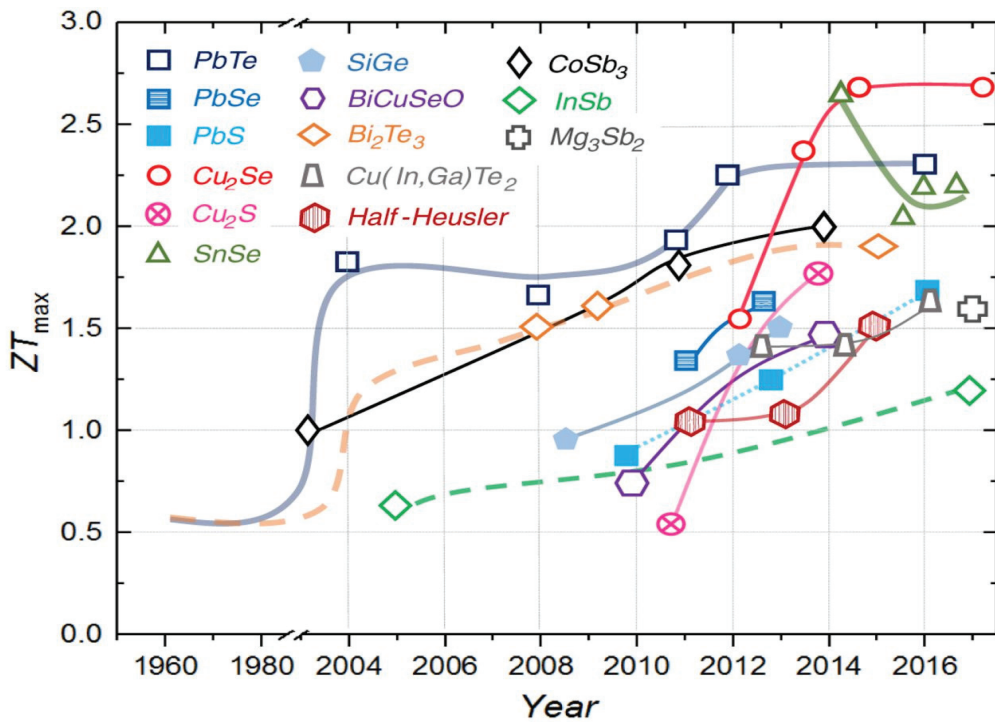


FIGURE 1.6. The figure of merit of the state of the art thermoelectric materials

The thermoelectric materials have different values of ZT in different temperature ranges which limit their application with specific temperature ranges. The alloys of Bi_2Te_3 , $PbTe$ and $SiGe$ are utilized as the conversion materials for low, medium and high temperature applications respectively. Thermoelectric materials are categorized as tellurides, silicides, oxides, chalcogenides, clathrates, skutterudites,

half-Heusler compounds and Zintl phase materials [33]. Bismuth telluride is a tetradymite structure with space group $R\bar{3}m$. The lattice is stacked in a repeated sequence of Te-Bi-Te-Bi-Te and the second Te atom has different bonding characteristics from the other two Te atoms. The strong ionic and covalent bonds between Te and Bi layers in a same unit and the weak Van der Waals force between two adjacent layers on the boundaries of each unit form cleavages in planes of Bi_2Te_3 perpendicular to c-axis. These structure properties make the material superior in thermoelectric conversion materials. Lead telluride based alloys are the member of lead chalcogenide family. The cubic NaCl structure consisting of two interpenetrating face centred cubic lattices is very accommodating and can be alloyed with many other compounds of compatible crystal structure and thus result in lower lattice thermal conductivity. This compound can be prepared by a variety of synthesis techniques and hence the alloying and various morphological forms are possible to enhance the thermoelectric properties. In recent years, thallium doped lead telluride achieved excellent progress in thermoelectric efficiency on the basis of electron resonant states and band convergence. The alloying of silicon with germanium considerably brought down the lattice thermal conductivity of its elemental species and the cubic structure offers potential electronic transport properties. This promises good thermoelectric figure of merit to silicon-germanium alloys [31].

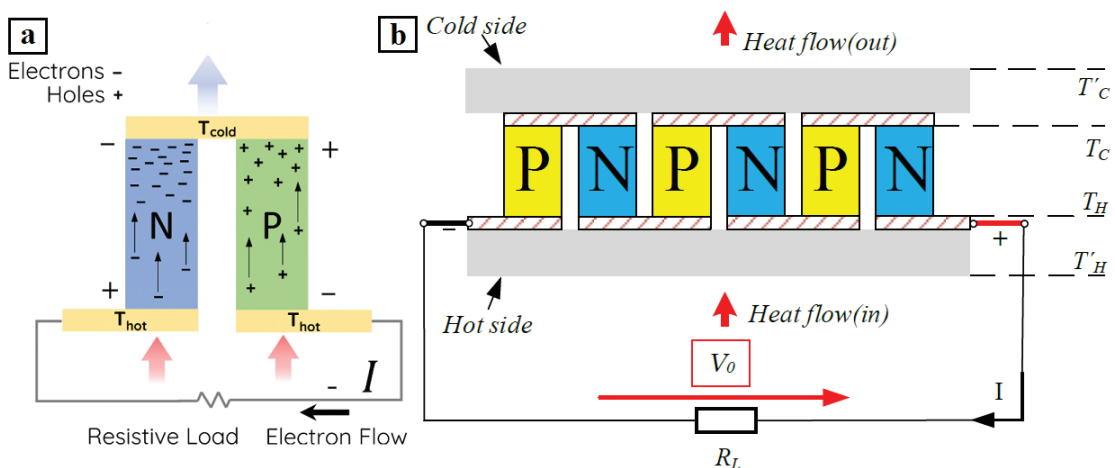
Skutterudites and clathrates belong to the group of caged compound thermoelectric materials. The phonon-glass electron-crystal concept of thermoelectric material works best in these compounds when the structural voids filled with guest atoms. The optimization of the framework structure by carefully choosing the filler species favours reduced lattice thermal conductivity without affecting the existing good electronic transport properties. The skutterudites have a general chemical formula MX_3 ($M=Co, Rh$ or Ir and $X=P, As$ or Sb). The single and multi filling of $CoSb_3$ -based skutterudites shows exceptionally high figure of merit. Clathrates are composed of tetrahedrally coordinated Al, Si, Ga, Ge, Sn, etc., atoms with polyhedral cages of different size. Here also, the filler atoms are considered as rattlers that efficiently scatter lattice phonons resulting in a low lattice thermal conductivity. Single and poly crystalline $Ba_8Ga_{16}Ge_{30}$ are the best clathrates compounds for thermoelectric energy conversion. Half-Heusler alloys crystallise in the $MgAgAs$ -type structure with the space group $F\bar{4}3m$, where X, Y and Z atoms occupy interpenetrating

face-centred cubic sublattices. The structural features promise the reduction of lattice thermal conductivity of half-Heuslers without deteriorating the existing electronic transport properties. The most studied families of half-Heusler alloys for the thermoelectric applications are $MNiSn$ and $MCoSb$ ($M=Ti, Zr$ or Hf) based alloys. As thermoelectric material, one of the Zintl phase, $Yb_{14}MnSb_{11}$ has received wide attention due to its unique low temperature electronic properties. This compound is isostructural to $Ca_{14}AlSb_{11}$ and crystallizes in the space group of $I4_1/a$. It displays low thermal conductivity due to large complex unit cells and high atomic mass. The AM_2Sb_2 Zintl phase ($A=Ca, Sr, Ba, Yb$ or Eu and $M=An, Mn$ or Cd) also has potential thermoelectric properties due to its intrinsic features such as small bandgap, large DOS at the Fermi level and covalently bonded and sandwiched type crystal structure [33].

This thesis deals with the enhancement of thermoelectric properties of nitride and oxide thin films for device applications. The work focuses on the earth abundant and nontoxic compounds having the capability to be transformed as efficient n- and p-type thermoelectric materials by advanced techniques like band convergence, resonant levels, point defects and nanostructuring. Hence tin nitride (Sn_3N_4) and zinc tin nitride ($ZnSnN_2$) and chromium nitride (CrN) and nickel oxide (NiO) were chosen for the investigation of n- and p-type materials respectively on the basis of the keen analysis of the crystallographic and electronic band structures and basic physical properties.

1.5 Thermoelectric devices

A thermoelectric generator is a solid state device that converts heat into electricity by Seebeck effect. It has the advantages of no moving parts, long lifetime



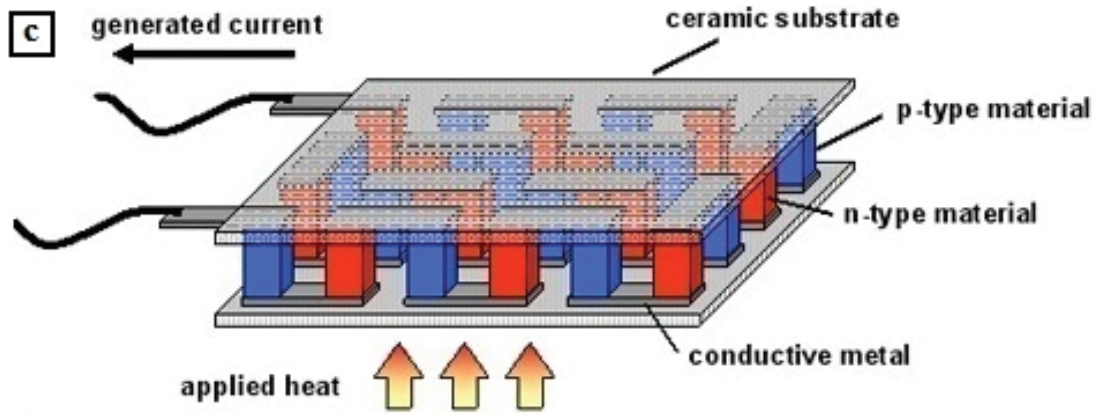


FIGURE 1.7. The Seebeck effect for power generation in (a) a thermoelectric couple (b) serially connected thermoelectric couples and (c) a thermoelectric module

and environmental friendly [34]. The thermoelectric generator is constructed by alternatively attaching n-type and p-type semiconductor materials that are electrically connected in series and thermally in parallel as shown in fig. 1.7.

Several parameters have been introduced to evaluate the performance of a thermoelectric generator. In general, efficiency is defined as

$$\eta = \frac{\text{Net power output}}{\text{Net power input}} = \frac{\text{Output power of the TEG}}{\text{Heat energy absorbed at the hot junction}} \dots\dots (1.6)$$

The maximum output power of TEG composed of thermoelectric materials is

$$P_{max} = \left(\frac{T_h - T_c}{T_h} \right) Q \frac{\sqrt{Z\bar{T} + 1} - 1}{\sqrt{Z\bar{T} + 1} + \frac{T_c}{T_h}} \dots\dots\dots (1.7)$$

where, Q is the rate of heat transfer through the generator, T_h and T_c are the temperature at the hot and cold junctions respectively and \bar{T} is the average temperature of both n- and p-type legs between T_h and T_c [35]. The equations (1.7) and (1.8) describe the importance of thermoelectric parameters of individual leg material on the power conversion capability of a TEG. Hence, the selection of p-type and n-type material is very important for a TEG.

The thermoelectric performance of a material can be assessed by considering various quality parameters. These parameters are the combinations of different microscopic properties of the material. The most important parameter is the figure of

merit, ZT which is already discussed with reference to Seebeck coefficient and electrical conductivity. Another parameter which is commonly used to evaluate the materials is thermoelectric quality factor, B . This can be described as,

$$B \propto \frac{\mu_c m^{*1.5} T^{2.5}}{\kappa_L} \dots\dots\dots (1.8)$$

where μ_c is the carrier mobility, m^* is the effective mass, κ_L is the lattice thermal conductivity [21]. It deals with the decoupling of electrical conductivity and Seebeck coefficient which are represented by mobility and effective mass respectively in the equation while minimizing the lattice thermal conductivity. The quality factor has great role in thermoelectric material processing during the optimization of electrical conductivity and Seebeck coefficient and the higher the B value, the higher the ZT value. The third material parameter is the thermoelectric compatibility factor, S^* .

$$S^* = \frac{\sqrt{ZT+1}-1}{S T} \dots\dots\dots (1.9)$$

where ZT is the figure of merit and S is the Seebeck coefficient [21]. This parameter helps to extract the maximum conversion capability of a material by optimizing geometrical shape and compositional variations of material legs of a thermoelectric device. Hence, it is a device design related parameter which has considerable role during the fabrication of TEGs. These three material quality parameters together greatly support the researchers to analyse whether a compound can be transformed as an efficient thermoelectric material and to correlate the material properties with device performance [36].

1.6 Motivation and objectives of the thesis

Transition to the green energy sources is the only solution to balance the challenges between development and environment. Thermoelectrics is an eco-friendly electrical power generation technique based on sustainable resources. But, the application of the technique is limited due to scarcity and toxicity of the efficient conversion materials and inefficiency of the environmentally benign materials. Hence,

continuing efforts to be given for the development of earth abundant and non-toxic materials with good thermoelectric conversion efficiency.

The primary objective of this research work is to prepare efficient thin films of earth abundant and nontoxic nitrides and oxides for thermoelectric device applications. The thin films of n- and p-type materials are prepared by reactive radio frequency magnetron sputtering. Initially, the compounds having the capability to be transformed as an efficient thermoelectric material are identified by the keen analysis of the crystallographic and electronic band structures and basic physical properties. The sputtering parameters for the specific properties of the thin films according to the requirements are optimized by various characterizations. The advanced techniques such as band convergence, resonant energy levels, nanostructuring, and intrinsic point defects are employed to improve the thermoelectric conversion capability of the thin films. To evaluate the performance in a device form, the prototype thermoelectric generators are fabricated by the investigated thin films as n- and p-type leg materials.

References

- [1] I.E.A., World energy outlook: Executive summary, International Energy Agency, Paris (2019). <https://www.iea.org/reports/world-energy-outlook-2019>.
- [2] I.E.A., Global energy review: The latest trends in energy and emissions, International Energy Agency, Paris (2019). <https://www.iea.org/reports/global-energy-review-2019>.
- [3] I.E.A., World energy balances: Overview, International Energy Agency, Paris (2019). <https://www.iea.org/reports/world-energy-balances-overview>.
- [4] I.E.A. Exploring clean energy pathways: The role of CO₂ storage, International Energy Agency, Paris (2019). <https://www.iea.org/reports/the-role-of-co2-storage>.
- [5] I.E.A., CO₂ emissions from fuel combustion: Overview, International Energy Agency, Paris (2019). <https://www.iea.org/reports/co2-emissions-from-fuel-combustion-overview>.
- [6] B. Zhengfu, I.I. Hilary, L.D. John, O. Frank, S. Sue, Min. Sci. Technol. 20 (2010) 215–223.
- [7] I.E.A., World energy outlook: Executive summary, International Energy Agency, Paris (2018). <https://www.iea.org/reports/world-energy-outlook-2018>.
- [8] I.E.A., Southeast Asia energy outlook: Special report, International Energy

- Agency, Paris (2017). <https://www.iea.org/reports/southeast-asia-energy-outlook-2017>.
- [9] R.G. Newell, D. Raimi, G. Aldana, Global energy outlook 2019 : The next generation of energy, Resources for the future, Washington (2019). <https://www.rff.org/publications/reports/global-energy-outlook-2019>.
- [10] I.E.A., Renewables information: Overview, International Energy Agency, Paris (2017). <https://www.iea.org/reports/renewables-information-overview>.
- [11] I.B.E.F., Renewable energy, India Brand Equity Foundation, New Delhi (2019). <https://www.ibef.org/download/Renewable-Energy-August-2019.pdf>.
- [12] M.A. Zoui, S. Bentouba, J.G. Stocholm, M. Bourouis, *Energies* 13 (2020) 3603.
- [13] M.A. Green, *Prog. Energy* 1 (2019) 013001.
- [14] C. Forman, I.K. Muritala, R. Pardemann, B. Meyer, *Renew. Sustain. Energy Rev.* 57 (2016) 1568–1579.
- [15] X. Zhang, L. Zhao, *J. Mater.* 1 (2015) 92–105.
- [16] L.E. Bell, *J. Elect. Mater.* 38 (2009) 1344–1349.
- [17] R.A. Kishore, S. Priya, *Materials* 11 (2018) 1433.
- [18] E. Velmre, *IEEE Xplore* (2010) 17–24.
- [19] K.R. Adhikari, *The Himalayan Physics* 6 (2017) 10–14.
- [20] L. Anatyckuk, *WIT transactions on state of the art in science and engineering.* 89 (2015) 337-362.
- [21] H.J. Goldsmid, *Introduction to thermoelectricity*, Springer, New York (2010).
- [22] D.M. Rowe, *CRC handbook of thermoelectrics*, CRC Press, New York (1995).
- [23] P. Douglas, *Thermoelectric energy harvesting, ICT-Energy-Concepts towards zero*, Intech, London (2014).
- [24] D.M. Rowe, *Thermoelectrics-Handbook-Macro to nano*, Taylor & Francis, New York (2006).
- [25] S. S. Li, *Semiconductor physical electronics*, Springer, Boston (1983).
- [26] J. Wei, H.J. Liu, L. Cheng, J. Zhang, J.H. Liang, P.H. Jiang, D.D. Fan, J. Shi, *AIP Adv.* 5 (2015) 107230.
- [27] G.D. Mahan, J.O. Sofo, *Proc. Natl. Acad. Sci.* 93 (1996) 7436–7439.
- [28] S. Datta, *Electronic transport in mesoscopic systems*, Cambridge University Press, U.K. (1995).
- [29] C. Jeong, R. Kim, M. Luisier, S. Datta, M. Lundstrom, *J. Appl. Phys.* 107 (2010) 023707.
- [30] R. Kim, S. Datta, M.S. Lundstrom, *J. Appl. Phys.* 105 (2009) 034506.
- [31] J. He, T.M. Tritt, *Science* 357 (2017) 1369.
- [32] T.M. Tritt, *Encyclopedia of materials: Science and technology*, Elsevier, Netherlands (2002).

- [33] I. Petsagkourakis, K. Tybrandt, X. Crispin, I. Ohkubo, N. Satoh, T. Mori, *Sci. Technol. Adv. Mater.* 19 (2018) 836-862.
- [34] Y. Du, J. Xu, B. Paul, P. Eklund, *Appl. Mater. Today* 12 (2018) 366–388.
- [35] X.F. Zheng, C.X. Liu, Y.Y. Yan, Q. Wang, *Renew. Sustain. Energy Rev.* 32 (2014) 486–503.
- [36] R. He, G. Schierning, K. Nielsch, *Adv. Mater. Technol.* 3 (2018) 1700256.

* * * * *

THIN FILM DEPOSITION AND CHARACTERIZATION TECHNIQUES

Contents

-
- 2.1 Introduction
 - 2.2 Sputtering
 - 2.3 X-ray diffraction
 - 2.4 Atomic force microscopy
 - 2.5 Hall measurement
 - 2.5 UV-Vis spectroscopy
 - 2.6 Thermoelectric measurement
 - 2.7 Thermoelectric generator characteristics
-

This chapter deals with the various aspects of reactive radio frequency magnetron sputtering which is the deposition technique used to fabricate the thin films in this study. The characterization techniques which are employed to analyze the various parameters of the prepared thin films are also discussed.

2.1 Introduction

A film is normally a layer of material while thin film represents a layer of material having thickness less than 1 μm . The interesting factor of thin films is the very small thickness ranges from few nano meters to micro meters and the atoms at the surface are not surrounded on all sides by similar atoms as are interior atoms. Its thickness is only a few atomic layers hence considered as ‘all surface’ structure and having very large surface to volume ratio. This makes the materials exceptional and it exhibits drastically different surface features and physical properties from their bulk counterparts. The thickness depended physical properties and low requirement of materials for device fabrication make thin films technology important in micro and nano electromechanical systems, optical and optoelectronic devices. The properties of the thin films are greatly influenced by the surface and microstructural features which are developed during its growth [1]. Hence, the detailed understanding of the deposition technique used for the fabrication as well as the working principle of various characterization techniques is important for this research work.

2.2 Fabrication of thin films

2.2.1 The thin film deposition techniques

The understanding of nucleation and growth kinetics at the atomic scale is a fundamental aspect in the thin film studies. It determines the crystallographic features and microstructural evolution and hence the physical properties of thin films. Most of the properties of thin films depends on and can be modified by the deposition process and not all processes produce with the same properties. Hence the technique and the primary parameters which are used to deposit the films have significant importance in this study. There are many deposition techniques which are utilized according to nature of the material and the requirement of the devices. Basically, the deposition methods are classified as physical and chemical processes. The physical processes are further classified as evaporation and sputtering and chemical processes as gas phase and liquid phase chemical methods [1]. The detailed classification is given below as chart in fig. 2.1. In our study, the nitride and oxide thin films are deposited by reactive radio frequency (RF) magnetron sputtering. Hence, the various aspects of sputtering deposition technique are to be discussed in detail.

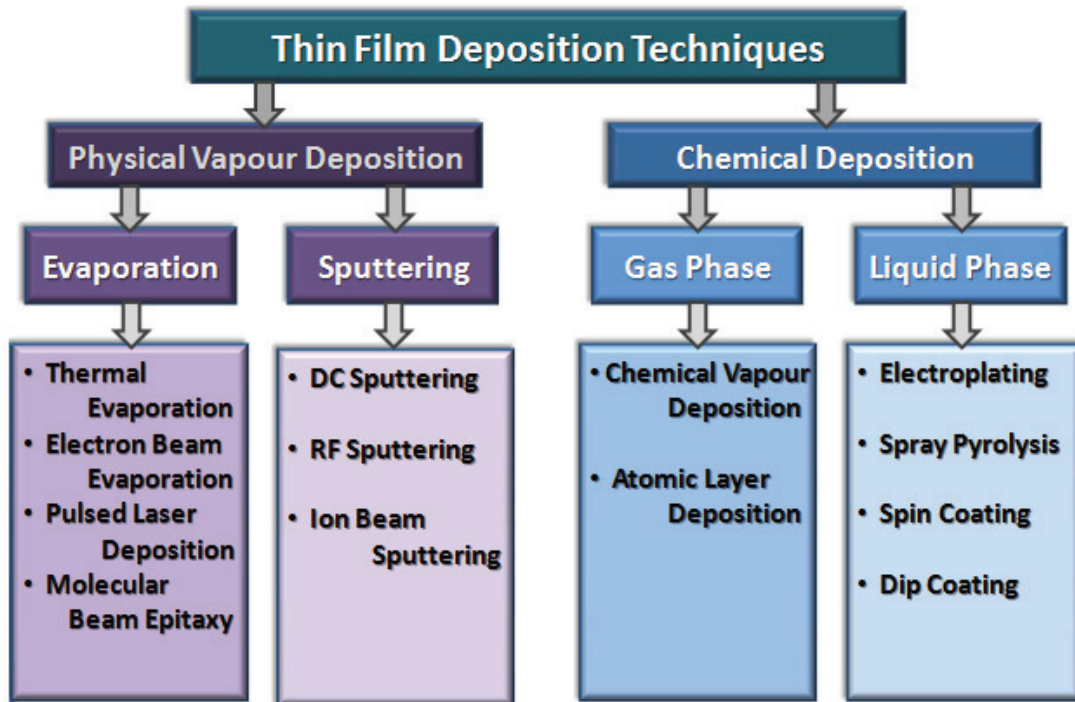


FIGURE 2.1. Classification of thin film deposition techniques

2.2.2 Sputtering

Sputtering is a physical vapour deposition process in which the material particles are ejected from the target surface due to the bombardment of energetic particles and depositing it on a substrate under high vacuum environment. Sputtering was first reported in the literature in 1852 by W.R. Grove [2]. The description of his observations during an investigation of the electrical conductivity of gases by direct current glow discharges led to the development of an extremely versatile technique for thin film deposition. He importantly noted the formation of metallic deposits on the inner wall of a glass discharge tube which was utilized for the investigation. Sputtering is presently being used in many industrial purposes especially in semiconductor device technology. Apart from the various types thin film depositions, sputtering is greatly utilized for etching patterns and surface etching for cleaning and chemical analysis. Sputtering has many advantages over the other deposition techniques; the important one is the possibility to deposit wide range of materials like metals, insulators, alloys and composites even the melting point is very high. The thin films deposited by sputtering usually have a stoichiometry close to that of a target material and shows good adhesion, step coverage and uniformity. Thin films having

uniform thickness over large substrates can be deposited using large area targets. The control over various sputtering parameters allows fabricating versatile thin films showing excellent properties like preferred orientation, amorphous to crystalline transformation and point defect formation. In addition to these advantages, the basic features can be upgraded by using RF power supply, magnets and reactive gases. The disadvantages of the sputtering process are the complexity to reproduce the thin films unless extreme care to be given for the collective optimization of many sputtering parameters and hard to produce high quality thick coatings due to porosity, pin holes, gas incorporation into films and high internal stress [3].

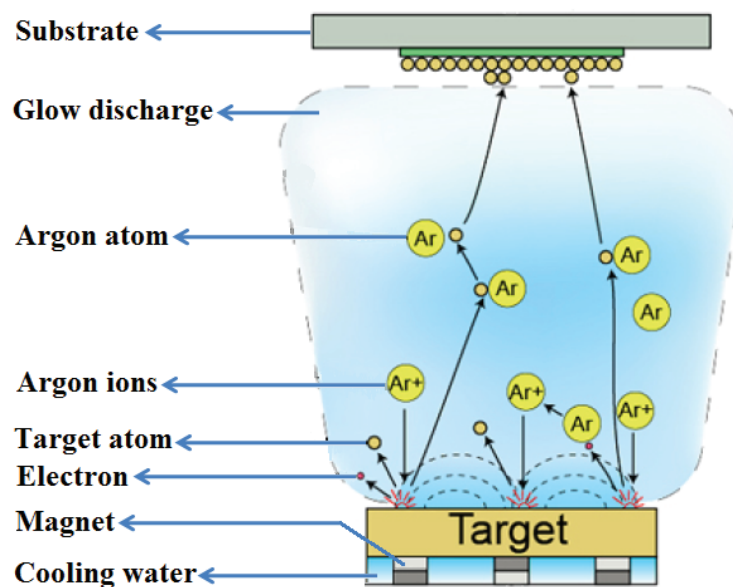


FIGURE 2.2. Basic sputtering processes

In sputtering process, target is the source of the material desired to be deposited and substrate is a substantial base to support the thin film, both are enclosed in a vacuum chamber which was pumped down to a prescribed process pressure. Then electrically neutral gas typically argon atoms are purged in to the vacuum chamber and a voltage is applied between the target and the substrate so that the target acts as cathode and substrate as anode. The stray electrons near the cathode are accelerated towards the anode and collide with neutral gas atoms converting it to a positively charged ion. It is a cascading process in which a new electron is generated in each collision and ionizes the other atoms until the gas breaks down. This process creates plasma or glow discharge and positively charged gas ions are attracted towards the cathode target at very high speed. The bombardment of sputtering gas transfers

momentum and ejects target atoms from the surface. These particles are condensed as thin film onto the surface of the substrate [4]. The basic sputtering processes are schematically represented in fig. 2.2.

2.2.2.1 Reactive radio frequency magnetron sputtering

The sputtering can be performed by different modes and depending on the source used for powering the system, it can be classified as direct current (DC) and RF sputtering. DC sputtering is generally utilized for depositing conductive materials. In case of insulating targets, the dc electrical discharge would result in the charging up of the target and will adversely affect the deposition process. Therefore radio frequency power supply of 13 MHz is used for energizing the system. RF excitation reverses the surface polarity of the target continuously and neutralizes the accumulated charges. Hence RF sputtering can be utilized for depositing conducting, insulating and semiconducting materials. Another technique incorporates into the sputtering system is the confinement of electrons in the vicinity of the target by the assembly of magnets beneath the target. The presence of magnetic field improves the number of collisions between electrons and neutral sputter gas atoms around the target. This helps to perform efficient sputtering in a lower pressure and high quality films can be produced at increased deposition rate. Since the plasma is confined around the target, probability of impingement of the gas ions on the surface of the target increases and hence improves the sputtering yield. Also, it reduces the damage on the surface of the thin film caused by the stray electrons and gas ions and minimizes the impurities due to gas incorporation. Sometimes, compound thin films can be deposited in reactive manner by sputtering elemental or alloy targets in reactive gases. A reactive gas such as oxygen or nitrogen is added to the sputter gas or used as both sputtering and reactive gas so that oxide or nitride thin films can be deposited. It allows the control of multiple parameters simultaneously and hence exceptional results can be expected. During reactive sputtering chemical reactions occur both at the target as well as at the substrate. The amount of reactive gas incorporated in sputter deposited films mainly depends on partial pressure of reactive gas, sputtering rate as well as other sputtering parameters. Hence, thin films of binary and multinary compounds of nitrides, oxides and sulfides with desired properties can be easily fabricated by reactive sputtering [3].

2.2.2.2 Growth kinetics of thin films

The growth of thin film usually proceeds through nucleation and growth stages. The adatoms reach on the surface is either met another adatom to form a stable nucleus is known as nucleation or attached with an existing island is known as growth. The growth process involves the arrival of single adatom, migration, nucleation, collision and combination, island formation, coalescence and film formation [5]. The competition between nucleation and growth is determined by the adatom diffusion coefficient. The adatoms with large diffusion coefficient always find an existing island to attach and grow as a part of entropy minimization. It reduces the possibility of the adatom to attach with another one and prevents nucleation results in lower island density. Considering the thermodynamics of initial stages of growth, the competition between surface energy of substrate ($\gamma_{\text{substrate}}$), surface energy of film (γ_{film}) and interface energy between substrate and film ($\gamma_{\text{interface}}$) determines the growth process [6]. Based on the difference in growth advancement, three types of growth modes are defined as follows [7].

(i) Frank-van der Merwe mode: This mode of thin film growth contains layer by layer growth originates due to $(\gamma_{\text{substrate}}) \geq (\gamma_{\text{film}}) + (\gamma_{\text{interface}})$. The atoms are more strongly bound to the substrate than to each other and the first adsorbed atoms form a complete monolayer on the surface of the substrate. The growing layer of the film reduces the surface energy results in complete wetting of the surface and supplements the smooth layer by layer growth as shown in fig. 2.3.

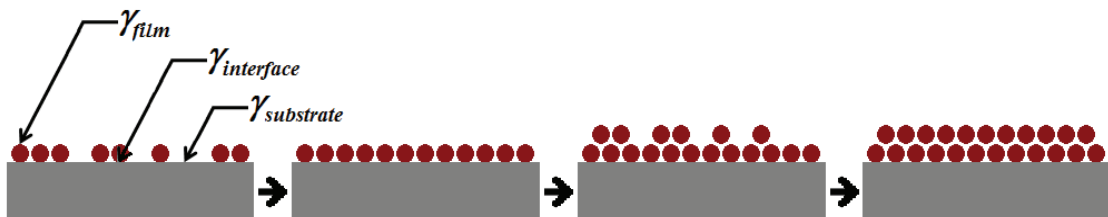


FIGURE 2.3. The layer by layer growth under Frank-van der Merwe mode

(ii) Volmer-Weber mode: In this mode, island type of crystallite growth is developed during the deposition of thin films. The atoms of the deposit are more strongly bound to each other than to the substrate due to $(\gamma_{\text{substrate}}) < (\gamma_{\text{film}}) + (\gamma_{\text{interface}})$. It balls up the

adsorbed atoms on the substrate surface in order to minimize the interface with the substrate. The surface diffusion of adatoms is slow, hence small clusters are nucleated directly on the surface of the substrate and then grow into the islands of adsorbed atoms as shown in fig. 2.4. The films in this mode usually exhibit uneven growth on the surfaces.

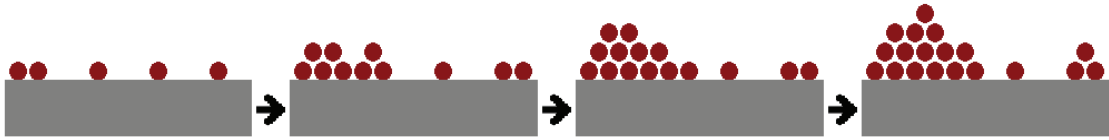


FIGURE 2.4. The island growth under Volmer-Weber mode

(iii) Stranski-Krastanov mode: This is a combined mode of layer by layer followed by island type growth of crystallites. After forming a few monolayers, islands are formed on the top of these layers. The initial layer is strained due to the mismatch between substrate and growing layer and after few layers the strain is relaxed results in island growth of crystallites as shown in fig. 2.5. Here, initially, $(\gamma_{\text{substrate}}) \geq (\gamma_{\text{film}}) + (\gamma_{\text{interface}})$ and then changes into $(\gamma_{\text{substrate}}) < (\gamma_{\text{film}}) + (\gamma_{\text{interface}})$.

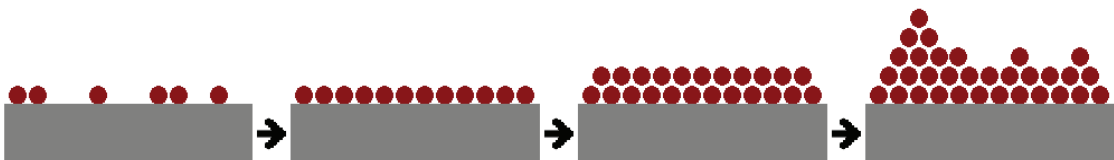


FIGURE 2.5. The layer by layer followed island growth under Stransky-Krastanov mode

These growth formalisms are originated as a consequence of the free energy minimization of the thin film system by maximizing the area of lowest energy surfaces while minimizing the interface energy. The thermodynamical consideration for this process is originated from the sputtering parameters during deposition. Since the microstructural evolution of sputtered thin films during growth is highly depended on the mode of crystallite growth, optimization of sputtering parameters is very important to achieve thin films having desired properties for each specific investigation.

2.2.2.3 Optimization of sputtering parameters

The major parameters that can be controlled in reactive RF magnetron sputtering process are working pressure, partial pressure of reactive gas, substrate temperature, power of RF bias and target-substrate distance. These parameters can markedly influence the energy of adsorbed atoms, deposition rate and chemical reaction and hence controls crystallographic structure, microstructure, phase, stoichiometry and defects of the thin films. The key factor behind the optimization of sputtering parameters is the knowledge about its correlation with growth kinetics of thin films. The energy required for the growth is provided by various sources such as substrate temperature, ionic bombarding and chemical reactions and it is available in the form of mobility of the adatoms. The adatoms experience a potential energy landscape formed by the structure and chemistry of the surface of the substrate. The presence of adsorption sites of different depth or stability determines the surface potential and act as barrier for adatom diffusion [7,8].

Assuming the diffusion barrier is same in all directions and the distance between the adsorption sites is separated by a distance, a , then surface diffusion coefficient or diffusivity can be described by the adatom jump rate, Γ as:

$$D = \frac{1}{4} a^2 \Gamma \dots\dots\dots (2.1)$$

where $\Gamma = \nu e^{-\frac{E_d}{k_B T}} \dots\dots\dots (2.2)$

where ν is the frequency of attempt of adatoms to overcome the diffusion barrier E_d as thermal jitters, T is the substrate temperature and k_B is the Boltzmann constant. The nature of the diffusion barrier is fixed by atomic structure of the surface and varies with each material and crystallite orientations in the same material. The diffusion barrier is also changed by the influence of other adatoms, nuclei, impurities and defects on the surface. The diffusion in larger scale can be defined in terms of chemical potential of adatoms. The diffusion is the process of the attempt of adatoms to occupy in a lowest energy position in the surface in order to reduce its chemical potential. The chemical potential is determined by the adatom density, the strain state

of the surface, the curvature of the surface and the presence of surface defects and can be expressed as:

$$\mu = (W - GK)\Omega \dots\dots\dots (2.3)$$

where W is the surface strain energy density, G is the surface energy density, K is the surface curvature and Ω is the atomic volume [1,9].

The evolution of microstructure of thin film has high influence on adatom mobility. The substrate temperature and the energy of adsorbed atoms are the parameters which determine the adatom mobility. The energy of adsorbed atoms depends on many sputtering parameters like sputtering pressure, RF power and gas composition. The variation in adatom mobility results in growth of crystallites with different density, morphology and surface profile and greatly affects the optical and electrical properties of the thin film. The growth formalism of crystallites with normalized substrate temperature is well defined by the structure zone model of Movchan and Demchisshim in 1969. In 1974, Thorton elaborated the zone classification by considering the sputtering pressure with substrate temperature. Thereafter many zone classification studies were reported for various types of materials based on these two models. Hence, optimization of sputtering parameters in accordance with microstructural evolution is necessary for any thin film investigations. There is a range of limit to tune some sputtering parameters for the requirement of the specific properties. The optimization of the parameters cannot exceed the basic requirements of the instrument to perform an efficient sputtering. Consider the sputtering pressure, at too low pressure, the collisions between atoms and electrons to sustain plasma are not enough and at too high pressure, there are so many collisions that electrons do not have enough time to acquire energy between collisions to be able to ionize the atoms. Hence, the optimized sputtering pressure for the specific properties of the thin film should have the strength to sustain plasma as well as generate high energy electrons [7,10].

The deposition rate of target atoms on the substrate surface is another parameter which influences the properties of the growing thin film. It can influence

microstructural features as well as the stoichiometry of thin film in a reactive sputtering. It is directly related with the yield of the sputtering process, Y , which is defined as the ratio of the number of target atoms ejected to the number of incident ions. The factors which determine the sputtering yield or it can be estimated as:

$$Y = \frac{3\alpha}{4\pi^2} \frac{4m_i m_t}{(m_i + m_t)^2} \frac{E}{U} \dots\dots\dots (2.4)$$

where m_i is the atomic mass of the bombarding incident ion, m_t is the atomic mass of the target, E is the energy of the incident ion, U is the binding energy of the surface atoms of the target and α is a constant depends on the ratio of m_i to m_t . Hence the sputtering parameters to be optimized to tune the deposition rate are the sputtering power, working pressure and partial pressure of reactive gas [11].

The growth of preferentially oriented crystallites is usually seen in sputtered thin films especially in nitrides. The orientation of crystallites have great role in the physical properties of the thin films. The origin of preferred orientation lies in the competition between surface energy and strain energy during the growth. The surface and strain energies developed are proportional to the substrate temperature and energy of the bombarding particles respectively. The variation in strain energy is developed from the difference in the increasing rate of strain energy of crystallographic planes due to the anisotropy of elastic moduli. Hence preferred orientation can be tuned by controlling the substrate temperature and the sputtering parameters which determine the energy of the bombarding ions [7,12]. Defects are another major factor which influences the various properties of deposited thin films. In reactive sputtering, intrinsic point defects can be tuned very precisely by controlling the target stoichiometry and partial pressure of reactive gas. The knowledge about the formation energy of defects and the correlation between the chemical potential of constituent elements of the thin film compound and sputtering parameters will bring exciting improvements in the physical properties. In addition to the optimization of individual parameters, the simultaneous control over multiple sputtering parameters offers more significant improvement in various functionalities of the thin films [13].

2.2.3 Factors considered to select the deposition technique

The discussions regarding fabrication, growth and deposition parameters of thin films has explored that the deposition technique has great importance to fulfil the objectives of a study regarding thin films and devices. Many deposition techniques are available for the fabrication of thin films as discussed earlier and each one has its own advantages and limitations. However, stability, quality and repeatability of the prepared thin films, ease of operation and availability of the equipment and nature of the study are the primary factors which have to be considered for the selection of fabrication technique [1,3].

This study mainly focuses on the nitride and oxide thin films of n- and p-type thermoelectric materials for device applications. The strategies adopted in the work like convergence of conduction band, formation of resonant levels and transformation of type of conductivity are stemmed from the formation of point defects. These are aroused as a consequence of the precise tuning of partial pressure of reactive gas and stoichiometry of target compound. Another strategy, nanostructuring is adopted by varying the substrate temperature during the deposition of thin films. Moreover, the deposition parameters are to be optimized before each investigation according to the specific requirements. Hence this study requires the deposition of compound thin films in a reactive manner and the precise tuning of individual and multiple deposition parameters simultaneously during the fabrication. Taking in to account all these factors, there was considerable motivation for us to choose reactive radio frequency magnetron sputtering for our study.

The RF magnetron sputtering allows the reactive deposition of compound thin film and offers excellent repeatability especially in presence of stoichiometric variations of reactive depositions. Since it fabricates high quality dense thin films having smooth surfaces on a large area, the deposited thin films can be considered as ideal samples for the analysis of optical and electrical properties. Moreover, the sputtering system allows more ease and manual control over various instrumental parameters, hence the deposition conditions can be precisely tuned for specific investigations. Also, the masking of substrates and deposited films are required during the fabrication of n- and p-type legs of thermoelectric generators and this can be easily done with the sputtering chamber [14].

In this study, the deposition of oxide and nitride thin films for various investigations and the fabrication of thin film thermoelectric generators were carried out by Hind Hivac 12 MSPT sputtering system. It comprises a diffusion pump backed by a rotary pump to evacuate the chamber up to 6×10^{-6} mbar. The RF power supply, R301 and the automatic matching network controller, MC2 made by SERENE are equipped to optimize the power transfer from RF source to the plasma. The high quality argon, nitrogen and oxygen in pure and mixture forms are used to generate plasma for reactive sputtering according to the requirement of the investigations. A two inch diameter target holder and twelve inch diameter planar magnetron and a substrate holder are mounted in the chamber with sputter up configuration. The thickness of the thin film is monitored in situ using a quartz crystal monitor. The maximum sputtering power that can be delivered by the supply is 400 W. The resistive heater provides a maximum temperature of 500°C to substrate. The RF magnetron sputtering used for the study is shown in fig. 2.6.



FIGURE 2.6. The RF magnetron sputtering system

2.3 Characterization techniques

2.3.1 X-ray diffraction

X-ray diffraction is an experimental technique primarily used to explore the crystallographic features of materials. It employs the diffraction of X-rays by the atomic arrangement in the crystalline materials. The maximum information can most readily be obtained by using the electromagnetic radiation whose wave lengths are of the order of the interatomic spacing in crystals. Since the typical interatomic spacing is about 2-3 Å, X-rays are used for the study of crystal structures. In case of some specific analysis, neutrons and electrons are also used for diffraction studies. When an atom is exposed to X-rays, the atomic electrons are accelerated and they radiate at the frequency of the incident radiation. Under certain conditions the superposition of these waves results in diffraction pattern which contains the informations about the atomic arrangement within the crystal. When the atoms are arranged differently, a different diffraction pattern is produced. The diffraction pattern for every phase is unique and considered as the fingerprint of a material. Thus it is ideally suited for characterization and identification of polycrystalline phases and crystal structure. It can also provide the information to determine crystallinity, lattice parameter, crystallite size, preferred orientation and microstrain [15].

In 1912, W. L. Bragg presented a simple explanation for the diffracted beams from a crystal. The diffracted beams are found when the reflections from parallel planes of atoms interfere constructively. Constructive interference of the radiation from successive planes occurs when the path difference is an integral number, n of wavelengths λ , so that:

$$2d \sin \theta = n\lambda \quad \dots\dots\dots (2.5)$$

where $2d \sin \theta$ is the path difference of the rays reflected from adjacent planes having interplanar spacing, d . This is Bragg's law, which can be satisfied only for wavelength $\lambda \leq 2d$. The schematic interpretation of Bragg reflection is shown in fig. 2.7 [16]. Since the X-ray wavelength is normally fixed in diffractometers, the Bragg's law relates the diffraction angle to interplanar spacing, consequently a family of planes produces a diffraction peak only at a specific angle 2θ .

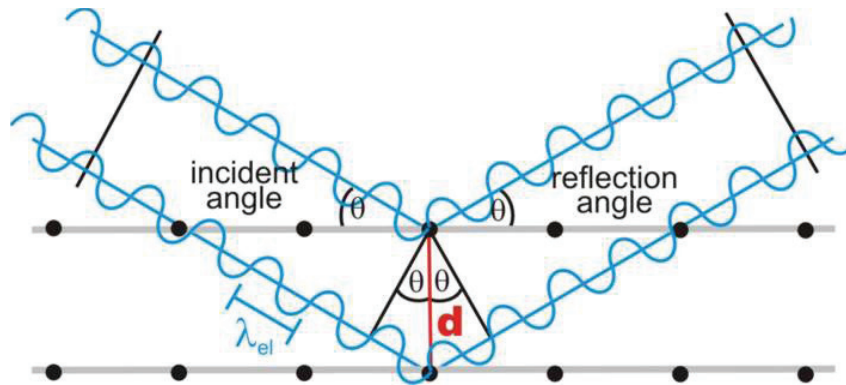


FIGURE 2.7. The schematic interpretation of Bragg reflection

Bragg’s law considers certain ideal conditions such that a perfect crystal and an incident beam composed of perfectly parallel and strictly monochromatic radiation. Any deviation from these conditions results in the variation of diffraction pattern. The broadening effect on the diffraction pattern due to the size of crystallites smaller than ~ 100 nm leads to the formulation of Scherrer equation:

$$t = K\lambda/\beta\cos \theta \quad \dots\dots\dots (2.6)$$

where t is the particle size, λ is the wavelength of the X-ray used, θ is the Bragg angle, β is the full width at half maximum of peak in radian located at any 2θ in the pattern and K is Scherrer constant varies from 0.62 to 2.08 according to the shape of the crystal and geometry of the unit cell [15].

2.3.1.1 Instrumentation

The X-ray diffractometer consists of three basic elements an X-ray tube, a sample holder and an X-ray detector. The electrons generated from a heating filament are used to generate X-rays. The electrons are accelerated towards a target material by applying a voltage and produces X-ray spectra. Copper is the most common target material having a wavelength of radiation $\text{CuK}_\alpha = 1.5418 \text{ \AA}$. These radiations are collimated and directed onto the sample. The intensity of the reflected X-rays are recorded when the sample and detector are rotated. The instrumentation of an X-ray diffractometer is such that the sample rotates in the path of X-ray beam at an angle

θ while the goniometer rotates an angle of 2θ . When the incident X-rays falls on the sample satisfies the Bragg reflection condition, constructive interference occurs and observes an intense peak. The fig. 2.8 schematically illustrates the powder X-ray diffraction instrumentation by Bragg-Brentano geometry [17].

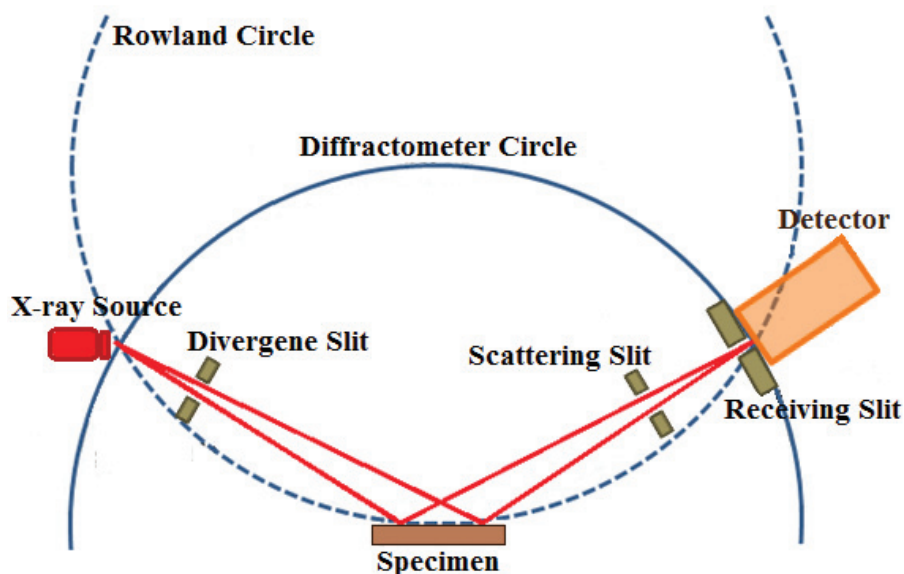


FIGURE 2.8. Bragg-Brentano geometry of XRD instrumentation

In this study, we have made use of Rigaku-MiniFlex 600 X-ray diffractometer for the analysis of phase, crystallinity and preferred orientation of the sputtered polycrystalline thin films. The internal view of the instrument is shown in fig. 2.9. The



FIGURE 2.9. Rigaku-MiniFlex 600 X-ray diffractometer

maximum power that can be delivered to the X-ray tube is 600 W (40 kV and 15 mA) for the generation of X-rays. It uses nickel filter, silicon strip detector and graphite monochromator. It usually performs analysis at room temperature using θ - 2θ method in continuous mode. It can record the diffractogram in a scanning range of -3 to 145° with scanning speed of 0.01 to $100^\circ/\text{minute}$ and minimum step size of 0.005° . The analysis of the X-ray diffractogram and its comparison with standard diffraction data, International Centre for Diffraction Data (ICDD) was done using integrated X-ray powder diffraction software, PDXL2 [18].

2.3.2 Atomic force microscopy

Microscopy is the characterization of objects using microscopes to view objects and areas of objects that cannot be seen with the naked human eye. Atomic Force Microscopy (AFM), also known as Scanning Force Microscopy (SFM), is an imaging technique that allows the mapping of surface topography and material properties with nanometer resolutions. The principle of operation is based on a cantilever probe with sharp tip that scans over a few angstrom distance above the surface of solid specimen. The interatomic force between the atoms on the surface and on the tip causes the deflection of the micro-fabricated cantilever. Since the deflection of the cantilever depends strongly upon the separation between the surface and tip atoms, they can be used to map out the surface topography with atomic resolution in all three dimensions [19].

Atomic force microscopy offers a multitude of different measurement modes that enable to characterize different properties of various types of samples. The basic and simplest mode of operation is contact mode. In this mode, the probe is in continuous contact with the surface while the probe raster scans the surface. Hence, the close range repulsive deflections are used to trace the surface features. In non-contact mode, a vibrating cantilever hovers very close to the surface of the sample instead of contact with it. As the tip approaches a sample, the changes in the vibrations of cantilever due to the attractive force between the tip and sample can be correlated with the topographical features. Tapping mode is a combination of contact and non-contact mode and takes advantages of both. During the scan, the cantilever

intermittently touches the surface and due to the interaction between the tip and surface, the amplitude of vibrations changes. The analysis of the feedback control signals used to maintain a constant amplitude provides the information about the surface topography. AFM can estimate morphology, surface roughness, particle size and step height by analyzing the topographic images of the thin films. In addition to the topographic studies, AFM is widely used to collect data on various mechanical and electrical properties with nanoscale resolution. The Conductive Atomic Force Microscopy (CAFM) maps the local electrical properties of the sample simultaneously with the topography by monitoring the currents flowing at the tip-sample nanojunction [20].

2.3.2.1 Instrumentation

In AFM, the surface imaging is realized by monitoring the interactive force between tip and sample in different locations while the probe is rastering the sample surface with the help of a piezoelectric actuator. An electronic feedback loop is employed to keep the force between probe and sample constant during scanning. The deflection of cantilever with the surface variations is detected with the aid of a position sensitive photo detector (PSPD). These signals are given to the input of feedback system and the appropriate output control signals are generated. Hence amplification and processing of these error signals produce topographic images of the samples. The schematic representation of an atomic force microscopy is shown in fig. 2.10. In CAFM, a conductive probe, a voltage source to apply a potential difference between tip and sample holder and a preamplifier to convert the analogical current signal into digital voltages are employed to map the surface current distribution. During the scanning, the conductive tip is in contact with the sample and a bias voltage is applied between them and the current flow is sensed by linear amplifier. By maintaining a constant force between tip and sample, simultaneous topographic images can also be generated that enables the direct correlation of surface topography with current distribution [21].

The thickness of the thin films can also be estimated by AFM. AFM measures the height of the step created on the sputtered thin film. Before sputtering, the glass

substrate is partially covered by kapton tape, and then sputters the sample up to which the thin film attains the required thickness. Finally peel off the tape and scan the surface topography of the partially coated sample to map the step features.

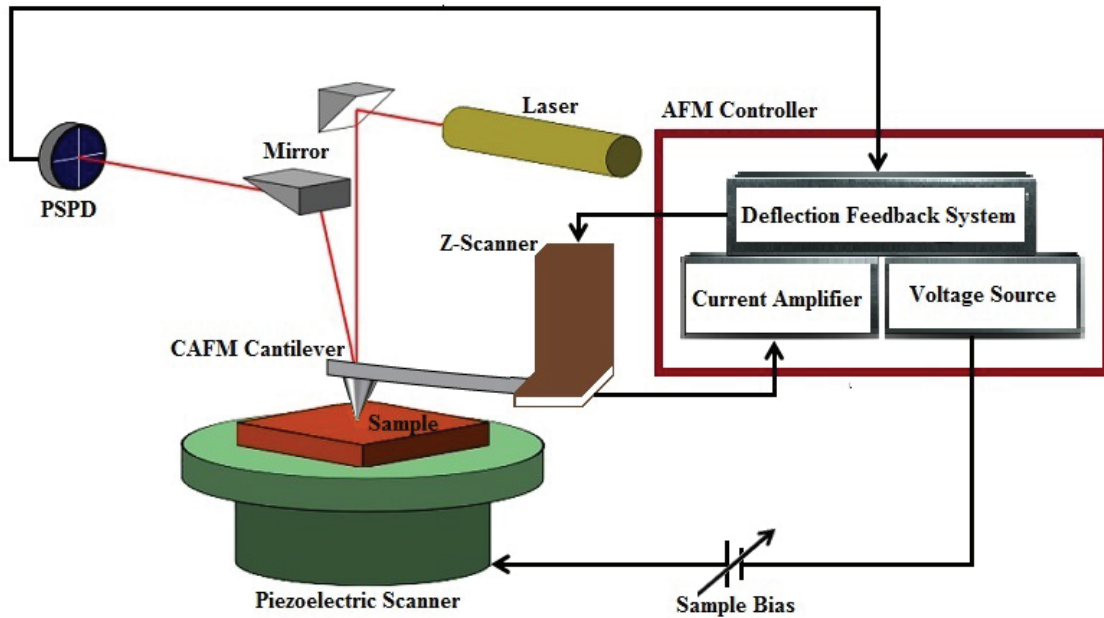


FIGURE 2.10. Schematic representation of CAFM

In this study, the surface and current distribution features were recorded by Bruker-MultiMode 8 AFM and the corresponding profiles are processed and analysed using NanoScope Analysis software. The system has $125\mu\text{m} \times 125\mu\text{m}$ XY and $5\mu\text{m}$ Z scanner with vertical engagement of the probe. The optical microscope with 10X objective is equipped for viewing tip, sample and laser. The linear amplifier of CAFM can sense the currents within the range of 1pA to $1\mu\text{A}$. The surface features were recorded in ScanAsyst mode using silicon nitride probe with reflective aluminium coating on back side. The resonant frequency and spring constant of the probe is 100 KHz and 0.2 N/m respectively. It has a tip radius of 2 nm. The probe which is used for CAFM is antimony (n) doped silicon and coated with platinum-iridium conductive coating on front side and reflective coating on back side. It has resistivity of $0.01\text{-}0.025\ \Omega\text{ cm}$, resonant frequency of 75 KHz and spring constant of 3 N/m . The tip has radius of 25 nm and height of $10\text{-}15\ \mu\text{m}$. The polarity convention of the current is that the positive current means the current is flowing from the sample to the tip and vice versa [22].

2.3.3 Hall measurement

The analysis of electrical and electronic properties of thin films is based on transport parameters of charge carriers. The Hall analysis is considered to be one of the most reliable techniques to yield the carrier transport parameters such as carrier concentration and mobility. When a current carrying conductor is placed in a magnetic field (B) transverse to the direction of current flow (I), a voltage is developed in the direction perpendicular to the plane of the current and the magnetic field. The voltage is known as Hall voltage (V_H) and it is directly proportional to the product of the current density and magnetic induction. It was discovered by Edwin Hall in 1879. If an electric current flows through a conductor in a magnetic field, the magnetic field exerts a transverse force called Lorentz force which curves the path of the moving charge carriers during collision. This leaves equal and opposite charges on the sides of the conductor. The charges accumulate on the faces of the specimen until the electric field associated with it is large enough to cancel the force exerted by the magnetic field. It results in a measurable voltage between the two sides of the conductor. It is schematically represented in the fig. 2.11. The resistance of the material is measured by applying a known current to the one pair of contacts across the conductor and the voltage drop across another diagonal pair is measured. The resistivity (ρ) is estimated from this resistance value by considering the dimension and thickness of the thin film.

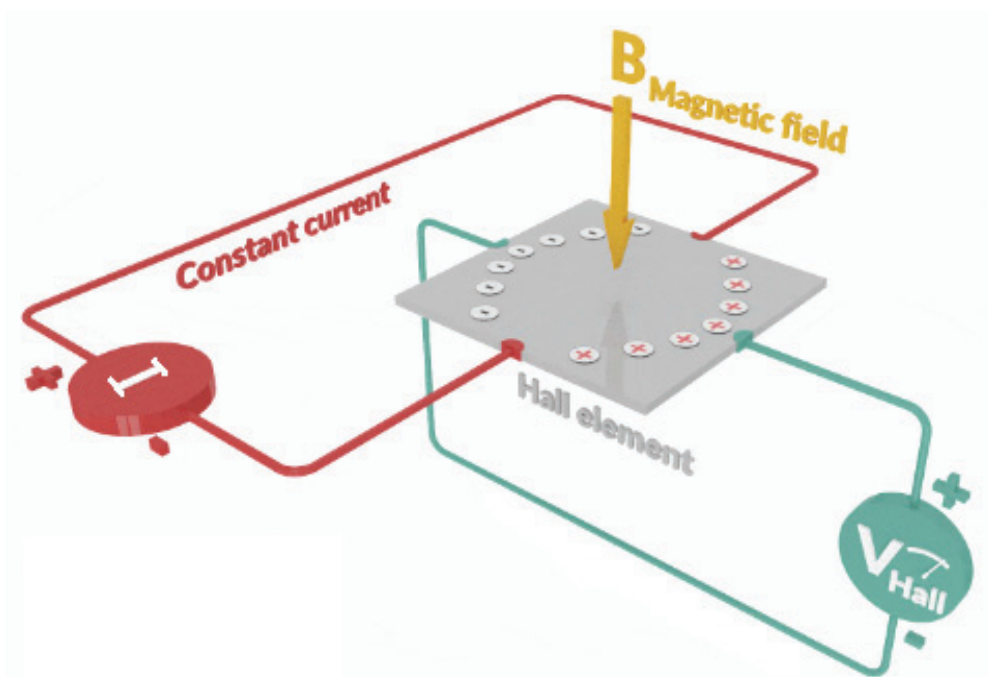


FIGURE 2.11. The schematic representation of Hall effect

The Hall coefficient (R_H) can be estimated by the relation, $R_H = (V_H t) / (I B)$, where t is the thickness of the film. The carrier concentration was calculated from the relation, $n = I / (e R_H)$, where e is the charge of an electron. The mobility of the electrons was also estimated from the determined Hall parameters by the relation $\mu = (R_H / \rho)$, where ρ is the resistivity [24].

2.3.3.1 Instrumentation

In this study of thin films, the carrier concentration and carrier mobility were estimated at room temperature by the Hall measurement system ECOPIA-HMS 3000. It uses four point probe method in the Van der Pauw configuration for the electronic transport parameter analysis. The measurements were performed in square samples of 1 cm dimension by engaging spring loaded gold probes with silver dot contacts at equidistant corners. The magnetic fields are provided by a permanent magnet having flux density of 0.51 Tesla. The system can feed DC input current in the range of 1nA-20 mA according to the resistance of the sample by a constant current source. The range of the resistivity and carrier concentration that can be analysed by the instrument is 10^{-4} - $10^8 \Omega \text{ cm}$ and 10^8 - 10^{22} cm^{-3} respectively [25].

2.3.4 UV-Visible spectroscopy

Spectroscopy is the study of the interaction between matter and electromagnetic radiations. The UV-Visible spectrophotometer provides the transmittance, absorbance and reflectance spectra of a material in UV-Visible range of electromagnetic radiations. When a homogeneous thin film is irradiated with light, the light may either be transmitted (T) through the thin film material in a well-defined direction, specularly reflected (R) or absorbed (A) by the material. In the presence of these phenomena, the energy conservation law may be written as:

$$T + R + A = 1 \quad \dots\dots\dots (2.7)$$

During the light-matter interaction in the thin film, the oscillating electric field polarizes the molecules of the material at the frequency of the incident photon. The field and the induced molecular dipoles become coupled. The net effect is that the polarization mechanism delays the propagation of the electromagnetic wave. The

stronger the interaction between the field and the dipoles, the slower is the propagation of the wave. The ratio of the velocity of light in free space (c) to its velocity in a medium (v) is called the refractive index (n) of the medium:

$$n = c/v \quad \dots\dots\dots (2.8)$$

When light propagates through a plane boundary between two media with different refractive indexes, a reflected wave and a transmitted wave appear in the first and second media, respectively. The irradiance of the reflected waves at normal incidence can be estimated using the following relationship:

$$R = [(n_1 - n_2)/(n_1 + n_2)]^2 \quad \dots\dots\dots (2.9)$$

where n_1 is the refractive index of the first medium, air and n_2 is the refractive index of the second medium, the thin film material. So, R has great dependence on the refractive index of the material of the thin film [26].

The transmitted light intensity decreases exponentially according to the Beer–Lambert law:

$$I(x) = I_0 \exp(-\alpha x) \quad \dots\dots\dots (2.10)$$

where α is the optical absorption coefficient of the material and x is thickness of the thin film. Absorption is the major phenomenon that gives rise to the loss of intensity in the regular direction of propagation. The α of a thin film can be related with the experimental data of T and R in the strong absorption region by a well-known formula:

$$\alpha = \frac{1}{d} \ln \left[\frac{(1-R)^2 + [(1-R)^4 + 4R^2T^2]^{1/2}}{2T} \right] \quad \dots\dots\dots (2.11)$$

where d is the thickness of the film.

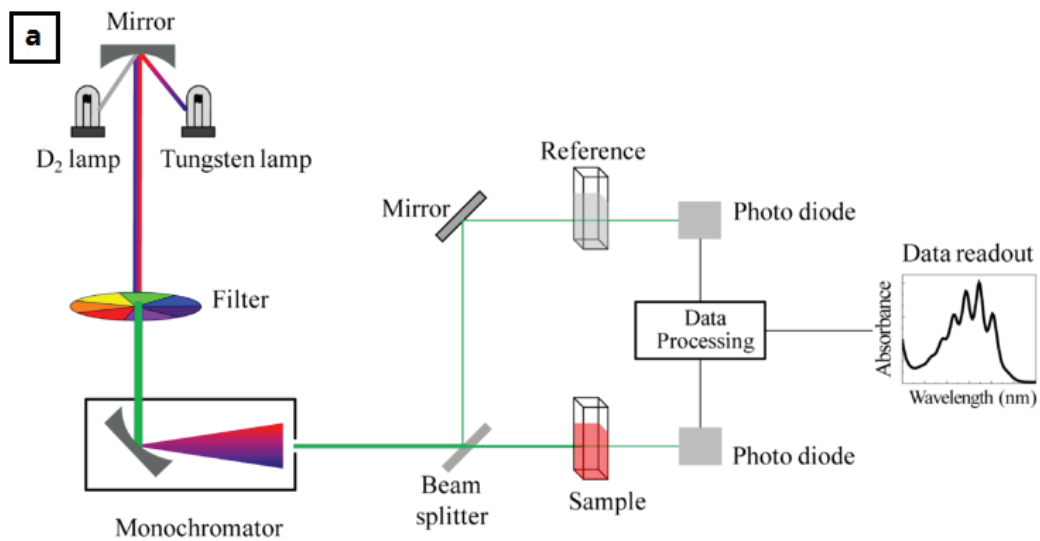
The bandgap (E_g) of the thin films is estimated by Tauc's relationship for the direct transition semiconductors:

$$(\alpha hv)^2 = \alpha_0 (hv - E_g) \dots\dots\dots (2.12)$$

The optical bandgap of the thin film can be estimated by extending the straight line portion of the plot $(\alpha hv)^2$ versus photon energy (hv) to intercept the (hv) -axis at $(\alpha hv)^2 = 0$ [19,27].

2.3.4.1 Instrumentation

The UV-Visible spectroscopy refers to the transmission, absorption or reflection spectroscopy in the ultraviolet-visible spectral region. In double beam spectrophotometer, a beam of light from a source is separated into its component wavelengths by monochromator and then it is separated into two equal intensity beams by a splitter. A series of mirrors is used to get one beam to the reference sample and the other to the sample to be analysed. The ratio of the two measured intensities is usually expressed as percentage of transmittance. In reflectance configuration, an integrating sphere is used to collect the diffused reflections. The ratio of the intensity of the reflected light from the analysed sample to the reference sample is expressed as



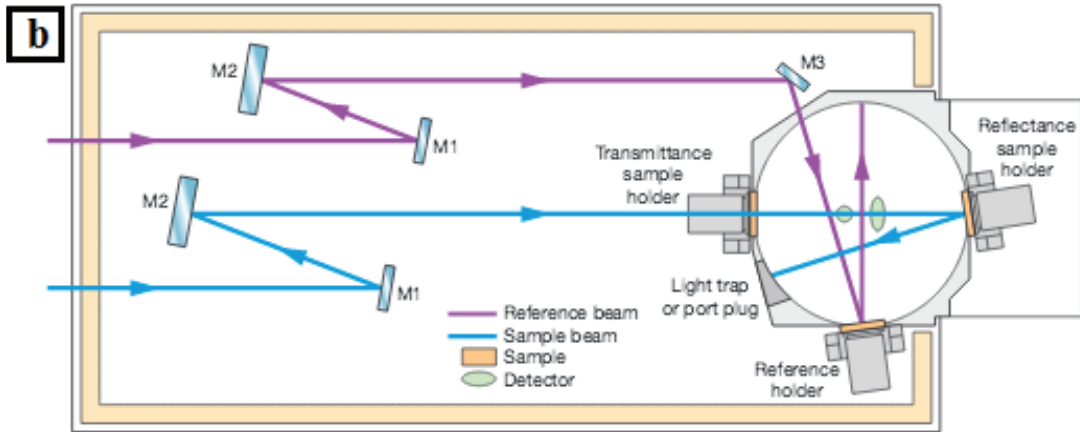


FIGURE 2.12. Schematic representation of (a) transmittance and (b) reflectance configurations of UV-Vis spectrophotometer

percentage reflectance. The schematic representation of the transmittance and reflectance configurations of the UV-Visible spectrophotometer is shown in fig. 2.12 (a) and (b) respectively [28,29]. In this work, the transmittance, absorbance and reflectance spectra of the thin films in the spectral range of 200-1200 nm were recorded using Agilent-Cary 5000 spectrophotometer [30].

2.3.5 Thermoelectric measurement

Measurement of Seebeck coefficient (*S*) and electrical resistivity (*ρ*) over a large temperature range is essential for characterizing thermoelectric materials. The Seebeck coefficient is an open circuit voltage (ΔV) that is created in response to a temperature gradient (ΔT):

$$S = \lim_{\Delta T \rightarrow 0} \frac{\Delta V}{\Delta T} \dots\dots\dots (2.13)$$

The differential method of Seebeck coefficient measurement is more accurate than the integral method. In differential method, the entire sample is heated in steps to successively higher temperatures and for each step small temperature differentials are created between the ends. The linear slope of voltage drop ΔV versus the temperature difference ΔT gives the Seebeck coefficient for the specific temperature. The resistivity of the material is determined by four point probe configuration to reduce

the error in measured values. The resistance of the sample is measured by applying a current at the two ends of the sample and measuring voltage from other two points. The resistivity can be estimated from the measured resistance by considering the dimension and thickness of the thin film samples. The advanced thermoelectric measuring systems usually perform Seebeck coefficient and electrical resistivity measurements simultaneously and hence reduces the measurement time and uncertainty in the measured parameters [31].

2.3.5.1 Instrumentation

In this study, thermoelectric characteristics were analyzed using Seebeck coefficient and electrical resistivity measuring system, ULVAC ZEM-3, M8 which is shown in fig. 2.13 (b). The temperature dependent electrical resistivity and Seebeck coefficient can be simultaneously measured from RT to 800⁰C. The measuring instrument uses standard four probe method to obtain electrical resistivity and static DC method to estimate Seebeck coefficient. The schematic representation of the thermoelectric measuring system is shown in fig. 2.13 (a). The measuring chamber was evacuated and purged the helium gas to supplement the heat transfer from infrared furnace to the sample. The thin film samples were placed in a holder made up of alumina plate and nickel foil. The holder was placed between two electrodes and two spring loaded platinum probe thermocouples. The nickel foils provide the contact between thin film surface and current electrodes. The analysis of the V-I plot ensures the intimate contact between probes and sample surface. The system automatically examines and fixes the best value of electric current for the resistivity measurement. The current is sending through the upper and lower electrodes, while simultaneously measuring the potential difference to obtain electrical resistivity in four probe configuration. The resistivity is calculated using the relation $\rho = R\{(W \times D)/d\}$, where R is the resistance, W is the width, D is the thickness and d is the distance between the probes. It uses ADCMT-6146 as DC current source and KEITHLEY-2010 as multimeter. A heater in the lower electrode provides temperature gradient in the sample to measure the Seebeck coefficient [32]. The Seebeck coefficient of the thin film is estimated by the relation $S = \Delta V / \Delta T$, where ΔV is the difference between lower and upper probe voltages and ΔT is the difference between lower and upper probe

temperatures. In order to minimize the measurement errors, at each measured temperature, the Seebeck coefficient is estimated for different temperature gradient, $\Delta T = 20, 30, 40$. It should be noted that before taking measurement, the samples were heated from RT to the highest temperature which the material can withstand for 3 cycles by using the helium purged infrared furnace. Since, any inhomogeneity of the thin film definitely reflects in the resistance value, the analysis of the measured resistance after each heating cycle gives an indication of the stability of the measuring parameters [33].

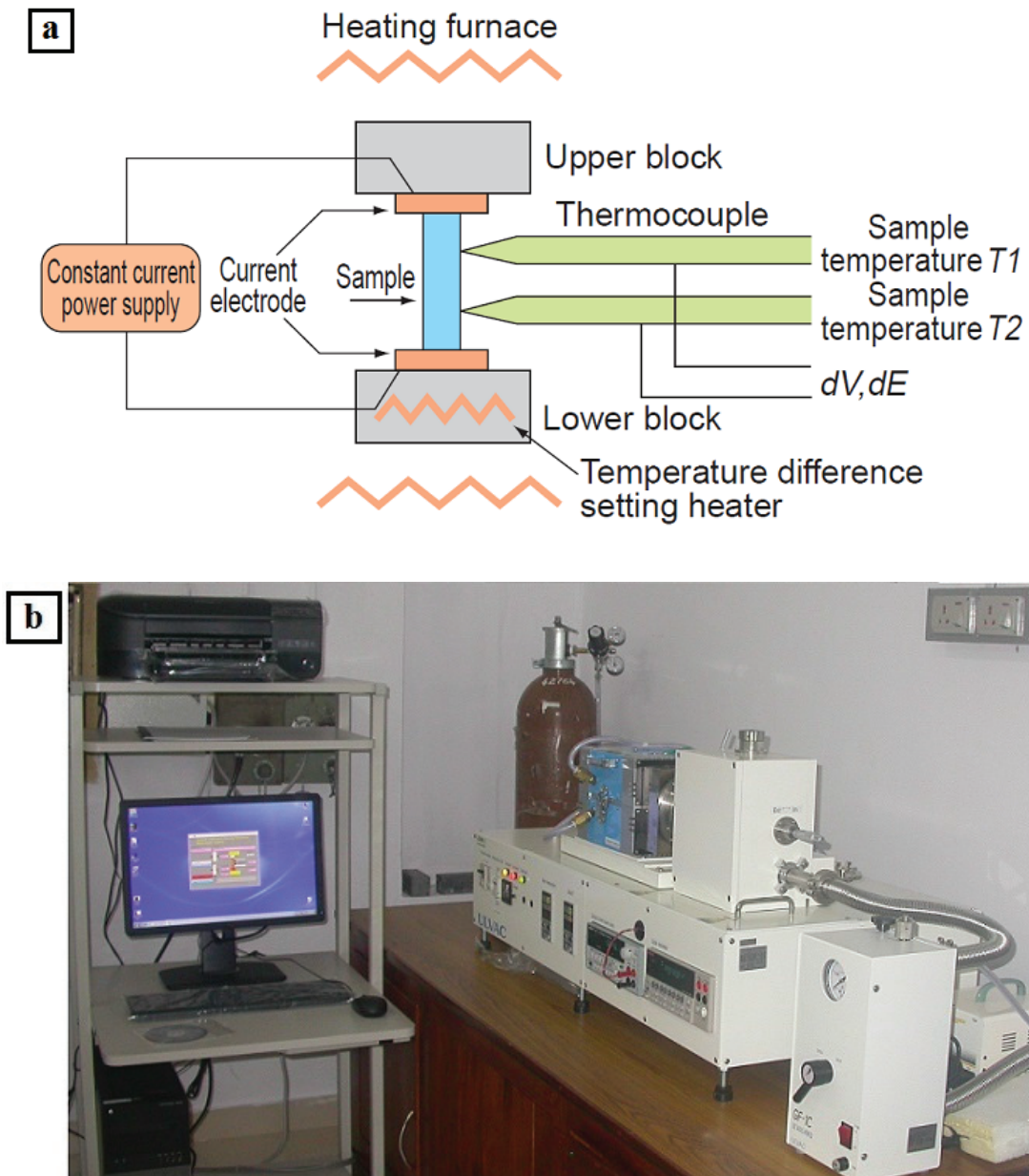


FIGURE 2.13. (a) The schematic representation of probe configuration used in (b) ULVAC ZEM-3 thermoelectric measurement system

2.3.6 Thermoelectric generator characteristics

The measurement of electrical characteristics of the TEGs is necessary to evaluate its energy conversion performance. The open circuit voltage (V_{OC}) is directly proportional to the average Seebeck coefficient (S) of the individual thermoelectric legs and temperature difference (ΔT) between the two ends:

$$V_{OC} = S\Delta T \quad \dots\dots\dots (2.14)$$

The short circuit current (I_{SC}) is proportional to the open circuit voltage and internal resistance (R_{int}) of the generator:

$$I_{SC} = \frac{V_{OC}}{R_{int}} \quad \dots\dots\dots (2.15)$$

Hence, the short circuit current generated from the device is depended on the temperature gradient and measuring temperature of the generator. Then, the variation of output power with temperature difference is the resultant of all the variations in open circuit voltage and short circuit current.

The TEG delivers maximum power (P_{max}) to the external circuit when the load resistance is matched with the device internal resistance. That is:

$$P_{max} = V_{load} I_{load} \quad \dots\dots\dots (2.16)$$

where V_{load} and I_{load} are the output voltage and circuit current respectively when the load resistance is equal to the internal resistance of the generator [34,35].

2.3.6.1 Instrumentation

In this study, the electrical characterization of the thermoelectric generators refers the analysis of the temperature gradient v/s current, voltage and power (ΔT -V, I and P) characteristics. The temperature difference was created by varying the hot side temperature from 50-250⁰C while maintaining the cold side at room temperature. The device operating voltage and power output as a function of electrical current (I-V and P) at matched load were estimated by varying the external load resistance. The measurements were performed by a customized instrumental setup as shown in fig. 2.14. It continuously senses the temperatures by thermocouples and it can be

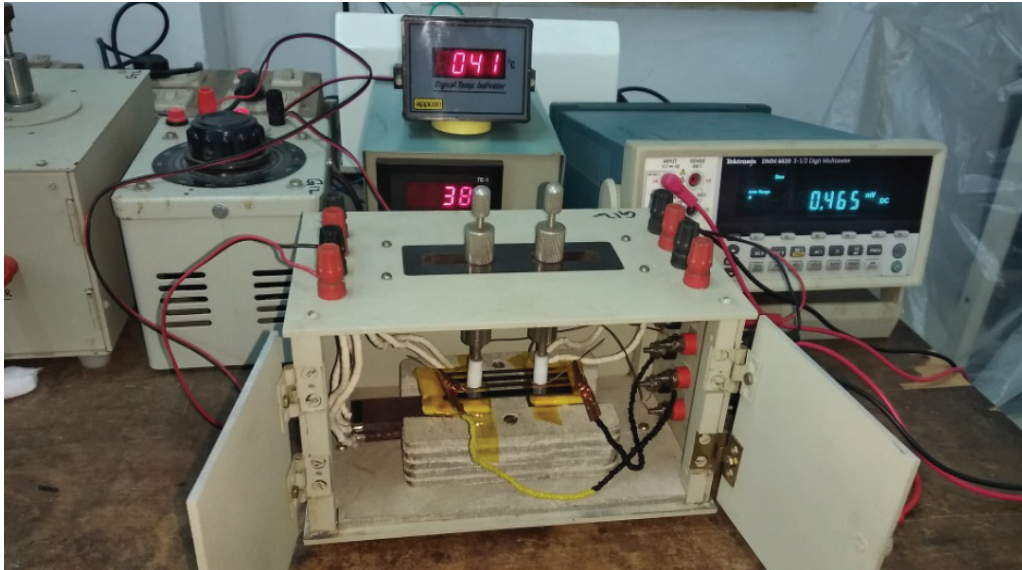


FIGURE 2.14. The electrical characterization system for thin film thermoelectric generators monitored by the temperature display system. The measurement leads are connected to multimeter by spring loaded copper probes to estimate the voltages and currents.

References

- [1] P.M. Martin, Handbook of deposition technologies for films and coatings: Science, applications and technology, Elsevier, U.K. (2010).
- [2] W.R. Grove, Philos. Trans. R. Soc. Lond. 142 (1852) 87-101.
- [3] K. Seshan, Handbook of thin film deposition processes and techniques: Principles, methods, equipments, and applications, Noyes Publications, U.S.A. (2002).
- [4] A. Iles, N. Pamme, Encyclopedia of microfluidics and nanofluidics: Sputtering for film deposition, Springer, U.S.A. (2014) 1-9.
- [5] I. Petrov, P.B. Barna, L. Hultman, J.E. Greene, J. Vac. Sci. Technol. A 21 (2003) S117-S128.
- [6] E. Alfonso, J. Olaya, and G. Cubillos, Crystallization-Science and technology: Thin film growth through sputtering technique and its applications, IntechOpen (2011) 397-432.
- [7] R.F. Bunshah, Handbook of deposition technologies for films and coatings: Science, technology and applications, Noyes Publications, U.S.A., (1994).
- [8] P.B. Barna, M. Adamik, Thin Solid Films 317 (1998) 27-33.
- [9] K.D. Leaver, B.N. Chapman, Thin films, Wykeham Publications, U.K. (1971).
- [10] J.A. Thornton, J. Vac. Sci. Tech. 11 (1974) 666-670.
- [11] R. Messier, A.P. Giri, R.A. Roy, J. Vac. Sci. Tech. A 2 (1984) 500-503.
- [12] P.K. Rol, D. Onderdelinden, Kistemaker, Some physical aspects of sputtering,

- Pergamon Press, U.S.A. (1965).
- [13] M. Lannoo, J. Bourngoin, Point defects in semiconductors-I: Theoretical aspect, Springer, U.S.A. (1981).
- [14] J.E. Greene, A.H. Eltoukhy, Surf. Interface Anal. 3 (1981) 34-54.
- [15] B.D. Cullity, Elements of X-ray diffraction, Addison-Wesley, U.S.A. (1956).
- [16] <https://www.microscopy.ethz.ch/bragg.htm>.
- [17] D. Kriegner, Z. Matej, R. Kuzel, V. Holy, J. Appl. Cryst. 48 (2015) 613–618.
- [18] A. Sasaki, A. Himeda, H. Konaka, N. Muroyama, The Rigaku Journal 26 (2010) 10–14.
- [19] E.N. Kaufmann, Characterization of materials, John Wiley & Sons, U.S.A. (2003).
- [20] Ionescu-Zanetti, A. Mechler, Applications of conductive atomic force microscopy, John Wiley & Sons, U.K. (2005).
- [21] R.A. Oliver, Rep. Prog. Phys. 71 (2008) 076501.
- [22] Bruker, Application modules: Dimensions and multimode manual, Bruker Corporation, U.S.A. (2011).
- [23] <https://www.melexis.com/en/articles/hall-effect>.
- [24] C. Kittel, Introduction to solid state physics, John Wiley & Sons, U.S.A. (2005).
- [25] Ecopia, Manual: Hall effect measurement system, Ecopia, South Korea (2015).
- [26] S.O. Kasap, Principles of electronic materials and devices, McGraw-Hill, U.S.A. (2006).
- [27] M. El-hagary, M. Emam-ismail, E.R. Shaaban, A. El-taher, Radiat. Phys. Chem. 81 (2012) 1572–1577.
- [28] https://en.wikibooks.org/wiki/Methods_and_Concepts_in_the_Life_Sciences/Spectroscopy.
- [29] https://www.perkinelmer.com/CMSResources/Images/44-74191APP_LAMBD A650IntegratingSpheres.pdf.
- [30] Agilent, Manual: Cary 5000 Spectrophotometers, Agilent Technologies, Australia (2016).
- [31] D.M. Rowe, CRC Handbook of thermoelectrics, CRC Press, New York (1995)
- [32] Riko, Manual: ZEM-3(M8) Seebeck coefficient and electric resistance measurement system, Advance Riko, Japan (2018).
- [33] S. Shafeie, S. Guo, Q. Hu, H. Fahlquist, P. Erhart, A. Palmqvist, J. Appl. Phys. 118 (2015) 184905.
- [34] L. Kütt, J. Millar, A. Karttunen, M. Lehtonen, M. Karppinen, Renew. Sustain. Energy Rev. 98 (2017) 519-544.
- [35] A. Montecucco, J. Siviter, A. Knox, Appl. Energy 123 (2014) 47-54.

ENHANCEMENT OF THERMOELECTRIC PROPERTIES OF TIN NITRIDE THIN FILMS BY BAND CONVERGENCE

Contents

-
- 3.1 Introduction
 - 3.2 Fabrication of thin films
 - 3.3 Results
 - 3.4 Discussion
 - 3.5 Conclusion
-

The enhancement of thermoelectric power factor of tin nitride thin films by conduction band convergence is reported in this chapter. It also deals with the characterizations employed to explore the physical aspects behind the correlation between thermoelectric properties and band parameters.

3.1 Introduction

Nitride materials are diverse class of compounds having wide uses in industry and holding important role in material science research. The moderate electronegativity of the nitrogen atom offers mixed covalent and ionic bonding features to nitrides. It is more ionic than other pnictides and more covalent than oxides. The ionic and covalent characteristics result in greater structural viability and better electronic transport properties respectively [1]. Gallium nitride as well as the other III-nitrides like aluminium and indium nitrides attracts much attention of researchers. Considering the systematic and extensive exploration of III-nitrides, their nearest neighbors, IV-nitrides are relatively unexplored. Group IV nitrides usually attain IV_3N_4 stoichiometry and show viable charge transport properties for various semiconducting applications. Even if the physical properties of silicon, germanium and carbon nitrides are well investigated, limited literatures are available on semiconducting properties of tin nitride (Sn_3N_4). The binary compounds of tin based on oxygen, sulfur and fluorine are studied systematically but tin nitride is much less known. Hence, it provides an opportunity to explore the extreme of various physical properties by tuning structural and electronic features. So, it is very interesting in the perspective of basic science [2].

Tin nitride is a stable IV-V semiconductor made up of earth abundant and non-toxic constituent elements. It crystallizes in the $MgAl_2O_4$ -spinel structure with space group $Fd\bar{3}m$. Normally spinel structures are cubic close-packed with eight tetrahedral and four octahedral sites per unit formula. Tin has two different sites in this compound with oxidation state of $+4$, four nitrogen atoms surrounded with a distance of 2.06 \AA at one site and six nitrogen atoms with 2.17 \AA radial distance at the other site. It has eight formula unit per unit cell with lattice constant, $a = 9.037 \text{ \AA}$ [3]. The crystal structure of Sn_3N_4 is shown in fig. 3.1 [4]. Two representations of tin nitride, Sn_3N_4 and Sn_xN_z , are available in the ICDD PDF database with ICDD No. 01-070-3184 and 00-050-0553 respectively [5]. The Bragg angles correspond to the reflection planes in both the data are same and keen observation of the diffraction patterns indicates that both compounds are Sn_3N_4 with a different crystallographic orientation. The Sn_xN_z compound changes the preferred orientation (PO) from (311) to (222) in comparison with Sn_3N_4 . It is often observed that changes in orientation in

nitride thin films depend on variations in growth parameters such as temperature and pressure. The detailed structure studies of the tin nitride compounds by Caskey and Zakutayev also explored this matter [6].

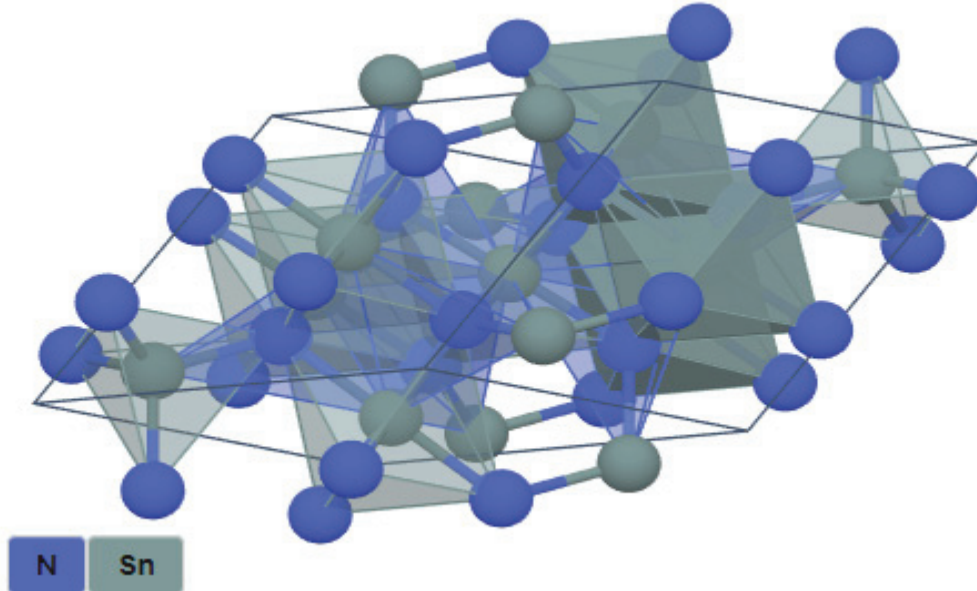


FIGURE 3.1. Crystal structure of Sn_3N_4 compound

Sn_3N_4 is a degenerate semiconductor with n-type conductivity. The electronic band structure of spinel Sn_3N_4 along with other group 14 nitrides were investigated by W.Y. Ching et al. and I-H. Chu et al. using first principle calculations and local density approximation respectively [7,8]. The studies revealed that, Sn_3N_4 having the smallest direct band gap of 1.4 eV at Γ -point among group 14 nitrides. The bottom of the conduction band consists of single band unlike other nitrides having multiple bands. Hence, the higher conduction bands can be easily converged at a point with the bottom conduction band by tuning band parameters. The single band has very low effective mass at the conduction band minimum which is an excellent figure for various charge transport property applications. Also, the defect chemistry of Sn_3N_4 associated with vacancies, interstitials and antisites has a favorable nature for the improvement of electronic transport properties. But, the reported values of physical parameters of Sn_3N_4 thin films are not consistent. It shows bandgap ranging from 1-2.25 eV, carrier concentration of 10^{16} - 10^{20} and conductivity of 10^{-2} - 10^3 S/m based on various experimental and theoretical investigations [1,2,6–8]. These disparities can be

ascribed to the variations in the features associated with the crystal structure, microstructure, surface and charge carriers. Most of the prominent metal nitride thin films exhibit large variations in crystallographic orientation, defect, surface topography and carrier concentration with deposition conditions [9–11]. Hence, tuning of physical properties can be easily achieved by controlling the growth parameters of Sn_3N_4 compound.

The enhancement of power factor succeeds only when the tradeoff between electrical conductivity and Seebeck coefficient become optimum. Generally, the increase in carrier concentration improves conductivity, but also results a decrease in Seebeck coefficient and the band engineering can improve conductivity and Seebeck, but not simultaneously [12,13]. The band convergence and flattening are the main band engineering techniques exploit to improve the Seebeck coefficient. The band convergence enhances Seebeck coefficient without substantially degrading the conductivity, but band flattening leads to conductivity reduction. However, both methods have relevance in the optimization of thermoelectric parameters. Among the various strategies, enhancing the DOS by increasing the valley degeneracy of the conduction bands has been adopted in this work to improve the energy conversion capability. The increase in conduction band valleys takes part in the transport mechanism is originated from the convergence of the conduction bands at a particular energy by band structure modification. This is the only way to enhance the DOS near the Fermi energy without reducing the mobility [14,15].

Tin nitride (Sn_3N_4) is a semiconductor made up of earth abundant and non-toxic constituent elements. Its crystallographic, electronic and optical properties are well suitable for thermoelectric applications. Considering the band structure, the second conduction band can be easily converged to the bottom conduction band at Γ -point by tuning band parameters. The convergence of the conduction bands can be stimulated by optimizing the bandgap and orientation of crystallites of the thin films. In this chapter, the enhancement of thermoelectric power factor of Sn_3N_4 thin films by conduction band convergence is reported. It discusses the experimental strategy to precisely tune the defect chemistry and growth kinetics of crystallites of the thin films for the optimization of bandgap and PO. It also deals with the characterizations employed to explore the basic mechanisms behind the enhancement of thermoelectric power factor.

3.2 Fabrication of preferentially oriented Sn₃N₄ thin films

The Sn₃N₄ thin films were deposited on glass substrates with dimension 10x10x1 mm using reactive RF magnetron sputtering with a 99.99% pure tin target of 50 mm in diameter and 4 mm thick. Before the deposition, the glass substrates were cleaned by standard solution cleaning method followed by ultrasonic cleaning in acetone and finally dried in an oven [16]. We carried out different analysis based on the various deposition parameters which determine the physical properties of the thin film. The effect of substrate temperature and sputtering power on structural and electrical properties of the Sn₃N₄ thin film were investigated. These studies provided a precise picture of parameter-property correlation. From these results, we optimized the deposition parameters of Sn₃N₄ thin films for thermoelectric analysis.

TABLE 3.1. The optimized deposition parameters for Sn₃N₄ reactive sputtering

Parameter	Specification
Fabrication Technique	Reactive RF magnetron sputtering
Target	Sn 99.99% pure and 50x4 mm size
Substrate	Glass with 99.999% pure and 10x10x1mm
Sputtering & Reactive Gas	Nitrogen
Target-Substrate Distance	8 cm
Sputtering Power	150 W
Substrate Temperature	250 ⁰ C
Ultimate Vacuum	6x10 ⁻⁶ mbar
Working Pressure	4x10 ⁻³ - 4x10 ⁻² mbar
Film Thickness	~250 nm

Nitrogen gas with 99.999% pure was used as both sputtering and reactive gas. The separation distance between the substrate and the target was fixed as 80 mm. The base pressure was about 6x10⁻⁶ mbar before the entry of N₂ gas into the chamber. For all the deposited films, the base pressure, sputtering power of 150W, substrate temperature of 250⁰C and thickness of ~250 nm were kept constant while sputtering pressure was set to different values. Since the interference fringes is absent in the thin films of thickness 250 nm, thin films having thickness of ~ 950 nm was fabricated for

optical characterizations with the same optimized sputtering parameters. Before conducting the reactive sputtering, the chamber was evacuated to ultimate vacuum of 6×10^{-6} mbar, purging the N_2 gas in to the chamber and control for different sputtering pressures in between 4×10^{-3} mbar and 4×10^{-2} mbar. The reduction in N_2 gas pressure of reactive sputtering reduced both working pressure and amount of reactive nitrogen. The thin film deposition continued up to which the quartz crystal thickness monitor showing the required thickness. Table 3.1 shows the optimized deposition parameters for Sn_3N_4 reactive sputtering.

3.3 Results

3.3.1 Phase and crystallographic features

The X-ray diffraction technique was employed to analyze the phase and crystallographic features. The XRD patterns of Sn_3N_4 thin films deposited at different N_2 gas pressure are shown in fig. 3.2. The comparison of the diffractogram with standard ICDD data (ICDD No. 01-070-3184) ensures the evolution of Sn_3N_4 phase in all the reactively sputtered thin films. It is shown that the prepared Sn_3N_4 thin films were polycrystalline and in the cubic phase with space group $Fd\bar{3}m$ [4]. The peaks of metallic or oxide phases were not detected, indicating that the sputtered Sn atoms almost completely reacted with N_2 gas. The absence of any unassigned extra peak eliminates the possibility for the presence of other phases of Sn-N system. Also, there is no any overlapping peak in the standard data of different phases of Sn-N system. Hence, the prepared thin films can be considered as a single phase of Sn_3N_4 . The major XRD peaks were observed with diffractions of (111), (220), (311) and (222) planes. The variations in the intensities of the diffraction planes were observed for thin films deposited at various N_2 gas pressure. At highest N_2 gas pressure, the diffractions of (311) plane around 32.5° was dominant. When decreasing N_2 gas pressure, intensities of the all peaks were increased with sustaining (311) PO up to the N_2 gas pressure of 2×10^{-2} mbar. Further decrease in N_2 gas pressure to lower values decreased the intensity of (311) diffraction and gradually increased the (222) and (111) diffraction intensities. The thin films sputtered at these N_2 gas pressures have POs along (222) and (111) planes around 33.8° and 16.7° respectively. The increase in total

intensity of the reflections from all planes with decreasing N₂ gas pressure ensured the improved crystallinity of the Sn₃N₄ thin films with PO [17].

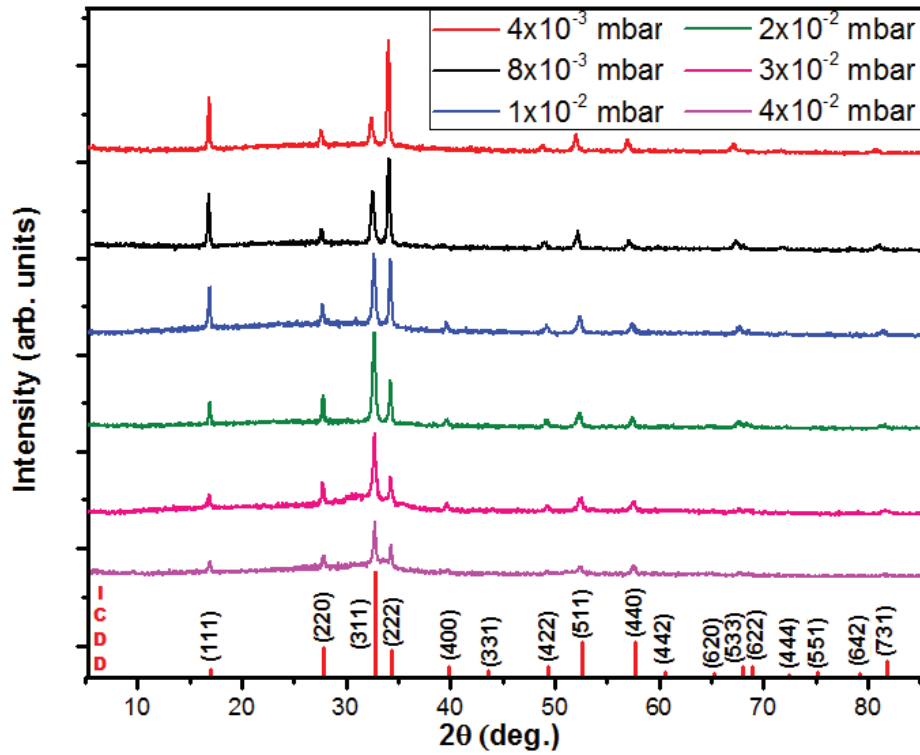


FIGURE 3.2. XRD of sputtered Sn₃N₄ thin films having varying PO with N₂ pressure

The characteristic of the PO of a thin film can be identified by the texture coefficient (TC), which is obtained from the diffractions of (hkl) plane by the equation 3.1, [18]

$$TC_{(hkl)} = \frac{\frac{I_{(hkl)}}{I_0(hkl)}}{\frac{1}{n} \sum_{i=1}^n \frac{I_{(hkl)}}{I_0(hkl)}} \dots\dots\dots (3.1)$$

where, I is the measured intensity, I₀ is the ICDD standard intensity of the Sn₃N₄ compound, and n is the number of (hkl) diffraction peaks considered for analysis. The deviation of TC from unity corresponds to the change in orientation of the planes. The TC greater than unity indicates that the particular crystallographic direction is preferentially oriented and it less than unity realizes that the particular growth orientation is selectively avoided. The presence of PO along a particular plane implying an enhancement in the number of grains along that plane [19]. The TC of the

two major diffraction planes, (311) and (222) is shown in fig. 3.3 (a) for different N₂ gas pressure.

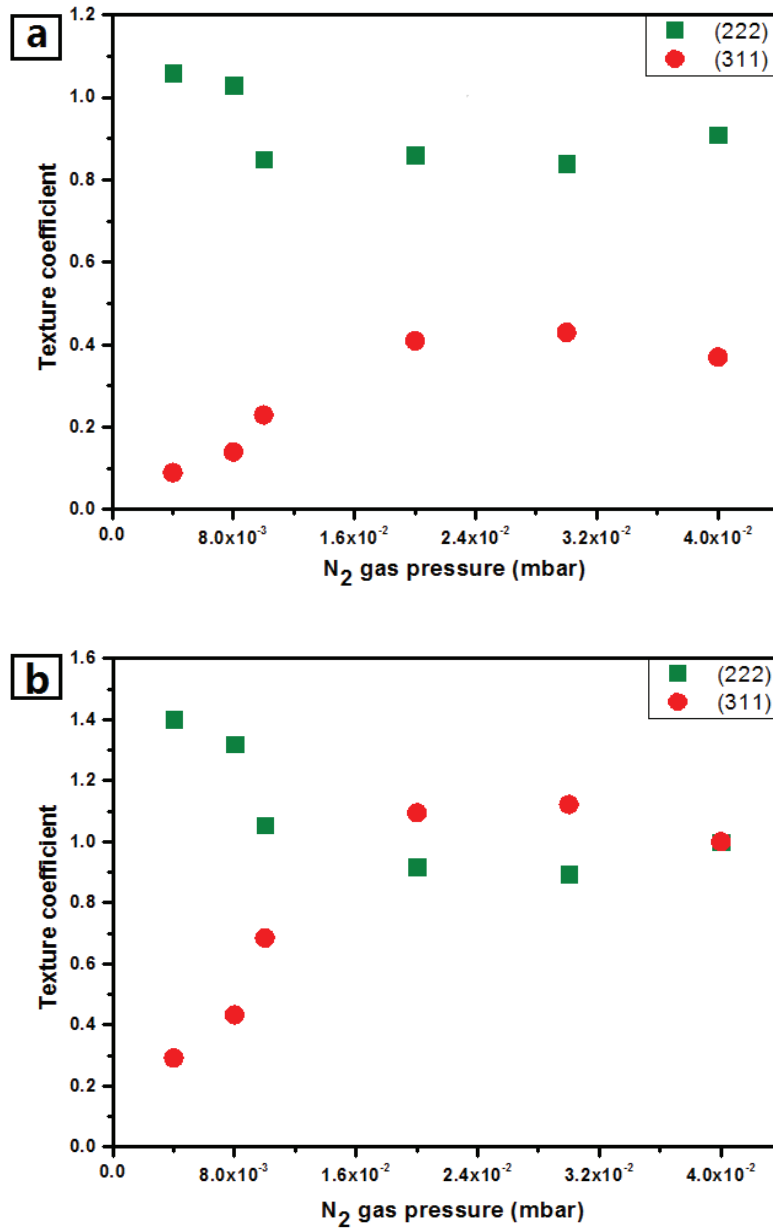


FIGURE 3.3. Texture Coefficient of Sn₃N₄ thin films with reference to (a) ICDD file (b) XRD data of thin film sputtered at 4x10⁻² mbar

These TC calculations were made with ICDD file of Sn₃N₄ as reference, which already has a PO along (311) plane. It affects the proper correlation of PO and TC with variation in N₂ gas pressure and hence, obscures the proper interpretation of the various results of the prepared thin films based on PO and TC. In order to overcome this, TCs were recalculated using the XRD intensities of Sn₃N₄ thin film prepared at

4×10^{-2} mbar pressure as reference. The TC of planes (311) and (222) are then plotted as a function of pressure as shown fig. 3.3 (b). It gives a proper correlation between TC and PO. The TC of (311) decreased and that of (111) and (222) increased with the decrease in pressure.

The plane of self assembly or orientation is usually observed in three dimensional growth of crystalline materials. In thin films, the orientation of planes has strong influence on its physical characteristics. The ordering of atoms highly depends on variations of growth parameters like temperature, pressure, etc [20]. The PO is considered as an entropy lowering phenomenon subjected to the variations in growth parameters. The thin film overall energy should includes interfacial, surface and strain energies. Once the thin film material and substrate are determined, the deposition conditions have fewer effects on interfacial energy. Therefore, the origin and variations of PO in Sn_3N_4 thin film can be assigned to the competition between surface and strain energies during the growth of the film. The developed strain energies are proportional to the energy of the bombarding particles striking on the surface [10,11,21]. The variations in strain energy and overall energy of the planes (311) and (222) are schematically represented in fig. 3.4.

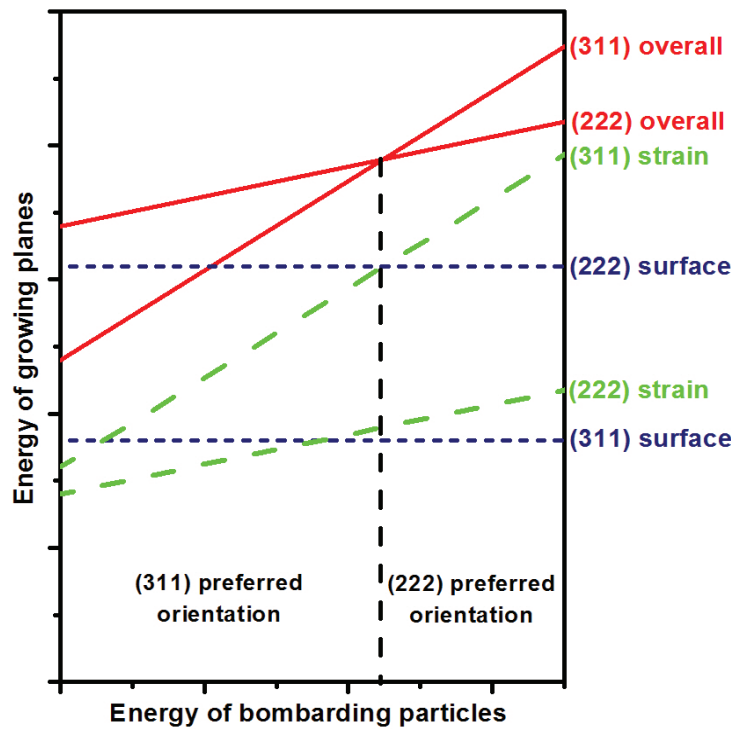


FIGURE 3.4. Variation of preferred orientation of Sn_3N_4 thin film with the energy of bombarding particles

At high nitrogen gas pressure, due to more number of collisions, the energy of the sputtered species arriving on the film will be low. Hence, the overall energy of the film mainly depended on the surface energy. The (311) planes of the Sn_3N_4 have the lowest surface energy which led to the growth of energetically favorable (311) oriented Sn_3N_4 thin film. When the nitrogen gas pressure decreases, the average energy of the sputtered species arrived at the film surface increases. It developed an increase in strain energy of the planes and the overall energy of the film was largely controlled by strain energy. The adatom on the film surface would be arranged in a plane with the lowest strain energy to minimize the overall energy of the film [20]. The lower strain energy density for (222) leads to an orientation along (222) rather than in (311) direction. The high strain energy of (311) plane originated from the difference in the increasing rate of strain energies of (311) and (222) planes due to anisotropy of the elastic moduli [11,22].

3.3.2. Electronic transport parameters

At higher N_2 gas pressure during the growth of thin films, more number of nitrogen atoms is available for the reaction; hence the nitrogen concentration in the thin film reaches to the stoichiometry of Sn_3N_4 . Reduction in N_2 gas pressure creates N_2 deficient atmosphere for reactive sputtering. It creates donor type defects such as nitrogen vacancy and tin interstitial. The nitrogen vacancy, V_N , in Sn_3N_4 , induces states, which can be neutralized with three holes; hence, the nitrogen vacancy acting as a triple donor. The excess tin can be occupied at the interstitial sites of the Sn_3N_4 compound. This interstitial tin defect, Sn_i , induces a state in conduction band with four electrons and it always donates four electrons to conduction band and acting as donors. Hence, the carrier concentration of sub-stoichiometric Sn_3N_4 thin films is increased. The carrier concentration gradually increases with defect density [23,24]. The variation of carrier concentration and mobility with N_2 gas pressure is shown in fig. 3.5. The slight reduction in mobility is attributed to the low dominance of defect scattering in presence of improved crystallinity and grain boundary formation. The variations in mobility reduction show that it is mainly influenced by variations in carrier concentration.

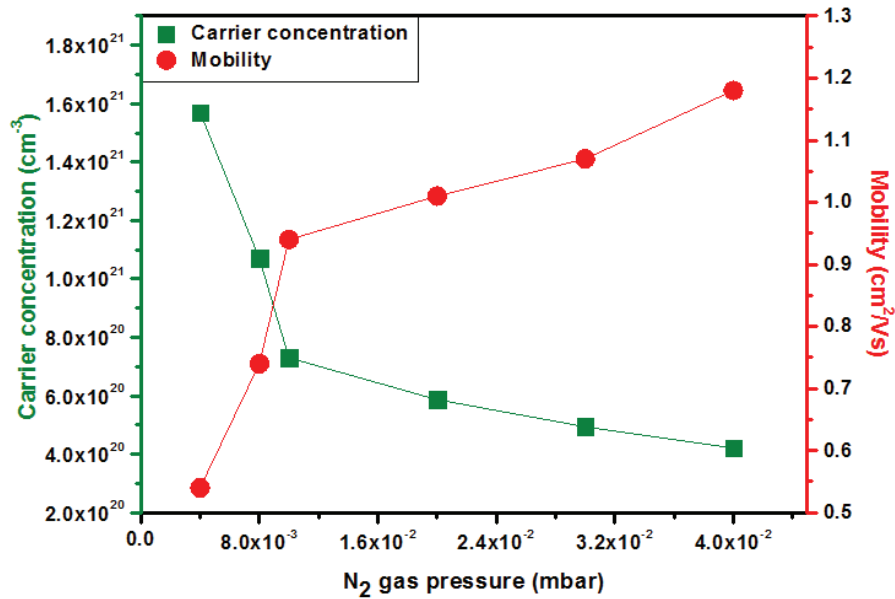


FIGURE 3.5. Variation of carrier concentration and mobility of Sn₃N₄ thin films with N₂ gas pressure

3.3.3 Thermoelectric properties

Thermoelectric power factor is determined by the Seebeck coefficient (S) and electrical conductivity (σ) of the material. The conductivity is the reciprocal of resistivity (ρ) and can be determined by the relation, $\sigma = 1/\rho$. The temperature depended thermoelectric properties of the prepared Sn₃N₄ thin films from RT to 250⁰C were shown in fig. 3.6. When decreasing the nitrogen gas pressure of sputtering process, both the resistivity and Seebeck coefficient are decreasing up to 2x10⁻² mbar pressure of nitrogen. This behavior of the parameters is usual and it decreased the power factor of the material [14,25]. The decrease in nitrogen gas pressure from 2x10⁻² mbar to 4x10⁻³ mbar, the resistivity follows the decreasing nature, while the Seebeck coefficient is in an increasing state. This unusual behavior of the parameters favors the enhancement of power factor. The thin film sputtered at the pressure of 4x10⁻³ mbar achieved a maximum power factor of 390 μ W/m K² at 250⁰C with Seebeck coefficient of -144 μ V/K and resistivity of 53.11 $\mu\Omega$ m. The prepared thin films show the negative temperature coefficient of resistance, which reveals the semiconductor nature of Sn₃N₄. The Seebeck coefficient increases with temperature and found to be negative in the entire temperature range under the investigation, suggesting that the electrons are the majority carriers in the thermoelectric transport [25].

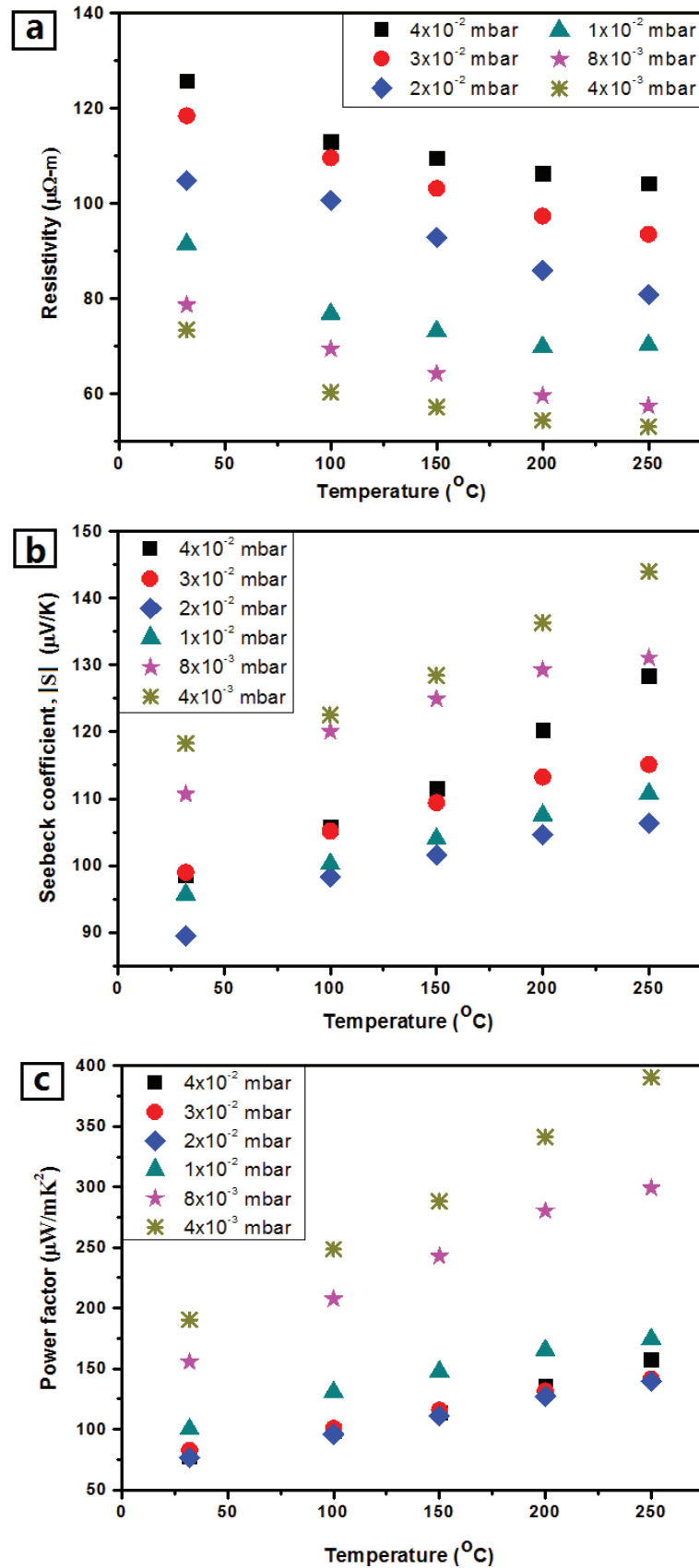


FIGURE 3.6. Temperature dependent (a) resistivity (b) Seebeck coefficient and (c) power factor of Sn_3N_4 thin films sputtered at different N_2 pressure

3.3.4 Surface features

The integration of optical properties with the thermoelectric parameters can be effectively employed to elucidate the precise mechanism behind the band convergence. For this, the Sn_3N_4 thin films having thickness of ~ 950 nm were fabricated at various N_2 gas pressures using the same optimized sputtering parameters given in table 3.1. The thickness of the thin films was estimated by AFM [26]. AFM measured the height of the step created on the sputtered thin film as shown in fig. 3.7.

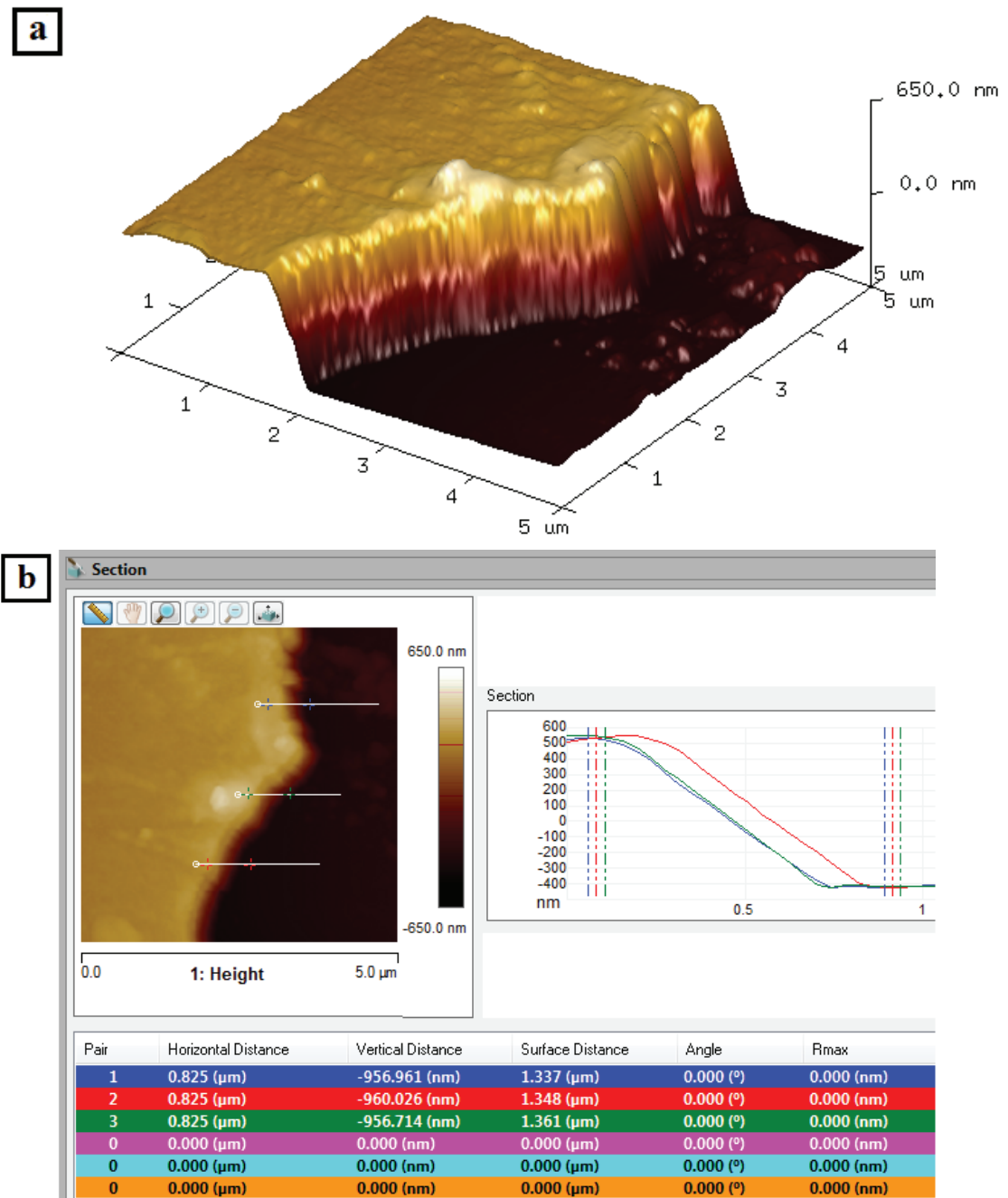


FIGURE 3.7. (a) Surface topography and (b) thickness analysis of the partially coated Sn_3N_4 thin film

Any variations in optical parameters can be attributed to the material properties of the thin films, especially surface and microstructural features. This can be obtained by the AFM analysis. During the decrease in nitrogen gas pressure, the total working pressure of reactive sputtering is decreased from 4×10^{-2} mbar to lower values. With the decrease in sputtering pressure, the grain morphology and microstructure will change. The gradual changes in microstructure and grain morphology from spherical to worm-like structure are clearly observable in AFM images shown in fig 3.8. In thin films sputtered at high pressure, the energy and mobility of the adatom is very low due to high collisions. Hence, the adsorbed particles will rest in the position at which they arrive. The inefficiency of the adatoms in overcoming the energy barrier creates tapered fibrous crystallites with small size due to the intergrain shading effect as shown in fig. 3.8 (a). In this growth formalism, the separations between grains are voids instead of grain boundaries and the films have low density and high porosity. This type of crystallites offer high surface roughness to the growing film and poor electrical conductivity [27]. When the energy of the sputtered atoms is increased due to decreased collisions by decreasing the N_2 gas pressure, surface mobility of the adatoms improves. Then the adsorbed atoms can move slightly from their initial arriving positions. This increases the size and reduces the height of the tapered crystallites as shown in fig. 3.8 (b) and (c). However, migration of the adsorbed particles between grains is not possible due to low energy per incident particle. This results in the growth of more tightly packed fibrous grains with weak grain boundaries and decreases the surface roughness of the growing layers of the film. This growth formalism improves the density and conductivity of the sputtered films compared to the previous ones [20,28].

At low pressure, surface mobility significantly improves due to increased energy of adsorbed atoms. The bombardment of the energetic particles destroys the overhang structures rather than growing. This reduces the density of tall crystallites in the growing surface of the film and creates a two-level surface as exhibited in fig. 3.8 (d) and this increases the surface roughness [27]. Here also we expect a gradual improvement of density due to increased grain size and decreased intergrain shading. Further decreases in N_2 gas pressure offer a great amount of energy to the adsorbed atoms and hence high mobility and surface diffusion. The bombardment of high energy particles completely destroys the tall crystallites and grain boundary migration

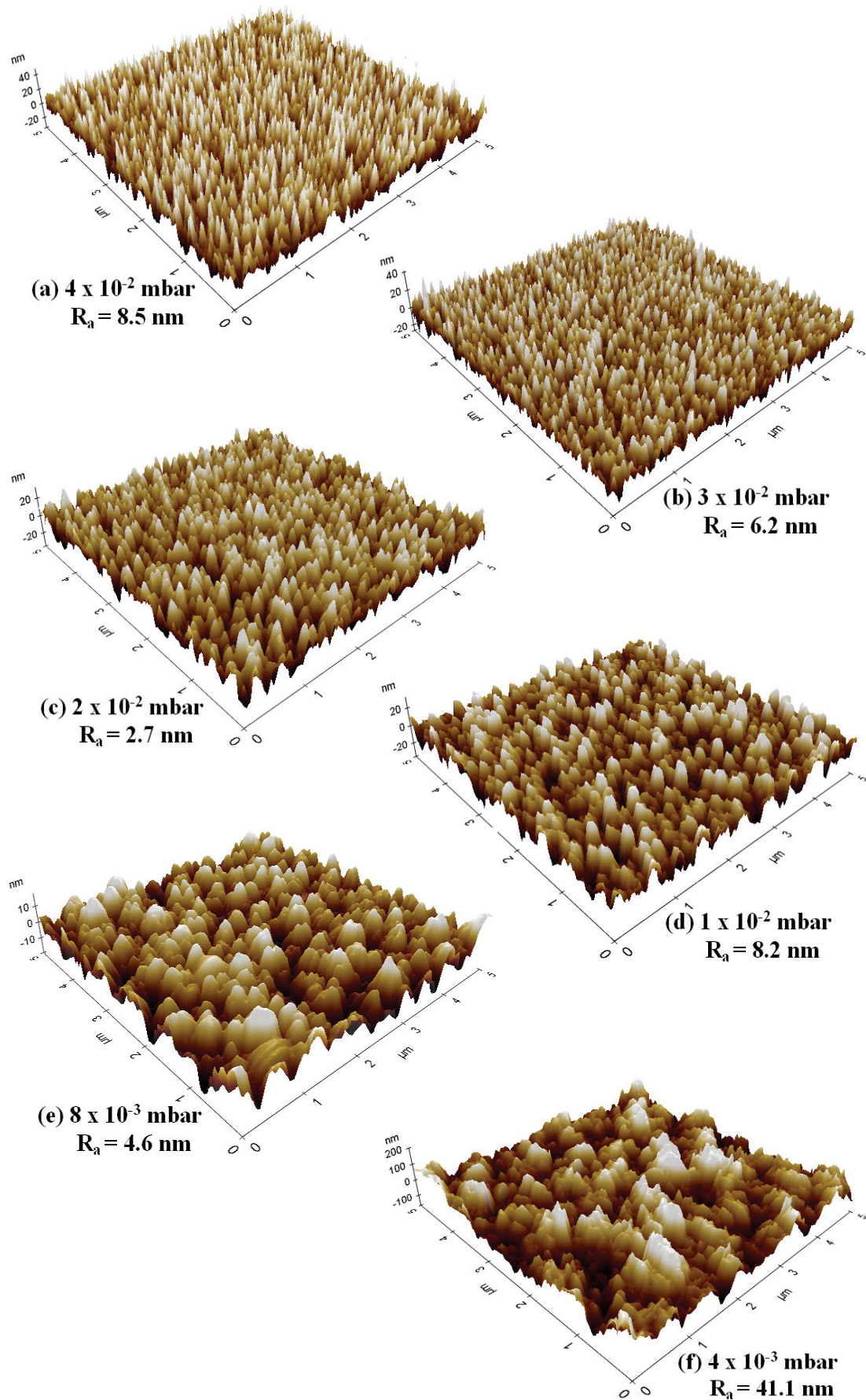


FIGURE 3.8. AFM 3D images of sputtered Sn₃N₄ thin films with average surface roughness

is possible upon impingement of the two grains. The true intercrystalline boundaries start to develop instead of voided grain boundaries. The prepared thin films transform to microstructures consisting of flat columnar grains with high density and low surface roughness as shown in fig. 3.8 (e). Also, the scattering effect on conductive electrons by true grain boundaries is less than that offered by voids. These factors lead to significant improvement in electrical conductivity of growing thin films [27,29,30]. The size of the columnar grains increases as N₂ gas pressure decreases. Finally, at the lowest pressure of 4×10^{-3} mbar, the structure shows tall grains separated by true grain boundaries due to surface recrystallization. The columnar grains originating from this growth formalism extend through the coating thickness. This engenders the surface textures on the growing film; hence, the surface roughness attains a higher value than all other prepared films. The surface texture formation can be recognized by analyzing the z-axis scale of the image. Even though the surface contains vacant spaces, the microstructure formed under recrystallization has very high density [27,29,31]. The overall analysis of AFM images explores the gradual improvement in density of the thin films with reduced N₂ gas pressure.

3.3.5 Optical properties

The spectral distributions of transmission (%*T*) and reflection (%*R*) are depicted in fig. 3.9. The transmittance (*T*) of the thin films decreases with decreases in N₂ gas pressure. The rate of reduction in *T* increases for the sample sputtered at 8×10^{-3} mbar pressure. Any reduction in *T* is the consequence of the variations in reflectance (*R*) and absorptance (*A*) of the material. The incident radiation spectrum and the substrate are the same for all the studied thin films and, hence, the variations in *R* and absorptance *A* can be attributed to the variations in the material parameters of the thin films [32]. The reflectance spectra show an increasing trend with decreasing N₂ gas pressure.

The variation of the refractive index of the prepared Sn₃N₄ thin films with N₂ gas pressure is shown in fig. 3.10. The refractive index increases with decreases in N₂ gas pressure. Density is the major material parameter that influences the refractive index [33]. The improvement in the density of the fabricated thin film with decreases in N₂ gas pressure was discussed in the AFM analysis. The improved density of the

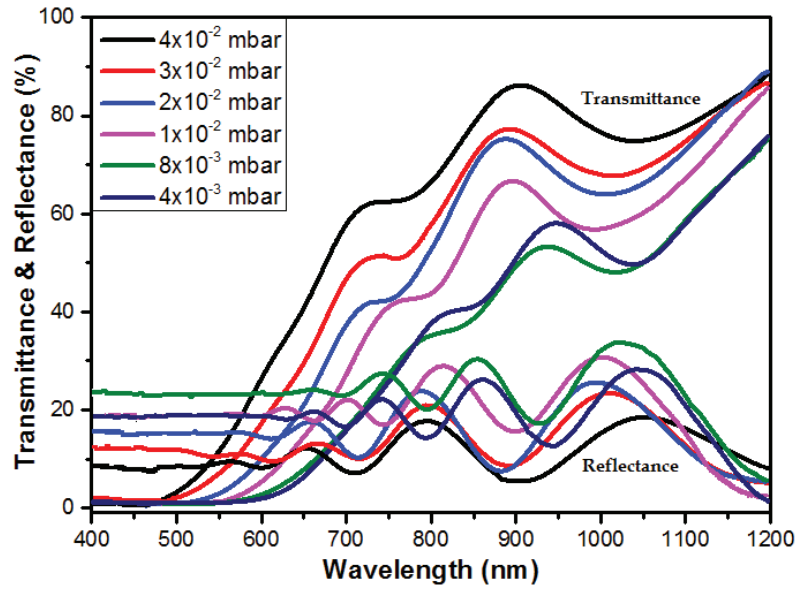


FIGURE 3.9. Transmittance and reflectance of spectra of Sn_3N_4 thin films as functions of the wavelength

thin film enhances the interaction between the electric field of the incident radiation and the molecular dipoles and leads to the increase in refractive index. According to the relation, $R = [(n_1 - n_2) / (n_1 + n_2)]^2$, the increased refractive index of the thin film material enhances its reflection capability. However, T and R of the thin film sputtered at the lowest N_2 gas pressure show opposite behavior to the others. The decrease in R can be ascribed to the surface texture formed in this thin film during the growth due to recrystallization. The texture traps the reflected energies due to its high surface roughness and the major part of the trapped energies absorbed by the thin film [34].

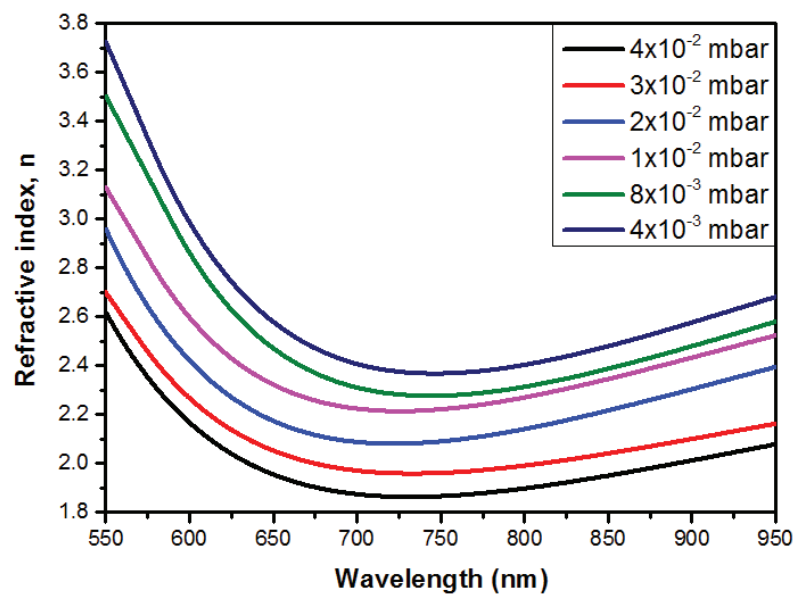


FIGURE 3.10. Refractive index of Sn_3N_4 thin films as a function of wavelength

The calculated absorption coefficients show high value for all prepared thin films and increases with decreases in N₂ gas pressure as shown in fig. 3.11. The rate of variation in absorption significantly increases for samples sputtered at 1×10⁻² mbar and lower pressures.

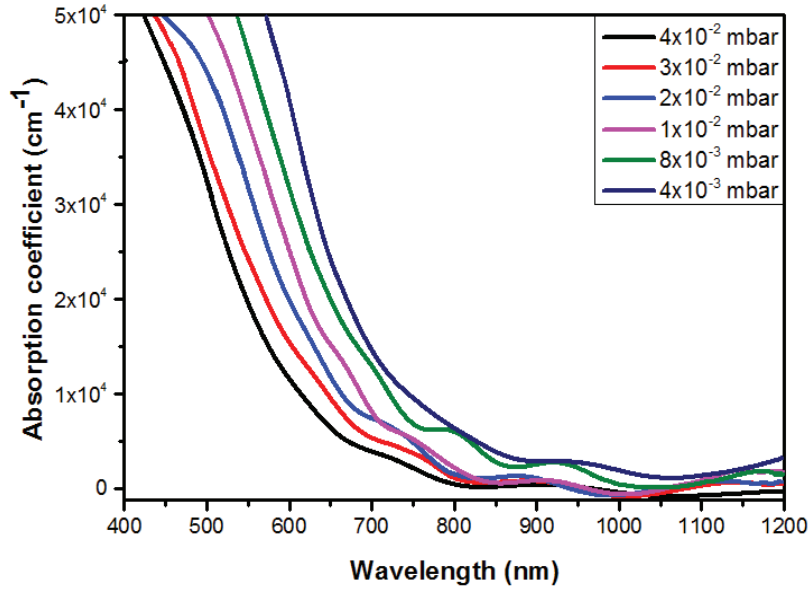


FIGURE 3.11. The variation of optical absorption coefficient of Sn₃N₄ thin films with incident wavelength

The bandgap (E_g) of the thin films is estimated by Tauc’s relationship for the direct transition semiconductors,

$$(\alpha h\nu)^2 = \alpha_0 (h\nu - E_g) \quad \dots\dots\dots (3.2)$$

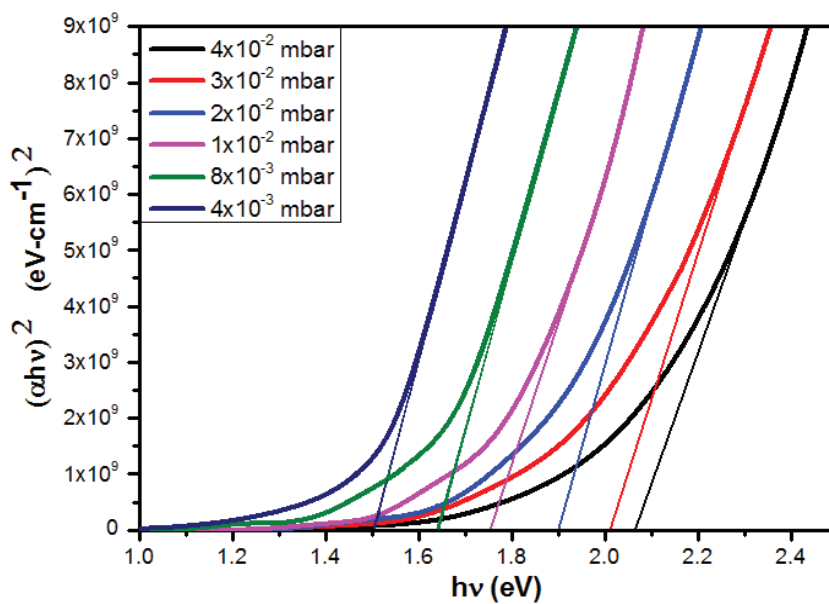


FIGURE 3.12. The variation of optical bandgap of Sn₃N₄ thin films with N₂ gas pressure

To determine the optical bandgap of the thin film, the parameter $(\alpha hv)^2$ versus photon energy (hv) is plotted in fig. 3.12. To obtain the direct band gap values, the straight line portion of the plot is extended to intercept the (hv) -axis at $(\alpha hv)^2 = 0$, showing that the bandgap decreases with decreasing N_2 gas pressure [35].

3.4 Discussion

The enhancement of power factor of a thermoelectric material can be achieved by creating a best band structure from an optimized trade-off between electrical conductivity and Seebeck coefficient. This trade-off can be optimized by controlling the carrier concentration. The simultaneous reduction in both the sputtering pressure and availability of nitrogen for reactive sputtering imparts (222) oriented crystallites instead of (311) orientation as well as new defect energy states in the thin films. Reduction in N_2 gas pressure creates a N_2 -deficient atmosphere for reactive sputtering. It creates donor-type defects such as nitrogen vacancy and tin interstitial. When considering the relationship:

$$\sigma = ne\mu \dots\dots\dots (3.3)$$

where σ is the conductivity, n is the carrier concentration, e is the charge of electron and μ is the mobility of electron, the increased carrier concentration in the sub-stoichiometric Sn_3N_4 thin films increases the conductivity. But, it shifts the E_F to a higher value and positioned more close to the lower end of the conduction band. This shifting maximizes the DOS in the Fermi window and hence decreases the mean free path of the electron and mobility. So, the enhancement in conductivity itself has a dependency on balancing between increases in carrier concentration and reduction in mobility [13,15]. However, the resultant effect improved the conductivity of the Sn_3N_4 thin films with reduced N_2 gas pressure.

When considering the relationship,

$$S = \frac{8\pi^2 k_B^2}{3eh^2} m^* T \left(\frac{\pi}{3n}\right)^{2/3} \dots\dots\dots (3.4)$$

where k_B is the Boltzmann constant, h is Planck's constant and m^* is the DOS effective

mass, the increase in Seebeck coefficient is the resultant of the variations in carrier concentration and DOS effective mass [36]. Normally, the effect of carrier concentration predominates over that of DOS effective mass in presence of increased conductivity and the Seebeck coefficient decreases. This trend of thermoelectric parameters is seen in the thin films sputtered at 2×10^{-2} mbar and higher pressures. But, a concurrent enhancement in both the Seebeck coefficient and conductivity is observed for the thin films sputtered at N_2 gas pressures lower than 2×10^{-2} mbar. To explain the phenomenon, the evolution of band structure to be explored by analyzing the optical parameters extracted from UV-Vis spectroscopy in conjunction with analyzed thermoelectric parameters.

The shallow energy levels associated with the point defects during the growth of sub-stoichiometric thin films create energy states in the bandgap near the conduction band edge. With increase in defect density, the DOS increases and forms a continuum of states like bands and gradually reduces the bandgap of the Sn_3N_4 thin film from 2.06 to 1.51 eV [37,38]. The variation of the estimated thermoelectric parameters at RT with reducing band gap is depicted in fig. 3.13. The variations of electrical conductivity and Seebeck coefficient have opposite behavior up to the bandgap of 1.9 eV and, thereafter, the parameters clearly show simultaneous improvement with the reduction in bandgap. These optical and thermoelectric parameters are listed in table 3.2.

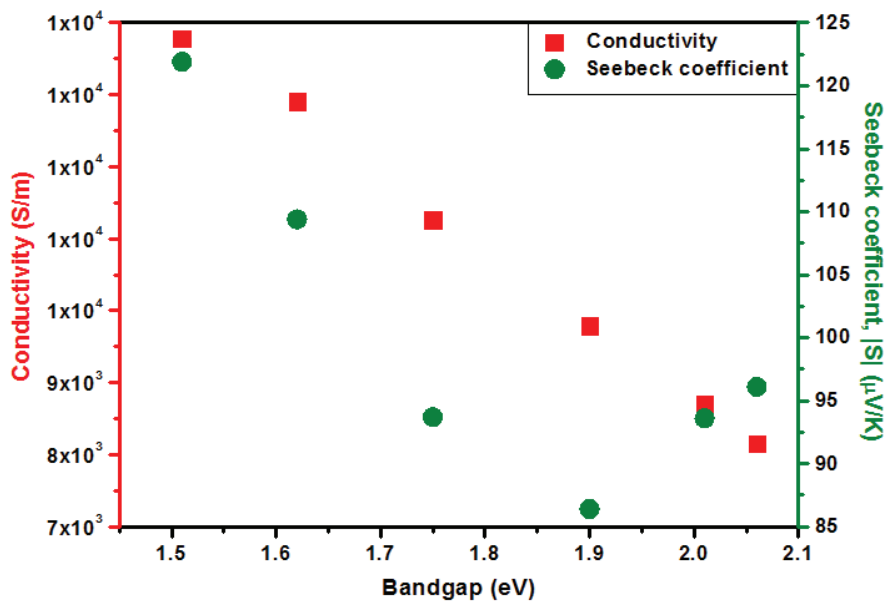


FIGURE 3.13. The variation of conductivity and Seebeck coefficient of Sn_3N_4 thin films with bandgap

According to the equation (3.4), the improvement in Seebeck coefficient in the presence of increasing carrier concentration can be attributed to the increased m^* . The m^* is derived from the Seebeck coefficient and the variations are depicted in fig. 3.14.

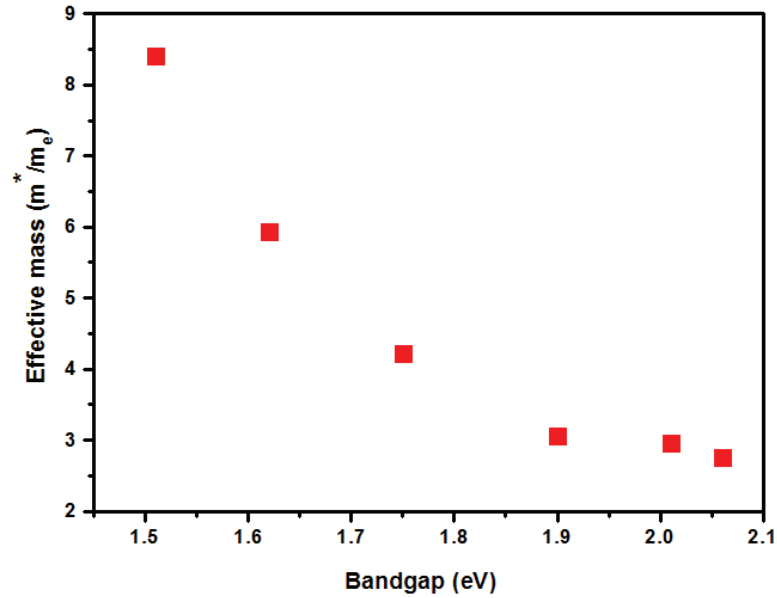


FIGURE 3.14. The variation of effective mass of Sn_3N_4 thin films with bandgap

TABLE 3.2 Optical and electronic transport parameters at RT of Sn_3N_4 thin films sputtered with different N_2 gas pressures

N_2 gas pressure (mbar)	Crystallite orientation (hkl)	Bandgap (eV)	Absorption coefficient at $\lambda = 600$ nm (/cm)	Effective mass (m^*/m_e)	Conductivity (S/m)	Seebeck coefficient ($\mu\text{V/K}$)
4×10^{-2}	(311)	2.06	1.16×10^4	2.76	8.1×10^3	-96.1
3×10^{-2}	(311)	2.01	1.55×10^4	2.95	8.7×10^3	-93.6
2×10^{-2}	(311)	1.90	2.07×10^4	3.06	9.8×10^3	-86.4
1×10^{-2}	(222)	1.75	2.53×10^4	4.23	11.3×10^3	-93.7
8×10^{-3}	(222)	1.62	3.21×10^4	5.93	12.9×10^3	-109.4
4×10^{-3}	(222)	1.51	4.22×10^4	8.40	13.8×10^3	-121.9

The following relationship,

$$m^* = (N_v)^{2/3} m_b^* \dots\dots\dots (3.5)$$

shows that valley degeneracy (N_v) or band mass (m_b^*) is responsible for the improvement in effective mass and, hence, the Seebeck coefficient [15]. When analyzing the trend of the mobility reduction, the possibility of the dependence of band mass on the Seebeck coefficient can be eliminated. Because mobility clearly follows the carrier concentration variations without any drastic reduction in N_2 gas pressures of 1×10^{-2} mbar and lower. The high effective band mass originating from band flattening produces a high Seebeck coefficient, but significantly reduces mobility [36,39]. Since the mobility does not depend on valley degeneracy, the increase in DOS effective mass is the consequence of the increased valleys in the conduction band structure [14,15,40]. The increase in conduction band valleys taking part in the transport mechanism is due to the band convergence originating from the band gap reduction and increased density of (222) oriented crystallites. In the multi-band model of transport mechanism, the transport properties are governed by the relative motion of the two conduction bands, comprising one light band and one heavy band, separated by an energy difference of ΔE , and one valence band. During the gradual reduction in bandgap with increasing (222) orientation, the heavy band with high valley degeneracy shows a sharp decline in energy and the light band with low valley degeneracy declines slightly. The conduction band convergence is schematically represented in Fig. 3.15. When the energy difference between light and heavy bands

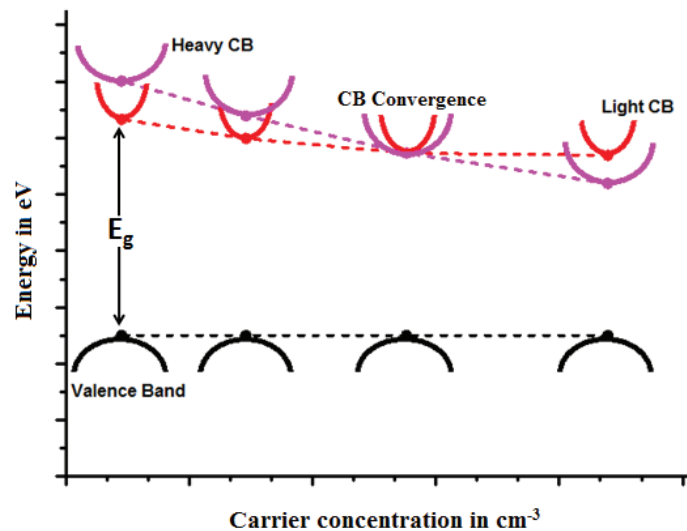


FIGURE 3.15. The schematic representation of conduction band convergence

decreases and reaches a few $k_B T$, the contribution of the heavy band to the transport process starts and progressively increases with reducing band gap and increasing orientation. This leads to an increase in the effective valley degeneracy and DOS effective mass. Hence, the Seebeck coefficient is enhanced without any adverse effect on mobility [15,36,41]. It imparts significant enhancement in thermoelectric power factor. The increase in DOS due to the increase in valley degeneracy improves the absorption coefficient in the order of $10^4/\text{cm}$ along with the reduction of band gap to an optimized value of 1.51 eV. In addition to the enhancement in thermoelectric power factor, the concurrent increase in defect density and (222) orientation originating from the reduced N_2 gas pressure provides efficient solar energy tapping capability to the Sn_3N_4 thin films.

3.5 Conclusion

The thin films of earth abundant and non-toxic tin nitride were fabricated with preferred orientation and an optimized carrier concentration for potential application as thermoelectric conversion material. The improved power factor and enhanced absorption coefficient with optimum bandgap are necessary to transform this material to a potential conversion material for thermoelectric and photovoltaics respectively. This was achieved by adopting an experimental strategy of introducing deficiency in reactive nitrogen and reduction in deposition pressure simultaneously during the growth of the thin films by taking the advantage of using nitrogen as both the sputtering and the reactive gas. This combined effect changed the orientation of the crystallites from (311) to (222) along with resulting in high defect density. These concurrent variations converged the conduction bands in accordance with bandgap reduction. This gradually increased the contribution of the second heavy conduction band in the transport process and improved the DOS by increasing valley degeneracy. These features of band evolution were explored by merging the optical analyses with thermoelectric transport parameters. The Sn_3N_4 thin film shows power factor of $390 \mu\text{W}/\text{mK}^2$ at 250°C with Seebeck coefficient of $-144 \mu\text{V}/\text{K}$ and resistivity of $53.11 \mu\Omega\text{-m}$. The modified band structure offered an optimized band gap of 1.51 eV with an increased absorption coefficient of the order of $10^4/\text{cm}$ to Sn_3N_4 thin films for efficient tapping of the entire solar spectral energy photons. Hence, this work explored the

capability of earth abundant nitrides as conversion material for renewable energy harvesting. The experimental technique used to concurrently control multiple processing parameters can be exploited to tune the microstructure and band structure of thin films for enhanced physical properties.

References

- [1] C.M. Caskey, J.A. Seabold, V. Stevanovic, M. Ma, W.A. Smith, D.S. Ginley, N.R. Neale, R.M. Richards, S. Lany, A. Zakutayev, *J. Mater. Chem. C* 3 (2015) 1389–1396.
- [2] A. Zakutayev, *J. Mater. Chem. A* 4 (2016) 6742–6754.
- [3] S.V. Nand, K. Ankur, K. Brijesh, M.B. Raj, *Solid State Sci.* 10 (2008) 569–572.
- [4] <https://materialsproject.org/materials/mp-16031/>.
- [5] International Centre for Diffraction Data, PDF Card Numbers 01-070-3184 (2010) 1-5 & 01-050-0553 (1998) 1-4.
- [6] C.M. Caskey, A. Holder, S. Shulda, S.T. Christensen, D. Diercks, P. Craig, D. Biagioni, D. Nordlund, A. Kukliansky, A. Natan, D. Prendergast, W. Sun, X. Zhang, G. Ceder, D.S. Ginley, W. Tumas, J.D. Perkins, V. Stevanovic, S. Pylypenko, S. Lany, R.M. Richards, A. Zakutayev, C.M. Caskey, A. Holder, S. Shulda, S.T. Christensen, D. Diercks, C.P. Schwartz, D. Biagioni, D. Nordlund, A. Kukliansky, A. Natan, D. Prendergast, B. Orvananos, W. Sun, X. Zhang, V. Stevanovic, S. Pylypenko, S. Lany, R.M. Richards, *J. Chem. Phys.* 144 (2016) 144201.
- [7] W.Y. Ching, P. Rulis, *Phys. Rev. B* 73 (2006) 045202.
- [8] I. Chu, A. Kozhevnikov, T.C. Schulthess, H. Cheng, *The J. Chem. Phys.* 141 (2014) 044709.
- [9] Y.C. Feng, D.E. Laughlin, and D.N. Lambeth, *J. Appl. Phys.* 76 (1994) 7311-7316.
- [10] H. Chullee, and J.Y. Lee, *J. Mater. Sci. Mater. Electron.* 5 (1994) 221-225.
- [11] U.C. Oh and J.H. Je, *J. Appl. Phys.* 74 (1993) 1692-1696.
- [12] M. Jonson, G.D. Mahan, *Phys. Rev. B* 21 (1980) 4223–4229.
- [13] J. Wei, H.J. Liu, L. Cheng, J. Zhang, J.H. Liang, P.H. Jiang, D.D. Fan, J. Shi, *AIP Adv.* 5 (2015) 107230.
- [14] J. He, T.M. Tritt, *Science* 357 (2017) 1–10.
- [15] Y. Pei, H. Wang, G.J. Snyder, *Adv. Mater.* 24 (2012) 6125–6135.
- [16] G. Shugar and J. Ballinger, *Chemical technicians' ready reference handbook*,

- Tata Mc-Graw Hill, U.S.A. (1996).
- [17] B.D. Cullity, Elements of X-ray diffraction, Addison-Wesley, U.S.A. (1956).
- [18] J.T. Wang, X.L. Shi, W.W. Liu, X.H. Zhong, J.N. Wang, L. Pyrah, K.D. Sanderson, P.M. Ramsey, M. Hirata, K. Tsurii, Sci. Rep. 4 (2014) 3679.
- [19] M. Kumar, A. Kumar, A.C. Abhyankar, ACS Appl. Mater. Interfaces 7 (2015) 3571–3580.
- [20] E. Alfonso, J. Olaya, and G. Cubillos, Crystallization-Science and technology: Thin film growth through sputtering technique and its applications, IntechOpen (2011) 397-432.
- [21] H.H. Yang, J.H. Je, and K.B. Lee, J. Mater. Sci. Lett. 14 (1995) 1635-1637.
- [22] R. Carel, C.V. Thompson, and HJ. Frost, Acta Mater. 44 (1996) 2479-2494.
- [23] S. Chen, P. Narang, H.A. Atwater, L.W. Wang, Adv. Mater. 26 (2014) 311–315.
- [24] A.N. Fioretti, A. Zakutayev, H. Moutinho, C. Melamed, J.D. Perkins, A.G. Norman, M. Al-jassim, S. Toberer, A.C. Tamboli, J. Mater. Chem. C 3 (2015) 11017–11028.
- [25] H. Julian Goldsmid, Introduction to thermoelectricity, Springer, Germany (2010).
- [26] C. Cao, H.F. Chan, J. Zang, K.W. Leong, X. Zhao, Adv. Mater. 26 (2014) 1763–1770.
- [27] M. Pelliccione, T. Karabacak, C. Gaire, G. Wang, T. Lu, Phys. Rev. B 74 (2006) 1–10..
- [28] J.A. Thornton, J. Vac. Sci. Tech. 11 (1974) 666–670.
- [29] P.M. Martin, Handbook of deposition technologies for films and coatings, Elsevier, U.K. (2009).
- [30] R. Messier, A.P. Giri, R.A. Roy, J. Vac. Sci. Tech. A 2 (1984) 500–503.
- [31] P.B. Barna, M. Adamik, Thin Solid Films 317 (1998) 27–33.
- [32] N.J. Harrick, Appl. Opt. 10 (1971) 2344–2349.
- [33] A. Sangwal, W. Kucharczyk, J. Phys. D: Appl. Phys. 20 (1987) 522–525.
- [34] B. Shi, B. Liu, J. Luo, Y. Li, C. Zheng, X. Yao, L. Fan, J. Liang, Y. Ding, C. Wei, D. Zhang, Y. Zhao, X. Zhang, Sol. Energy Mater. Sol. Cells 168 (2017) 214–220.
- [35] J. Tauc, R. Grogrovici, A. Vancu, Phys. Stat. Soli. 15 (1966) 627–637.
- [36] G. Tan, L. Zhao, M.G. Kanatzidis, Chem. Rev. 116 (2016) 12123–12149.
- [37] C.A. Bates, K.W.H. Stevens, Rep. Prog. Phys. 49 (1986) 783–823.
- [38] S. Nayak, M. Baral, M. Gupta, J. Singh, M. Garbrecht, T. Ganguli, S.M. Shivaprasad, B. Saha, Phys. Rev. B 99 (2019) 161117.
- [39] J. Zhai, T. Wang, H. Wang, W. Su, X. Wang, T. Chen, C. Wang, Chin. Phys. B 27 (2018) 1–13.

- [40] H. Kim, N.A. Heinz, Z.M. Gibbs, Y. Tang, S.D. Kang, G.J. Snyder, *Mater. Today* 20 (2017) 452–459.
- [41] W. Liu, X. Tan, K. Yin, H. Liu, X. Tang, J. Shi, Q. Zhang, C. Uher, *Phys. Rev. Lett.* 108 (2012) 1–5.

EFFECT OF POINT DEFECT INDUCED RESONANT LEVELS ON THERMOELECTRIC PROPERTIES OF ZINC TIN NITRIDE THIN FILMS

Contents

-
- 4.1 Introduction
 - 4.2 Fabrication of thin films
 - 4.3 Results
 - 4.4 Discussion
 - 4.5 Conclusion
-

This chapter deals with the formation of resonant energy states in the ZnSnN₂ thin films by intrinsic point defects instead of conventional resonant impurity doping to enhance the thermoelectric power factor. It also discusses the method to ensure the presence of point defect induced resonant energy levels in the conduction band of a material by electronic spectrum.

4.1 Introduction

The evolution of an earth abundant binary nitride thin film as efficient thermoelectric and photovoltaic conversion material was reported in the previous work. Here a ternary nitride having structural and physical properties resemble to that of chalcopyrites have been considered for the investigation of thermoelectric properties. Chalcopyrite is a copper iron sulfide (CuFeS₂) mineral that crystallizes in the tetragonal system. Chalcopyrite type compounds have considerable attraction because of its structural resemblance to functional semiconductors with diamond and zinc blende structures. It provides an additional aspect of ordering/disordering of the cation sublattice due to the presence of multiple cations. The I-III-VI and II-IV-V₂ chalcopyrite compounds can be derived from II-VI and III-V zinc blende compounds respectively. This was first predicted by Goodman et al. in 1950s and later by 1957, seven compounds were synthesized and characterized by them [1,2]. ZnSnN₂ is a heterovalent ternary compound closely related to ternary chalcopyrites. It is a part of II-IV-V₂ compounds having β -NaFeO₂ structure derived from III-N wurtzites and having similar optical and electronic properties. Hence, ZnSnN₂ is a promising material in the field of green energy generation. It shows favorable electronic characteristics for thermoelectric energy generation with bandgap spans over a wide energy range. All constituent elements in ZnSnN₂ are non-toxic, low cost and earth abundant with good recycling. Also the ordering/disordering of the cation sublattice depended physical property variations can be exploited to transform it as a renewable energy conversion material [3].

The ZnSnN₂ semiconductor compound crystallizes in two different structures with respect to the ordering/disordering of the cation sublattice. The ordered phase has orthorhombic structure with Pna2₁ or Pmc2₁ space group and wurtzite or monoclinic structure for disordered phases. The variations in crystal structure, space group and bandgap of ZnSnN₂ with order-disorder transformations are still debatable in literatures. Here, the most stable orthorhombic Pna2₁ structure was considered for ZnSnN₂ thin films having the theoretically calculated lattice parameters of a=5.84 Å, b=6.72 Å and c=5.45 Å [4]. The crystal structure of stable ZnSnN₂ compound is shown in fig. 4.1 [5]. There are number of theoretical and experimental reports in the literature exploring the variation of crystal and electronic structures with the

disordering of cation sublattice. It shows degenerate semiconductor behavior originates from the low formation energy of native donor defects. Hence, the optical bandgap always exhibits Burstein-Moss shift. The tuning of the disorder provides spanning of the direct bandgap from 1-2.4 eV. The carrier concentration of the disordered thin films is the order of 10^{20} cm^{-3} [6].

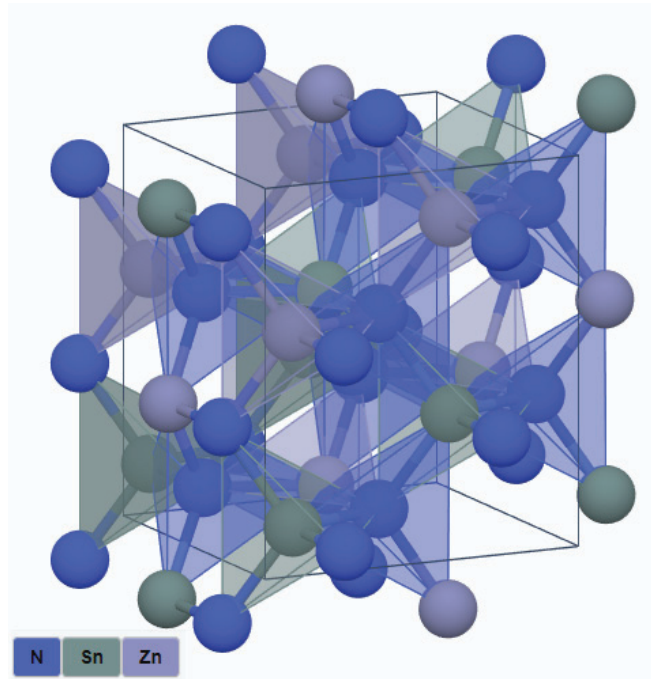


FIGURE 4.1. Crystal structure of ZnSnN₂ compound

The researchers have been adopting various techniques to tune the effective mass of charge carriers such as band convergence, band flattening, carrier energy filtering and resonant level scattering for an enhanced power factor [7]. The application of each method has unique advantages on different scenarios. In chapter-3, we have seen the efficient application of conduction band convergence technique to enhance the thermoelectric power factor of a binary nitride thin film. The capability of the technique to decouple the interdependence of Seebeck coefficient and conductivity and the electronic band structure of tin nitride compound greatly motivated us to utilize the conduction band convergence technique. Among the mentioned advanced strategies to improve power factor, resonant level scattering technique can influence the Seebeck coefficient and conductivity independently in two different ways. Hence, it brings significant improvement in thermoelectric power factor of materials [7,8]. The conduction band with resonant energy levels of an n-type material is shown fig.

4.2 as E-k diagram [8,9]. In conventional n-type doping, the energy states of the dopant atoms lie below the conduction band edge and in the bandgap of the semiconductor. In contrast, the resonant impurity would have an energy state known as impurity state (IS) within in the conduction band having energy of E_{res} . This energy level resonates with the free extended state (ES) having the same energy and build up two new energy states of slightly different energies in accordance with the Pauli exclusion principle. These virtual bound states having the same energies as the states of continuum in the conduction band and so on. Consequently, these virtual bound states acquire a certain width and known as resonant energy states (RS) [8–10]. The resonant energy levels are often created by incorporating resonant impurities in accordance with the host material. In semiconductors, s and p states impurities are more efficient than the other orbital states. The dopants must have the electronics configuration very close to that of the host material to create an energy state in the vicinity of the Fermi level. Normally the elements from the adjacent columns of the host material in the periodic table are preferable [9,11,12].

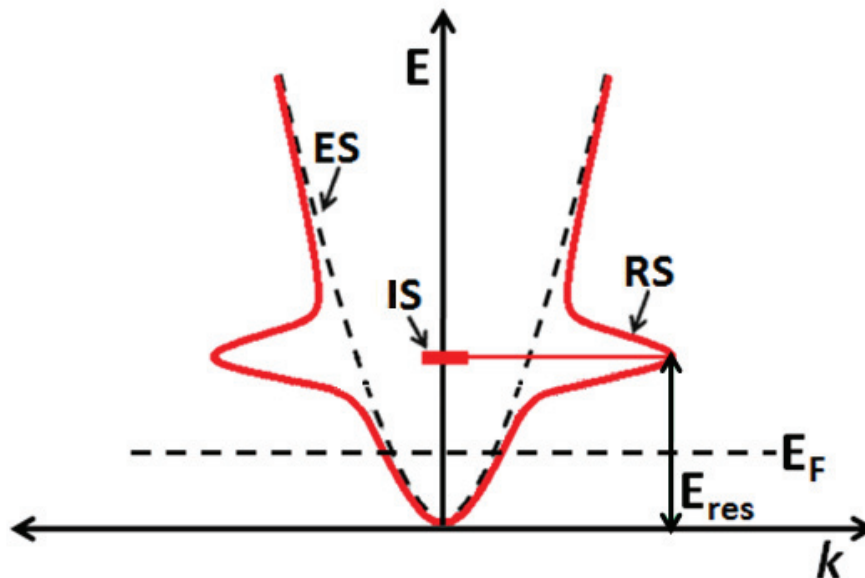


FIGURE 4.2. The resonant energy levels in a conduction band of an n-type material

The defect chemistry of ZnSnN₂ is greatly supporting the formation of resonant levels. Chen et al. calculated the formation energies of point defects in ZnSnN₂. The donor defects have significantly lower formation energies than acceptor defects. They also reported the energy states formed in the band structure due to these point defects [13,14]. These energy states span from 0.37 eV below to few hundreds

of meV above the conduction band minimum (CBM), hence the resonant energy states can be developed in ZnSnN₂ using point defects. The proper aligning of the Fermi level and defect energy levels to create the efficient resonant states is possible by the precise tuning of each defect or their combinations. The creation of resonant states in the conduction band by intrinsic defect strategy has some advantages over that by resonant elemental doping. It eliminates the tedious process of determining the suitable resonant impurity element for host material and the requirement of dual doping [15–17]. It permits precise and more control over resonant energy states by proper tuning of the various material processing parameters. The defect formation is greatly influenced by the chemical potential of the each element in the ZnSnN₂ and chemical potential can be varied using the reactive gas partial pressure, target composition and substrate temperature [3,4,13,18].

This chapter deals with the formation of resonant energy states in the ZnSnN₂ thin films by intrinsic defects itself to enhance the thermoelectric power factor. This is the first attempt ever in resonant level scheme, formation of resonant energy states in the conduction band by intrinsic point defects instead of resonant impurity doping. The careful control of the multiple point defects will concurrently position the Fermi level and resonant states independently with respect to CBM. This will supplement to achieve maximum benefit from resonant levels and, hence expecting significant enhancement in thermoelectric power factor.

4.2 Fabrication of ZnSnN₂ thin films

The ZnSnN₂ thin films were deposited by reactive radio-frequency magnetron sputtering. The 99.99% pure Zn_{0.6}Sn_{0.4} target was sputtered using nitrogen (N₂) plasma and deposited on glass substrate. In order to develop resonant energy states in the conduction band of ZnSnN₂, formation of nitrogen vacancies are essential. Reduction of nitrogen pressure in the chamber decreases the concentration of nitrogen and working pressure of reactive sputtering. It greatly supplements the annihilation of Sn_{Zn} antisite (Sn substituting Zn) defects instead of supporting the formation of nitrogen vacancy (V_N) defects. The simultaneous reduction of N₂ and working pressures provide enough energy to excess Zn atoms to occupy its lowest energy positions and reducing the Sn_{Zn} antisite defects and prevent the formation of V_N defect

[13,14,19]. Hence, during the reduction of nitrogen pressure, the working pressure of sputtering held constant at 3×10^{-2} mbar by purging Ar gas. The partial pressure of nitrogen in the chamber was set to different values in the range of 3×10^{-2} to 1×10^{-2} mbar and then purging Ar to maintain the working pressure at 3×10^{-2} mbar. The influence of plasma composition, power and substrate temperature on various physical properties was investigated to optimize the deposition parameters of ZnSnN₂ thin films for the specific thermoelectric studies. The optimized sputtering parameters are listed in table 4.1.

TABLE 4.1. The optimized deposition parameters for ZnSnN₂ reactive sputtering

Parameter	Specification
Fabrication Technique	Reactive RF magnetron sputtering
Target	99.99% pure Zn _{0.6} Sn _{0.4}
Substrate	Glass with 99.99% pure and 10x10x1mm size
Plasma	99.999% pure Nitrogen and Argon
Target-Substrate Distance	8 cm
Sputtering Power	150 W
Substrate Temperature	300°C
Ultimate Vacuum	6×10^{-6} mbar
Working Pressure	3×10^{-2} mbar
Nitrogen Partial Pressure	1×10^{-2} - 3×10^{-2} mbar
Film Thickness	~600 nm

4.3 Results

4.3.1 Phase and crystallographic features

In order to create nitrogen vacancies in the thin films, the nitrogen pressure of sputtering was reduced to different values in the range of 3×10^{-2} to 1×10^{-2} mbar. Fig. 4.3 shows the XRD patterns of the reactively sputtered ZnSnN₂ thin films at different nitrogen partial pressures. According to the literature data, ZnSnN₂ can grow with various crystal structures: ordered phase has orthorhombic structure with Pna2₁ or

Pmc2₁ space group and wurtzite or monoclinic structure for disordered phases [3,20]. The variations in crystal structure, space group and bandgap of ZnSnN₂ with order-disorder transformations are still debatable in literatures. Since the XRD of ZnSnN₂ deposited in this study only exhibit one intense reflection due to strong preferred orientation, the most stable orthorhombic Pna2₁ structure was assigned to the prepared phase [21]. The X-ray reflections located at Bragg angles $\sim 32.5^\circ$ and $\sim 68.5^\circ$ were assigned to the (002) and (004) planes. This indicating that the sputtered ZnSnN₂ thin films exhibit strong preferred orientation along [001] direction. The crystallinity of the thin films is increasing slightly with decreasing nitrogen pressure. The argon supplied to the plasma for compensating the reduction in working pressure due to the decrease in nitrogen pressure delivers more momentum to the target atoms. Hence, the energy of the adsorbed Zn-Sn atoms is increased and results in improved crystallinity [22].

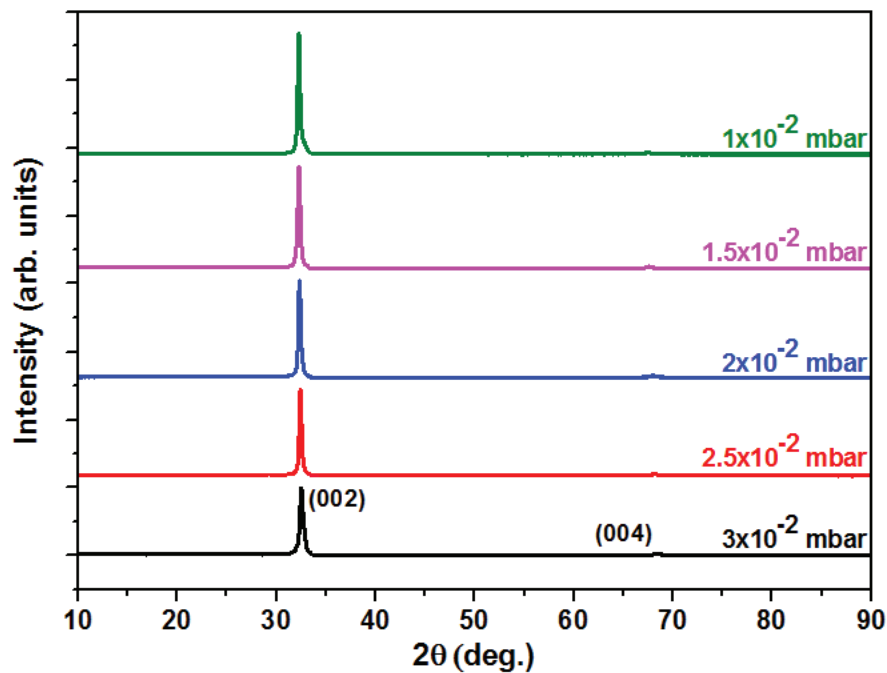


FIGURE 4.3. XRD of of ZnSnN₂ thin films sputtered with different nitrogen partial pressure

4.3.2 Thickness

The thickness of the sputtered thin films was confirmed by AFM [23]. The thickness is estimated from the depth parameters of the step profile created by partially masking the substrate as shown in fig. 4.4. The thickness of all thin films sputtered at various nitrogen partial pressures is ~ 600 nm.

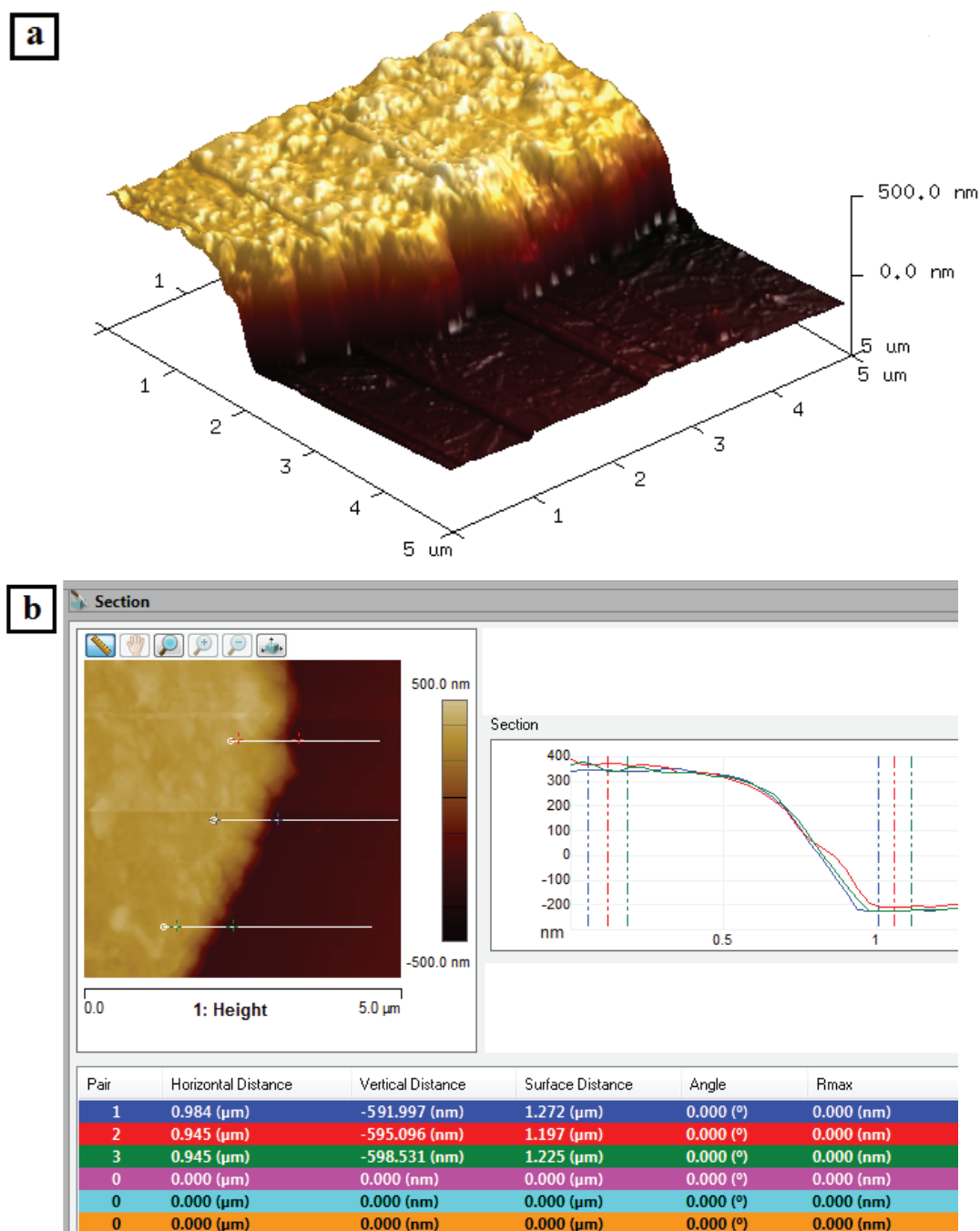


FIGURE 4.4. (a) Surface topography and (b) step parameters of partially masked ZnSnN₂ thin film

4.3.3 Surface features

The morphology and surface roughness of the ZnSnN₂ thin films deposited at various N₂ partial pressures were analysed by AFM. The 3D surface topography with the value of surface roughness is shown in fig. 4.5. The scans were performed on an area of 1 μm × 1 μm with scanning rate of 1 Hz and 256×256 pixel resolution.

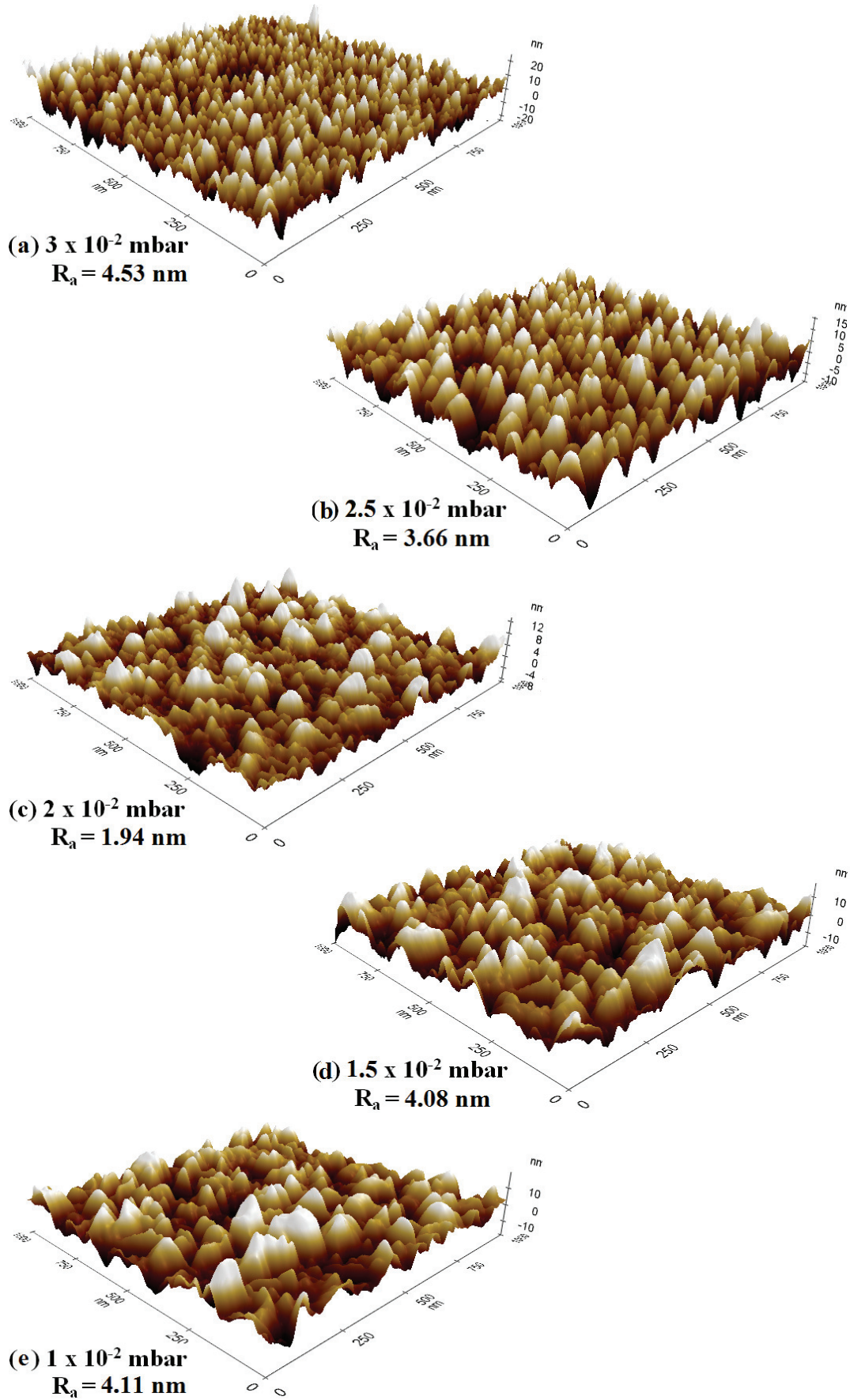


FIGURE 4.5. AFM surface profile with average surface roughness of ZnSnN₂ thin films

It shows the variations in surface profile with the N₂ partial pressure. The surface particles exhibit a spherical morphology and the size is increased with decrease in N₂ partial pressure for all the thin films. This can be attributed to the increased surface mobility of the adatoms obtained from the more momentum delivery of excess argon concentration in the plasma. During the reduction in N₂ partial pressure, the excess argon is supplied to the plasma to maintain a constant working pressure. Since these argon atoms can deliver more momentum to the target atoms than the nitrogen atoms, the surface mobility of the adatoms increase with decrease in N₂ partial pressure [22,24]. During the growth of crystallites with reduced N₂ partial pressure, ZnSnN₂ thin films exhibit coalescence of the spherical particles as shown fig. 4.5 (c). The growth formalism originated as a result of increasing surface mobility and particle size and the coalescence of crystallites determine the surface roughness of the thin films [24,25]. All prepared thin films show smooth surfaces and the highest surface roughness is 4.53 nm.

4.3.4 Electronic transport properties

The variation of the carrier concentration (*n*) of the thin films with reduction in nitrogen partial pressure was measured at room temperature by Van der Pauw configuration. The carrier concentration is increased during the reduction of N₂

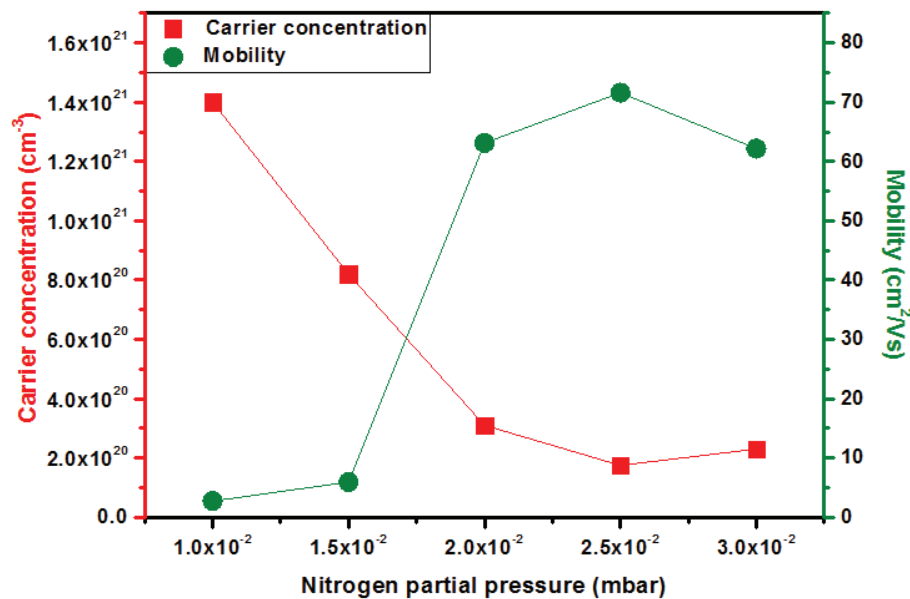
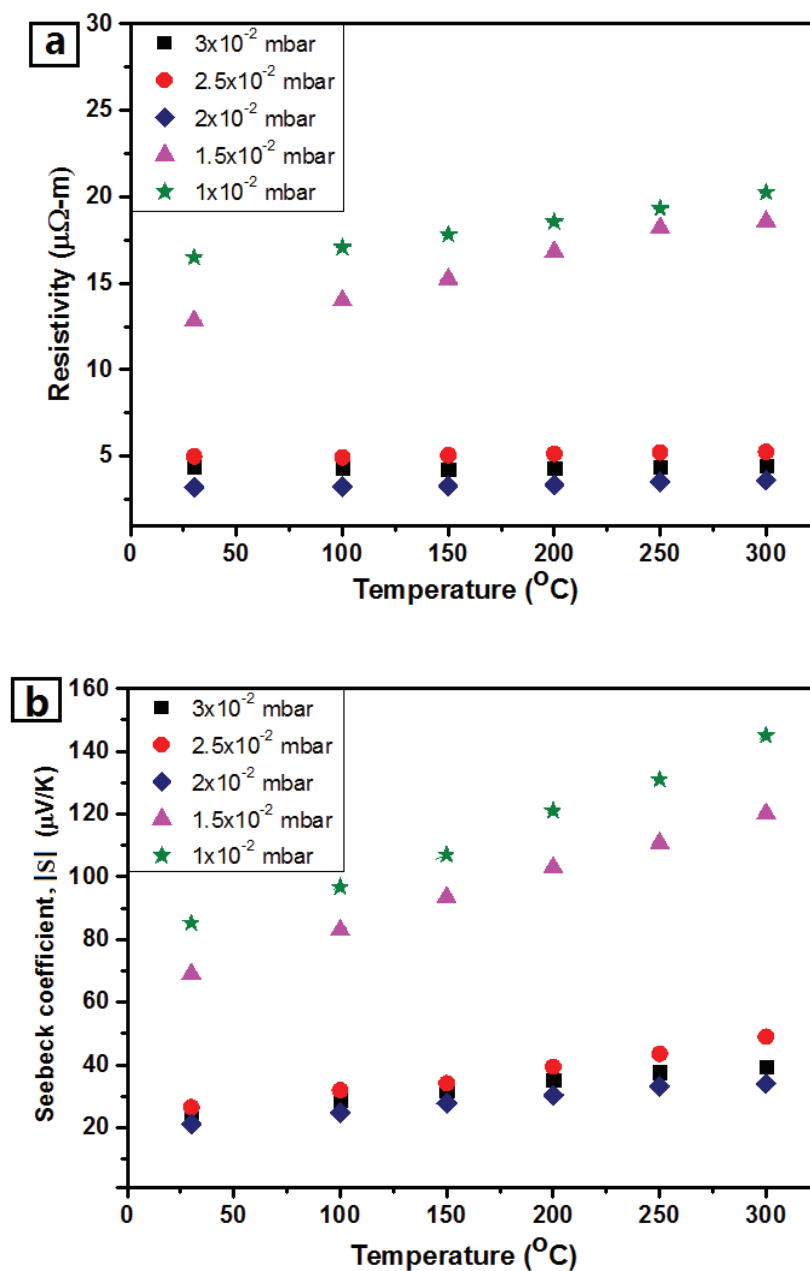


FIGURE 4.6. Variation of carrier concentration and mobility of ZnSnN₂ thin films with N₂ gas pressure

pressure except at the initial reduction from 3×10^{-2} to 2.5×10^{-2} mbar as shown in fig. 4.6. During the reduction in nitrogen partial pressure, the flow of nitrogen in to the plasma is restricted. It decreases the availability of reactive nitrogen for sputtered Zn-Sn atoms and resulting in the formation of nitrogen vacancies [4,14,20].

4.3.5 Thermoelectric properties

The influence of nitrogen partial pressure on resistivity and Seebeck coefficient is shown in fig. 4.7. At higher nitrogen pressures, the resistivity is very low and it increases significantly for the films sputtered at 1.5×10^{-2} mbar. The films



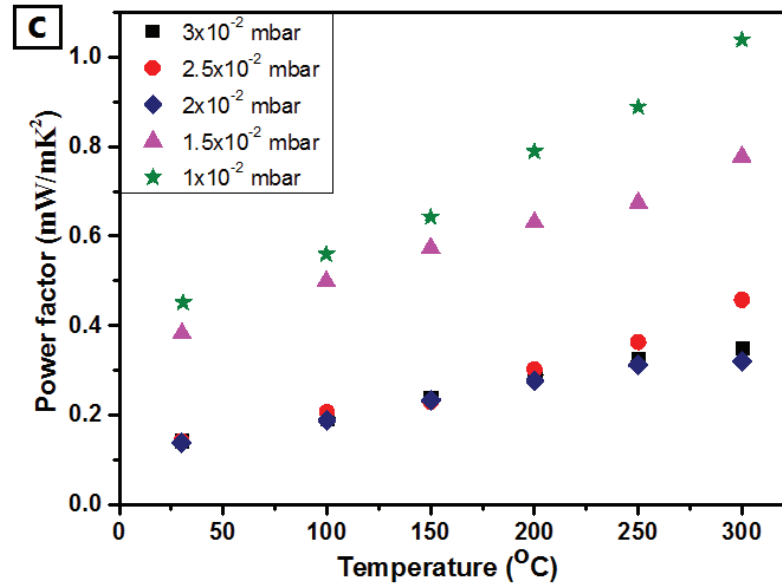


FIGURE 4.7. The variation of temperature dependant (a) resistivity, (b) Seebeck coefficient and (c) power factor of ZnSnN₂ thin films with nitrogen partial pressure

sputtered at lower pressures exhibit high resistivity. The variation of Seebeck coefficient with resistivity is normal and it depends on the variation of Fermi energy with carrier concentration [26]. The variation of power factor clearly reflects the resultant of variations in resistivity and Seebeck coefficient. The highest power factor is achieved for the ZnSnN₂ thin film fabricated at lowest nitrogen partial pressure. The detailed analysis of the variations in charge transport parameters and point defects with N₂ partial pressure is required to investigate the variations of thermoelectric properties.

4.3.6 Optical properties

The transmission (%T) and reflection (%R) spectra of investigated thin films of ZnSnN₂ thin films are shown in fig. 4.8. The interference fringes in the spectra are the indication of the uniform and homogeneous nature of film surfaces. As N₂ partial pressure decreases, the transmittance becomes relatively higher and reflectance becomes relatively lower. The increase in transmittance can be attributed to the variations in absorption coefficient and reflectance of the thin films. These factors have great dependence on the microstructure and the composition of the thin films [27]. During the reduction in N₂ partial pressure, the growth formalism originated due to the increased adatom mobility and the increased metallic composition due to

nitrogen deficient plasma result in microstructural and compositional variations respectively. The bandgap of the thin films is estimated by Tauc's relationship for the direct transition semiconductors and shown in fig. 4.9 (a) [28,29].

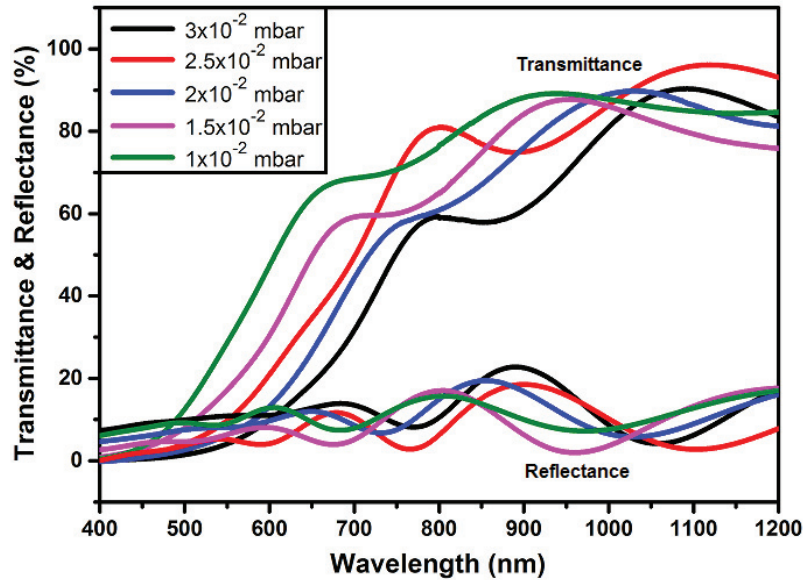


FIGURE. 4.8. Transmittance and reflectance spectra as functions of wavelength of ZnSnN₂ thin films sputtered at different N₂ partial pressure

4.4 Discussion

The significant enhancement in thermoelectric power factor of ZnSnN₂ can be achieved by developing resonant energy states in the conduction band. The careful control over nitrogen vacancies (N_V) and Sn_{Zn} antisite defects (Sn_{Zn}) eliminates the requirement of external resonant impurity elements and dual doping. The precise tuning of the point defects of ZnSnN₂ thin films create resonant energy states in the conduction band and results in enhanced power factor. The variation in N₂ partial pressure during deposition creates point defects in thin films. At the initial reduction of pressure from 3×10^{-2} to 2.5×10^{-2} mbar, the slight increase in resistivity is due to the decrease in carrier concentration. During this reduction of nitrogen pressure, the deficiency of nitrogen is not sufficient to create vacancies in presence of the excess Zn atoms. These Zn atoms acquire enough energy from the momentum supplied by the argon atoms and the annihilation of Sn_{Zn} defects predominates over the N_V defects [4,30]. Hence, initially the carrier concentration decreases and the resistivity increases. The corresponding change in Fermi energy increases the Seebeck coefficient. The slight increase in mobility as shown fig. 4.6 suggests that it is mainly influenced by

carrier concentration and improved crystallinity. Thereafter, due to more deficiency of the nitrogen with decreasing pressure, the nitrogen vacancies predominate over excess Zn results in increased carrier concentration. The decrease in resistivity, mobility and Seebeck coefficient in presence of enhanced carrier concentration is normal.

Further reduction in nitrogen pressure significantly increases resistivity in presence of increased carrier concentration and crystallinity. Also, it shows large increase in Seebeck coefficient. These parameter variations point out the formation of resonant energy states in the conduction band [11,10,31]. The deficiency of nitrogen creates N_V defects that have low formation energy in ZnSnN₂ thin films. The corresponding energy states formed in few meV above the conduction band minimum (CBM), hence the resonant energy states is developed in ZnSnN₂ [13,14,32]. These resonant levels induce a peak in the density of states near the resonant energy and enhance the effective mass. Also, the resonant energy states both conduct and diffuse charge carriers which are extremely sensitive to their energies [9,7,33]. The impact of these resonant energy states on the thermoelectric transport parameters can be elucidated by an approximate formula [10,7,34],

$$S = \frac{\pi^2 k_B^2 T}{3 e} \left[\frac{g(E)}{n(E)} + \frac{1}{\mu(E)} \frac{d\mu(E)}{dE} \right] \dots\dots\dots (4.1)$$

where $g(E)$ is the density of states, $n(E)$ is the number of states and $\mu(E)$ is the mobility. This approximate equation for degenerate semiconductors with single band conduction was derived from Bethe-Sommerfeld expansion of the Mott relation. It shows that, the large density of states and the strong dependence of mobility on energy through energy dependent relaxation time improve the Seebeck coefficient. Due to the presence of energy barriers induced by point defects, the electrons lower than a critical value is confined within the potential wells. These electrons are not participating to charge and energy transport. Since the Seebeck coefficient is determined by the average total energy of charge carriers, the carrier filtering enhances the Seebeck coefficient. Hence, the resonant energy scheme influences the thermoelectric properties in two ways. Both the peak in the density of states and the selective scattering of charge carriers enhances the Seebeck coefficient of the ZnSnN₂ thin films.

The sharp dip in mobility as shown in fig. 4.6 confirms the proper formation of resonant states in the conduction band of ZnSnN₂. The triggered peak in the DOS when the central energy of the resonant states is properly aligned with the Fermi energy enhances the effective mass of the electrons and decreases mobility [15,35]. The effect of mobility reduction predominates over that of increased carrier concentration results in increased resistivity. The Seebeck coefficient shows a significant enhancement due to the presence of the peak in DOS. The nitrogen vacancies and carrier concentration increase with reducing nitrogen pressure and the corresponding energy states more strongly resonates with the existing states and so on. The decrease in variation of Seebeck coefficient of thin film sputtered at lowest pressure of 1×10^{-2} mbar points the reduction of effective resonant levels due to the deviation of optimum position of resonant levels from the Fermi level. The maximum benefit from the resonant energy states are obtained when the position and width of the resonant levels should be in its optimum [31,9,36]. In order to obtain the maximum power factor from an optimized carrier concentration, the Fermi level E_F must be situated at a correct position with respect to the band edge. At the same time, **TABLE 4.2.** Optical and electronic transport parameters of ZnSnN₂ thin films sputtered at various nitrogen partial pressures the deviation of the Fermi level from the central energy of the resonant levels declines

<i>Nitrogen partial pressure</i>	<i>Carrier concentration</i>	<i>Mobility</i>	<i>Bandgap</i>	<i>Resistivity</i>	<i>Seebeck coefficient</i>	<i>Power factor</i>
(mbar)	(/cm ³)	(cm ² /V s)	(eV)	(μΩ m)	(μV/K)	(μW/m K ²)
3×10^{-2}	2.32×10^{20}	62.18	1.81	4.37	-25.1	140.4
2.5×10^{-2}	1.75×10^{20}	71.61	1.94	4.98	-26.5	142.6
2×10^{-2}	3.11×10^{20}	63.17	1.87	3.19	-21.2	131.7
1.5×10^{-2}	8.24×10^{20}	5.93	2.07	12.83	-69.7	370.0
1×10^{-2}	14.15×10^{20}	2.73	2.26	16.49	-85.9	451.1

the efficacy of the resonant level scheme. Hence the central energy of resonant levels itself must be located at the optimum position with respect to the band edge of the host material. In addition to the mentioned conditions, Mahan and Sofo explored the consequences of the broadening of the density of states peak [10,36]. The enhancement of the efficiency degraded with the widening of the density of states peak. The variations of resistivity and Seebeck coefficient are clearly reflected in the power factor of the thin films. The power factor of thin films deposited at lower pressures is large due to the significant enhancement in Seebeck coefficient. The estimated thermoelectric parameters are listed in table 4.2.

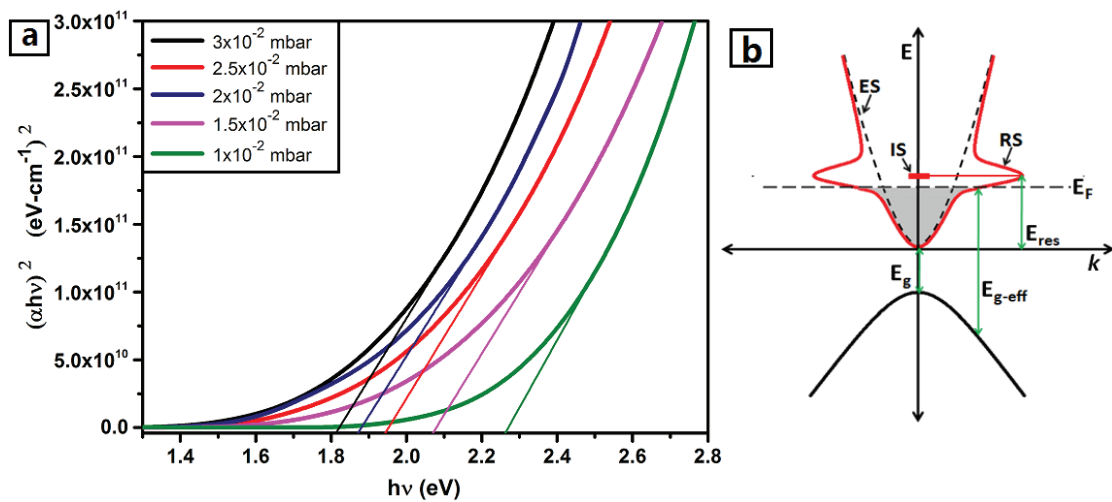


FIGURE 4.9. (a) The variation of bandgap with nitrogen partial pressure and (b) the Burstein-Moss shift in the optical bandgap of ZnSnN₂ thin films having resonant energy levels

The optical bandgap analysis also greatly validates the enhancement of thermoelectric properties by resonant levels stem from intrinsic point defects in ZnSnN₂ thin films. The variations in bandgap by the influence of decrease in nitrogen partial pressure are shown in fig. 4.9 (a). The variations of optical bandgap at higher pressures follow the normal defect mechanism. The thin films sputtered at lower pressures show rapid increase in band gap. The increase in bandgap with carrier concentration can be attributed to the Burstein-Moss shift [37,38]. It suggests that when free electrons fill the bottom of the conduction band, the excitation of electrons to these populated states is obstructed causing an increase in the apparent bandgap (E_g) as shown in fig. 4.9 (b). Hence, the effective optical bandgap (E_{g-eff}) of the thin film is increased with carrier concentration. The determined optical bandgaps are

listed in Table 4.2. Also, the Fermi level (E_F) shifts into the conduction band as a consequence of Burstein-Moss shift [4,30,39,40]. The Fermi level within the conduction band is a necessary criterion for the improvement of Seebeck coefficient by resonant levels. The enhancement of optical bandgap with carrier concentration of the ZnSnN₂ thin film sputtered at 1.5×10^{-2} and 1×10^{-2} mbar confirms the presence of Fermi level within the conduction band.

4.5 Conclusion

The thin films of earth abundant ZnSnN₂ were fabricated by reactive radio frequency magnetron sputtering. In order to enhance the thermoelectric conversion capability, the resonant energy states were developed by controlling the intrinsic point defect instead of resonant impurity doping. The careful control of the multiple point defects concurrently positioned the Fermi level and resonant energy states independently with respect to CBM. The large density of states and the strong dependence of mobility on energy through energy dependent relaxation time stem from the presence of resonant states improved the Seebeck coefficient. The ZnSnN₂ thin film exhibited the power factor of 1 mW/m K^2 at 300°C with Seebeck coefficient of $-145 \mu\text{V/K}$ and resistivity of $20 \mu\Omega \text{ m}$. The power factor is more than doubled as compared to the thin films without resonant energy states. Hence, this work explored a way of developing resonant energy states in the conduction band of a thin film by intrinsic point defects, a simple and reliable method than conventional resonant impurity doping. The defect chemistry of ZnSnN₂ opens a new window into resonant level induced thermoelectrics. This methodology can also be exploited to tune the various physical parameters of thin films by point defect induced resonant levels.

References

- [1] C.H.L. Goodman, R.W. Douglas, *Physica XX*, No. 11, Amsterdam Conference, Semiconductors (1954) 1107–1109.
- [2] C.H.L. Goodman, *Nature* 179 (1957) 828-829.
- [3] R.A. Makin, N. Senabulya, J. Mathis, N. Feldberg, P. Miska, R. Clarke, S.M. Durbin, R.A. Makin, *J. Vac. Sci. Tech. B*, 35 (2017) 02B116.

- [4] K. Chinnakutti, P. Vengatesh, T.S. Shyju, *J. Alloys Compd.* 772 (2018) 348-358.
- [5] <https://materialsproject.org/materials/mp-1029469/>.
- [6] A.D. Martinez, A.N. Fioretti, E.S. Toberer, A.C. Tamboli, *J. Mater. Chem. A*, 5 (2017) 11418–11435.
- [7] J. He, T.M. Tritt, *Science* 357 (2017) 1-10.
- [8] B. Wiendlocha, *Phys. Rev. B* 97 (2018) 205203.
- [9] J. Zhai, T. Wang, H. Wang, W. Su. X. Wang, T. Chen, C. Wang, *Chin. Phys. B* 27 (2018) 047306.
- [10] J.P. Heremans, B. Wiendlocha, A.M. Chamoire, *Energy Environ. Sci.* 5 (2012) 5510–5530.
- [11] J. Friedel, *Can. J. Phys.* 34 (1956) 1190-1211.
- [12] S.A. Némov, Y. I. Ravich, *Phys.-Uspekhi* 41 (1998) 735-759.
- [13] S. Chen, P. Narang, H.A. Atwater, L. Wang, Phase stability and defect physics of a ternary ZnSnN₂ semiconductor: First principles insights, *Adv. Mater.* 26 (2014) 311–315.
- [14] N. Tsunoda, Y. Kumagai, A. Takahashi, F. Oba, *Phys. Rev. Appl.* 10 (2018) 011001.
- [15] S. Perumal, M. Samanta, T. Ghosh, U.S. Shenoy, A.K. Bohra, S. Bhattacharya, A. Singh, U.V. Waghmare, K. Biswas, *Joule* 3 (2019) 2565–2580.
- [16] S. Sarkar, X. Zhang, S. Hao, X. Hua, T.P. Bailey, C. Uher, C. Wolverton, V.P. Dravid, M.G. Kanatzidis, *ACS Energy Lett.* 3 (2018) 2593-2601.
- [17] M. Zhou, Z.M. Gibbs, H. Wang, Y. Han, L. Li, G. J. Snyder, *Appl. Phys. Lett.* 109 (2016) 42102.
- [18] N. Feldberg, J.D. Aldous, W.M. Linhart, L.J. Phillips, K. Durose, P.A. Stampe, R.J. Kennedy, D.O. Scalon, G. Vardar, R.L. Field, T.Y. Jen, R.S. Goldman, T.D. Veal, S.M. Durbin, *Appl. Phys. Lett.* 103 (2017) 42109.
- [19] A.N. Fioretti, A. Stokes, M.R. Young, B. Gorman, E.S. Toberer, A.C. Tamboli, A. Zakutayev, *Adv. Electron Mater.* 3 (2017) 1600544.
- [20] L. Lahourcade, N.C. Coronel, K.T. Delaney, S.K. Shukla, N.A. Spaldin, H.A. Atwater, *Adv. Mater.* 25 (2013) 2562–2566.
- [21] F. Alnjiman, S. Diliberto, J. Ghanbaja, E. Haye, S. Kassavetis, P. Patsalas, C. Gendarme, S. Bruyère, F. Cleymand, P. Miska, P. Boulet, J.F. Pierson, *Sol. Energy Mater. Sol. Cells* 182 (2018) 30–36.
- [22] I. Petrov, P.B. Barna, L. Hultman, J.E. Greene, *J. Vac. Sci. Technol. A* 21 (2003) S117–S128.
- [23] C. Cao, H.F. Chan, J. Zang, K.W. Leong, X. Zhao, *Adv. Mater.* 26 (2014) 1763–1770.
- [24] E. Alfonso, J. Olaya, and G. Cubillos, *Crystallization-Science and technology:*

- Thin film growth through sputtering technique and its applications, IntechOpen (2011) 397-432.
- [25] M. Pelliccione, T. Karabacak, C. Gaire, G. Wang, T. Lu, Phys. Rev. B 74 (2006) 1–10.
- [26] C. Jeong, R. Kim, M. Luisier, S. Datta, M. Lundstrom, J. Appl. Phys. 107 (2010).
- [27] N.J. Harrick, Appl. Opt. 10 (1971) 2344–2349.
- [28] J. Tauc, R. Grogrovici, A. Vancu, Phys. Stat. Soli. 15 (1966) 627–637.
- [29] A.S. Hassanien, A.A. Akl, J. Alloys. Compd. 648 (2015) 280-290.
- [30] A.N. Fioretti, A. Zakutayev, H. Moutinho, C. Melamed, J.D. Perkins, A.G. Norman, M. Al-jassim, S. Toberer, A.C. Tamboli, J. Mater. Chem. C 3 (2015) 11017–11028.
- [31] J.P. Heremans, V. Jovovic, E.S. Toberer, A. Saramat, K. Kurosaki, Anek, A. Charoenphakdee, S. Yamanaka, G.J. Snyder, Science 321 (2008) 554–558.
- [32] J. Pan, J. Cordell, G.J. Tucker, A.C. Tamboli, A. Zakutayev, S. Lany, Adv. Mater. 31 (2019) 1807406.
- [33] V. Y. Irkhin, Y. P. Irkhin, Electronic structure, correlation effects and physical properties of d- and f-metals and their compounds, Cambridge International Science Publishing, U.K. (2007).
- [34] K. Kaur, R. Kumar, D.P. Rai, J. Alloys Compd. (2018) 1-13.
- [35] Y. Pei, H. Wang, G.J. Snyder, Adv. Mater. 24 (2012) 6125–6135.
- [36] G.D. Mahan, J.O. Sofo, Proc. Natl. Acad. Sci. 93 (1996) 7436–7439.
- [37] Y. Kumagai, K. Harada, H. Akamatsu, K. Matsuzaki, F. Oba, Phys. Rev. Appl. 8 (2017) 014015.
- [38] M. Futsuhara, K. Yoshioka, O. Takai, Thin Solid Films 322 (1998) 274–281.
- [39] S.O. Kasap, Principles of electronic materials and devices, third ed. McGraw-Hill, U.S.A. (2006).
- [40] X. Li, H. Li, Z. Wang, H. Xia, Z. Xiong, Opt. Commun. 282 (2009) 247–252.

AUGMENTATION OF p-TYPE CONDUCTIVITY OF CHROMIUM NITRIDE THIN FILMS FOR DEVICE APPLICATIONS

Contents

-
- 5.1 Introduction
 - 5.2 Fabrication of thin films
 - 5.3 Results
 - 5.4 Discussion
 - 5.5 Conclusion
-

In this chapter, the transformation of the type of conductivity of chromium nitride thin film by inducing metal vacancy point defects is described in detail. The improvisation of the p-type conductivity and hence the thermoelectric power factor by changing the orientation of the crystallites are also discussed.

5.1 Introduction

The early transition metal nitrides, primarily based on scandium and chromium have emerged as an unexpected class of materials for energy harvesting [1]. The nitrides of titanium, hafnium and niobium transition metals are well established in industry as hard and wear resistant coatings. It becomes a unique class of compounds when these properties are combined with its good chemical and thermal stability and ease of thin film formation. The presence of strong metal-nitrogen covalent bonds with cubic crystal structure is the root cause for these characteristics. Most of these nitrides exhibit changes in crystallographic orientation with or without structural transitions [2]. During structural transitions, flipping of the entire magnetic system is usually perceivable. At the same time it shows semiconducting properties, hence find prominent place in microelectronics [3]. Chromium nitride (CrN) is a great candidate for electronic applications due to its moderate electrical resistivity, low thermal conductivity and varying crystal structure and magnetism with temperature [2,4].

Chromium nitride is a high oxidation resistant and stable semiconductor material with varying crystal structure and magnetic properties with temperature. At room temperature, it exhibits cubic NaCl structure with a space group $Fm\bar{3}m$ and

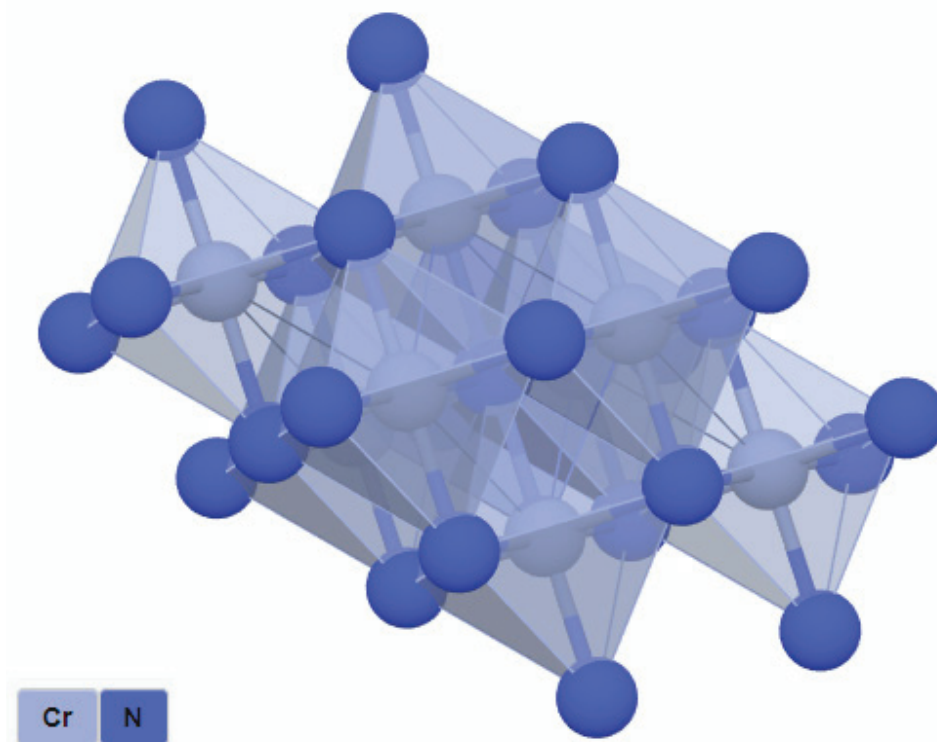


FIGURE 5.1. Crystal structure of CrN compound

lattice constant of 4.14 Å [4]. The crystal structure of CrN compound is shown in fig. 5.1 [5]. In this crystal system, each of the two atom types forms a separate face centered cubic lattice. Also, it can be viewed as face centered cubic structure with secondary atoms in its octahedral voids. It transforms the paramagnetic phase at temperature below Neel temperature, 13⁰C, to antiferromagnetic along with a crystallographic transition to orthorhombic. The CrN thin films exhibit different preferred orientations (PO) along (111), (200) and (220) planes with respect to the deposition conditions [6]. Hence, the variations in crystal structure, PO and magnetic phase are interrelated and these can be controlled by fabrication parameters. The electrical properties of CrN show wide variations and can be attributed to the variations in crystal structure and PO. The literature reports show that the resistivity values ranging from 0.1 to 350 mΩ m. Normally, the electrical resistivity is high due to large effective mass of the electrons from the localized 3d orbitals of Cr. It has a very narrow electronic and optical bandgap [7]. The electronic structure along with low thermal conductivity makes it as a promising candidate for thermoelectric applications. The formation energies of secondary phases and defects supplement the tuning of band structure and hence electrical resistivity and Seebeck coefficient [8,9]. The variation in PO can also be utilized to extract the maximum thermoelectric properties.

The thermoelectric and photovoltaic energy conversion techniques require n and p-type materials for device fabrication. The thermoelectric generators are setup by alternatively attaching n- and p-type materials and p-n junction in the photovoltaic devices are formed by depositing one type of material on another one [10–13]. The energy conversion efficiency of these devices are greatly depends on the parameters of each individual material. The matching of thermodynamic and physical properties is essential for stable device performance. When the devices are fabricated using n-type of nitrides, p-type of nitrides can greatly supplement to obtain stable maximum efficiency [14,15]. During p-n junction formation, the lattice mismatch between materials leads to formation of ohmic contacts. In case of oxides, copper oxide and nickel oxide perform the role of p-type but in nitrides no such materials are found out.

The p-type conductivity in these oxides is normally stems from the deficiency of metal atoms [16,17].

The defect chemistry of chromium nitride greatly supports to transform it as a p-type material by creating chromium deficiencies. In a nitrogen (N) rich condition, CrN exhibits the lowest overall energy in presence of Cr vacancies. In addition to this, the formation energy for N antisite configuration has only 17 meV difference with Cr vacancy configuration. The detailed study of point defects in CrN by D. Holec et al. revealed that Cr vacancies in addition to N antisites are the most favorable point defects in experimental samples of CrN deposited in N rich condition. The chemical potential environment to create these point defects can be easily created by optimizing the sputtering parameters during thin film deposition. The high Seebeck coefficient and low thermal conductivity with these defect features can transform the CrN thin films as an excellent material having p-type conductivity [8,18]. This chapter deals with the formation and optimization of point defects in CrN to transform it as a p-type material by controlling the growth kinetics during the thin film deposition. The optimization of the preferred orientations of CrN thin films to improve the conductivity for thermoelectric applications is also discussed.

5.2 Fabrication of CrN thin films

The CrN thin films were deposited on quartz substrates with dimension 10x10x2 mm using reactive RF magnetron sputtering with a 99.99% pure chromium target of 50 mm in diameter and 3 mm thick. Before the deposition, the quartz substrates were cleaned by standard solution cleaning method followed by ultrasonic cleaning in acetone and finally dried in an oven [19]. We carried out different analysis based on the various deposition parameters which determine the physical properties of the thin film. The effect of substrate temperature and sputtering power on structural and electrical properties of the CrN thin film were investigated. These studies provided a precise picture of the optimized sputtering parameters to deposit the CrN thin films for the investigation of p-type thermoelectric material. Nitrogen gas with 99.999% pure was used as both sputtering and reactive gas. The separation distance between the substrate and the target was fixed as 80 mm. The base pressure was about 6×10^{-6} mbar before the entry of N₂ gas into the chamber. For all the deposited films,

the base pressure, sputtering power of 150W, substrate temperature of 450⁰C and thickness of 600 nm were kept constant while sputtering pressure was set to different values. Before conducting the reactive sputtering, the chamber was evacuated to ultimate vacuum of 6x10⁻⁶ mbar; purging the N₂ gas in to the chamber and control for different sputtering pressures in between 1x10⁻² mbar and 5x10⁻² mbar. The increase in nitrogen pressure of reactive sputtering reduced both working pressure and amount of reactive nitrogen. The thin film deposition continued up to which the quartz crystal thickness monitor showing the required thickness. Table 5.1 shows the optimized deposition parameters for CrN reactive sputtering.

TABLE 5.1. Deposition parameters optimized for CrN reactive sputtering

Parameter	Specification
Fabrication Technique	Reactive RF magnetron sputtering
Target	Cr 99.99% pure and 50x3 mm size
Substrate	Quartz with 99.999% pure and 10x10x2mm
Sputtering & Reactive Gas	Nitrogen
Target-Substrate Distance	8 cm
Sputtering Power	150 W
Substrate Temperature	450 ⁰ C
Ultimate Vacuum	6x10 ⁻⁶ mbar
Working Pressure	1x10 ⁻² mbar - 5x10 ⁻² mbar
Film Thickness	~600 nm

5.3 Results

5.3.1 Phase and crystallographic features

The phase and crystallographic parameters of the deposited CrN thin films were elucidated using X-ray diffraction technique. The analysis was performed by powder XRD analysis software, PDXL complemented by the ICDD database. The X-ray diffractogram of thin films deposited at different N₂ gas pressure are shown in fig. 5.2. The comparison of the diffractogram with standard ICDD data (ICDD No. 01-074-8390) ensures the evolution of CrN phase in all the reactively sputtered thin films. It is shown that the thin films were polycrystalline and all the peaks were indexed with

the cubic phase of CrN with space group $Fm\bar{3}m$ [20]. The major XRD peaks were observed with diffractions of (111), (200) and (220) planes. The variations in the intensities of the diffraction planes were observed for thin films deposited at various N_2 gas pressure. At lowest N_2 gas pressure, the diffractions of (111) plane around 36.9° was dominant. When increasing N_2 gas pressure, intensities of all the peaks were decreased with sustaining (111) PO up to the N_2 gas pressure of 2×10^{-2} mbar. Further increase in N_2 gas pressure to higher values decreased the intensity of (111) diffraction and gradually increased the (200) diffraction intensities. The thin films sputtered at these N_2 gas pressures have PO along (200) plane around $\sim 43.7^\circ$. During the transformation of PO from (111) to (200), the thin films deposited at 3×10^{-2} mbar shows a small indication of growth of (220) planes. The decrease in total intensity of the reflections from all planes with increasing N_2 gas pressure ensured the reduction in crystallinity of the CrN thin films with PO.

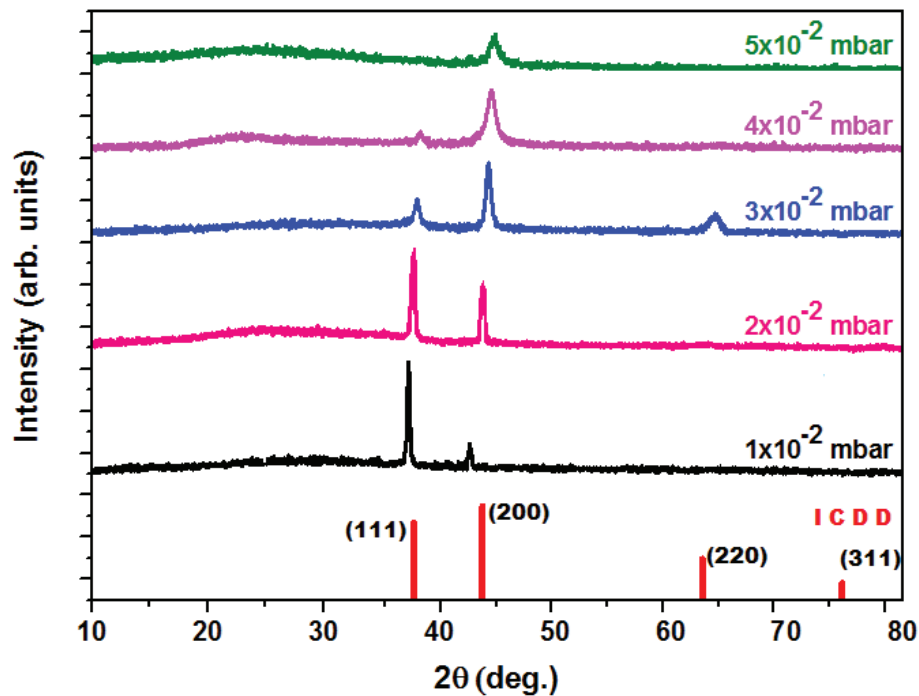


FIGURE 5.2. XRD of sputtered CrN thin films having varying PO with N_2 pressure

5.3.2 Thickness

The thickness of the thin films was estimated by AFM. It measures the height of the step created by partially masking the substrate during sputtering as shown in fig. 5.3. The thickness of all the sputtered thin films is ~ 600 nm.

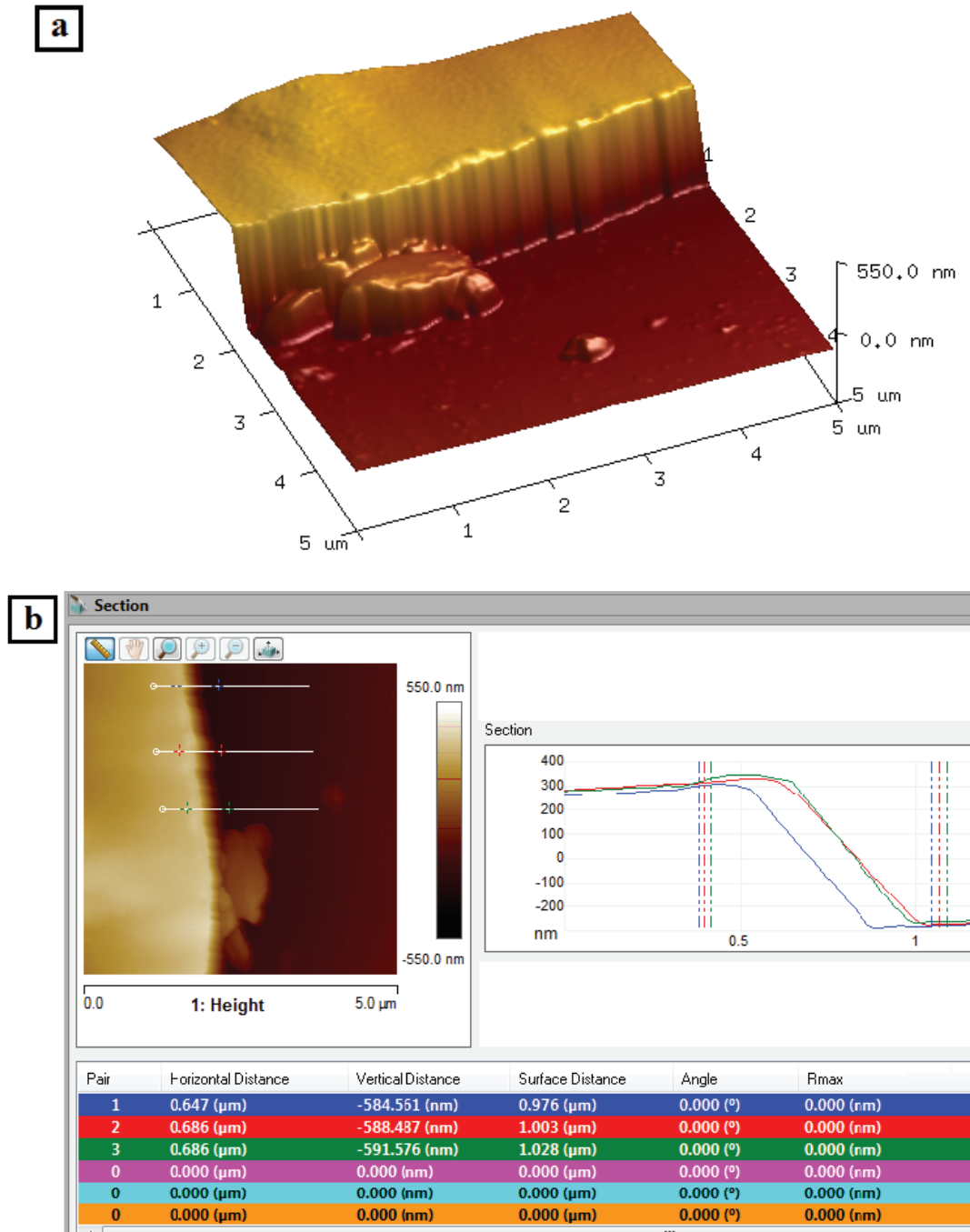


FIGURE 5.3. (a) Surface topography and (b) step parameters of partially coated CrN thin film

5.3.3 Surface features

The surface features of the deposited CrN thin films are obtained by an integrated analysis of the conductive atomic force microscopy. The CAFM maps the charge density on the sample surface during the current flow along with topographic profile. The current distribution profile of the thin films is discussed under the section ‘electronic transport properties’. The 3D images of the topographic features of CrN

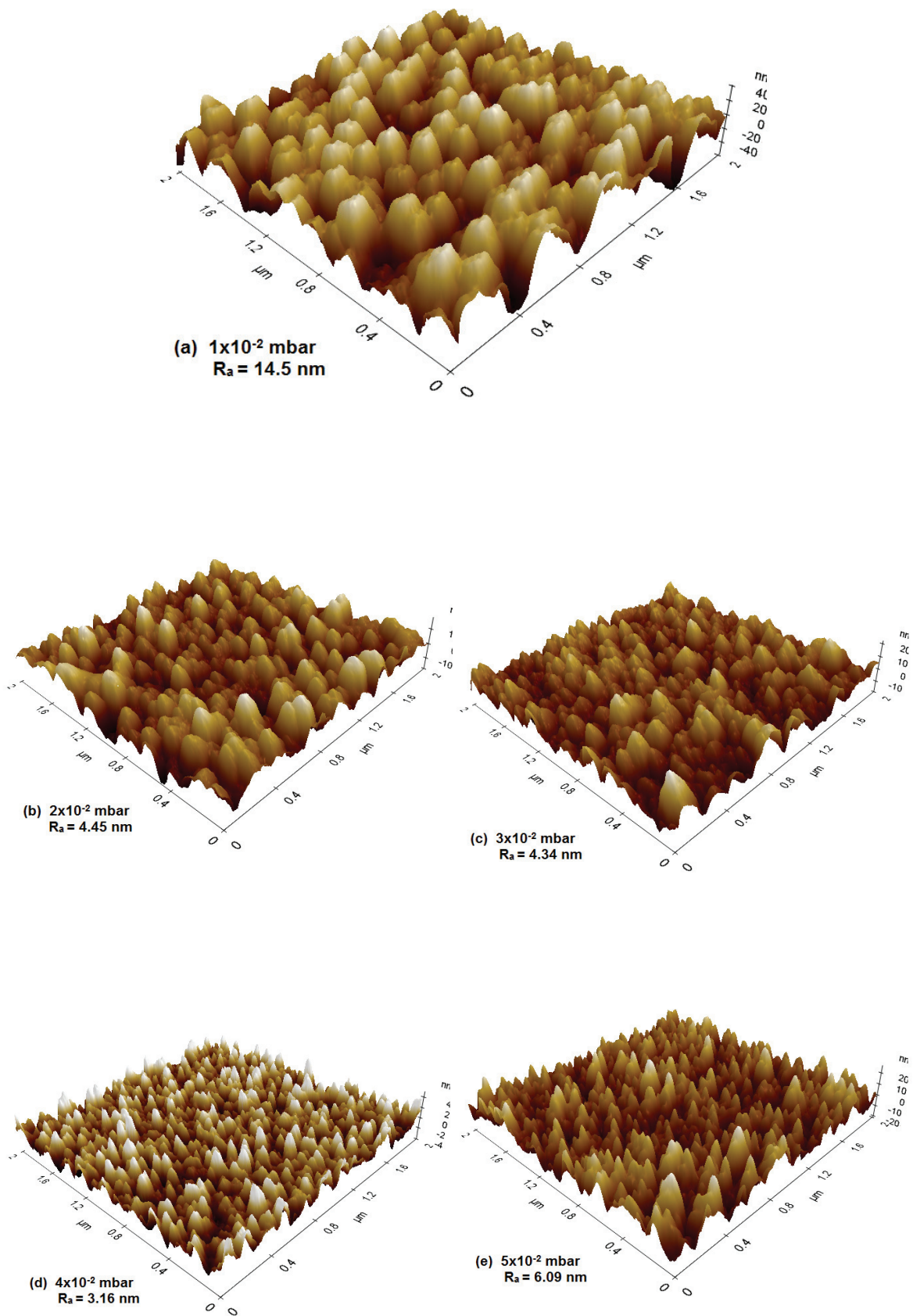


FIGURE 5.4. AFM topography with average surface roughness of CrN thin films

with varying N₂ pressure are shown in fig. 5.4. The analysis of horizontal and vertical dimensions of topographic images shows that the size of the particles is in nanometer range and the surfaces are very smooth. The particle size is decreasing with increase in N₂ pressure due to the variation in growth formalism results from the decreased energy of the adsorbed atoms. The reduction in energy delivered to the target atoms by plasma ions and the increased collision of the sputtered atoms due to the increased N₂ pressure decreases the energy of the atoms adsorbed on the surface of the thin films. It reduces the mobility of the adatoms and hence affects the nucleation and growth of the crystallites [21,22].

5.3.4 Electronic transport properties

The carrier concentration and mobility estimated from Hall measurement are shown in fig. 5.5. The lower nitrogen pressure always supplement the nitride compounds to grow with the donor type defects such as nitrogen vacancies and metal interstitials [6,8]. The CrN thin films deposited at lower pressure exhibits n-type conductivity due to the presence of nitrogen vacancies and Cr interstitials [9,18]. The formation energy of these point defects in the nitrogen deficient environment is low compared to other defects. The nitrogen vacancies and Cr interstitials donate three and four electrons respectively to the CrN. Hence, the electron concentration is high and shows n-type conductivity. The increase in nitrogen pressure reduces the nitrogen deficiency hence, the density of donor type point defects are decreased. It decreases the carrier concentration of the CrN thin films. When the nitrogen pressure reduced to 4×10^{-2} mbar, the nitrogen rich growth condition develops for the CrN thin films. This growth kinetics favours the CrN to grow with Cr vacancies and N antisites [8,23]. The high density of acceptor point defects neutralizes the electron charge carriers and the CrN thin films exhibits p-type conductivity. The density of the acceptor point defects increases with nitrogen pressure and showing improvement in hole concentration. The competition between donor and acceptor point defects due to small difference in their formation energies limits the carrier concentration of CrN to low values. This is the major reason for the high resistivity of p-type thin films. The variation of the carrier concentration of the CrN thin films with N₂ pressure are summarised in table. 5.2.

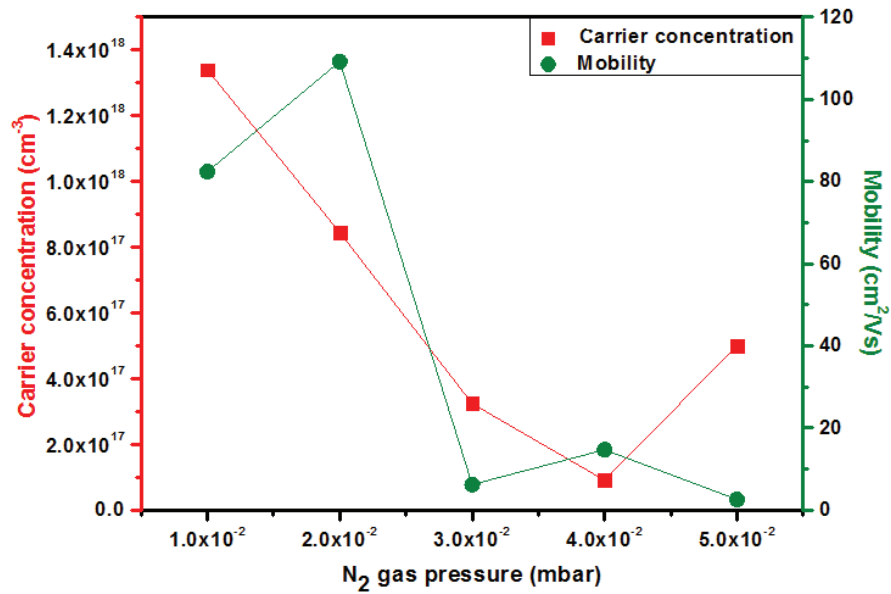


FIGURE 5.5. Variation of carrier concentration and mobility of CrN thin films with N₂ gas pressure

The realization of nanoscale current behavior of thin films is fundamentally important for the exploration of the electronic properties. It is more important and interesting when the material is new one and showing both n and p-type conductivities. In case of thin films, the conducting behavior of surface has considerable role in the total conductivity of the material [24]. The current charging and distribution phenomena on the surface of the CrN thin films were explored by conductive atomic force microscopy (CAFM). Also, the change in type of conductivity of the thin films with N₂ pressure was confirmed from the direction of current distribution [25,26]. The CAFM map the local charge distribution on the sample surface during the current flow along with topographic profile [27]. In our CAFM measurement system, current flowing from sample to tip is considered as positive by convention and the tip is referenced to the ground. The detailed experimental setup and procedure were discussed under atomic force microscopy of chapter 2.

The intensity of the charge distribution on the surface of the thin films at a bias voltage of 0V is depicted in fig. 5.6. The strength of the current distribution increases with the decrease in N₂ pressure which is directly related to the resistivity that obtained from the thermoelectric characterization. This variation is observed from the maximum value of the z-axis of the current images. The current flowing through the

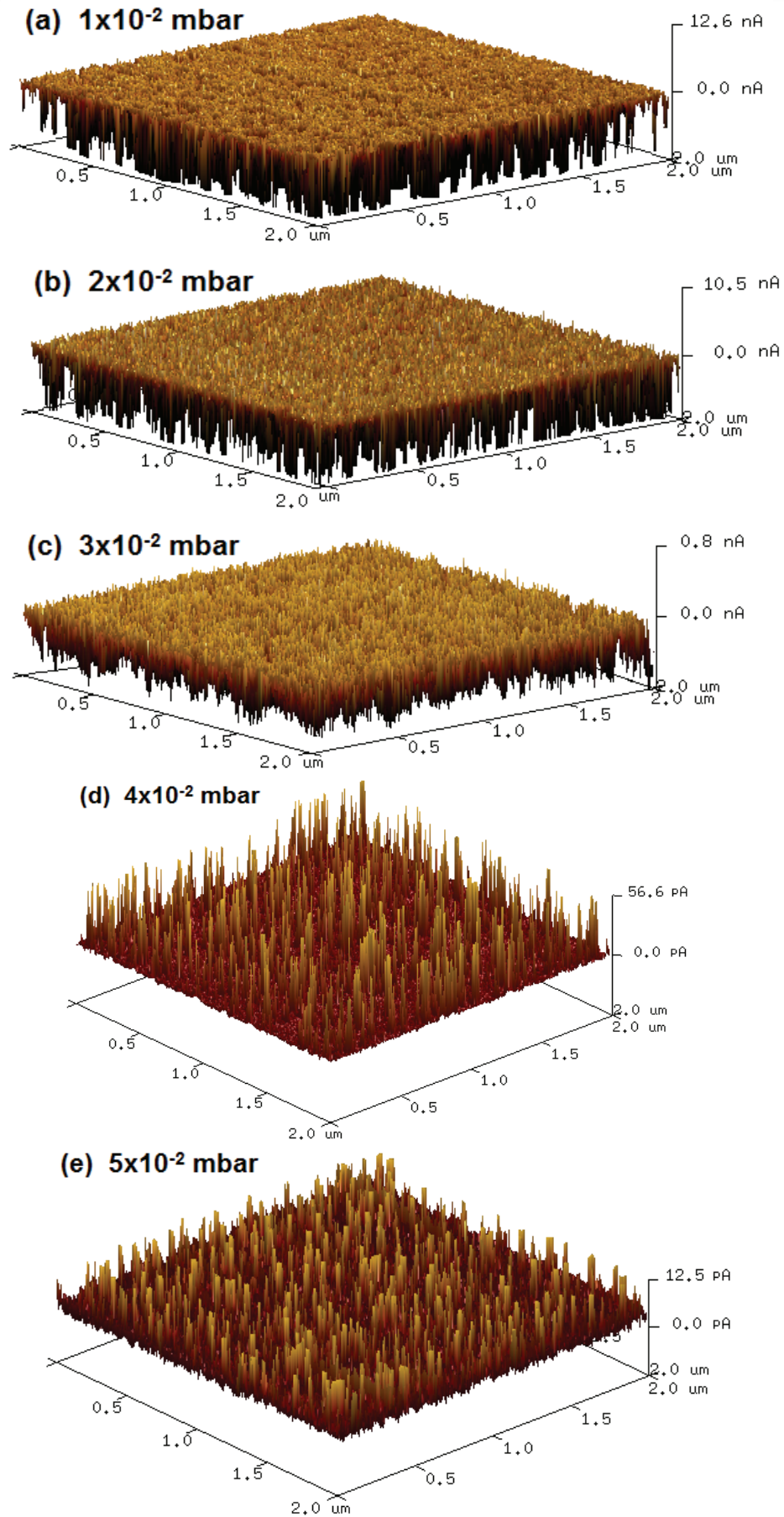


FIGURE 5.6. CAFM 3D current distribution profile of CrN thin films at different N_2 pressure

surface particles are negative for the thin films sputtered at the N_2 pressure up to 3×10^{-2} mbar. Thereafter during the reduction, the current is positive. The current flowing from sample to tip is considered as positive by convention. Hence, the negative current detected by the tip which is shown as downward in 3D images ensures that current is flowing from tip to sample and negative charges are stored within the particles. Similarly, the upward current in the image demonstrates that positive charges are stored in the particles and the thin film having p-type conductivity. These factors have already been obtained from Hall and Seebeck measurements. In addition to this, it is observable that the spreading of current distribution in particles decreases with the resistivity. It can be attributed to many factors like particle size, crystallinity, carrier concentration and PO. Each parameter has its own contribution, hence the spreading of the current distribution is the resultant of the influences of these factors.

5.3.5 Thermoelectric properties

Thermoelectric power factor is determined by the Seebeck coefficient and electrical conductivity of the material. The temperature depended thermoelectric properties of the prepared CrN thin films from RT to $400^{\circ}C$ are shown in fig. 5.7. The carrier concentration and mobility are the key parameters which determine the resistivity of thin films [28]. The variation of resistivity with N_2 pressure clearly follows its correlation with concentration and mobility of charge carriers. The high increase in resistivity of thin film deposited at 3×10^{-2} mbar is due to the large reduction in mobility of electrons. Even though the p-type CrN fabricated at 5×10^{-2} mbar has significant increase in carrier concentration, it doesn't show any reduction in resistivity. In these two samples, the effect of mobility on resistivity predominates over that of carrier concentration. Apart from this, the resistivity of all samples clearly follows the variations of carrier concentration. The Seebeck coefficient has negative and positive values for CrN prepared at lower and higher pressures respectively. This is due to the change in majority charge carriers originated from the Cr vacancy and N interstitial point defects. This is well agreement with the results obtained from the Hall and CAFM measurement. In normal conditions, the Seebeck coefficient is a covariance parameter with resistivity. The variation of Seebeck coefficient of all prepared thin films has direct relation with resistivity variation except for that

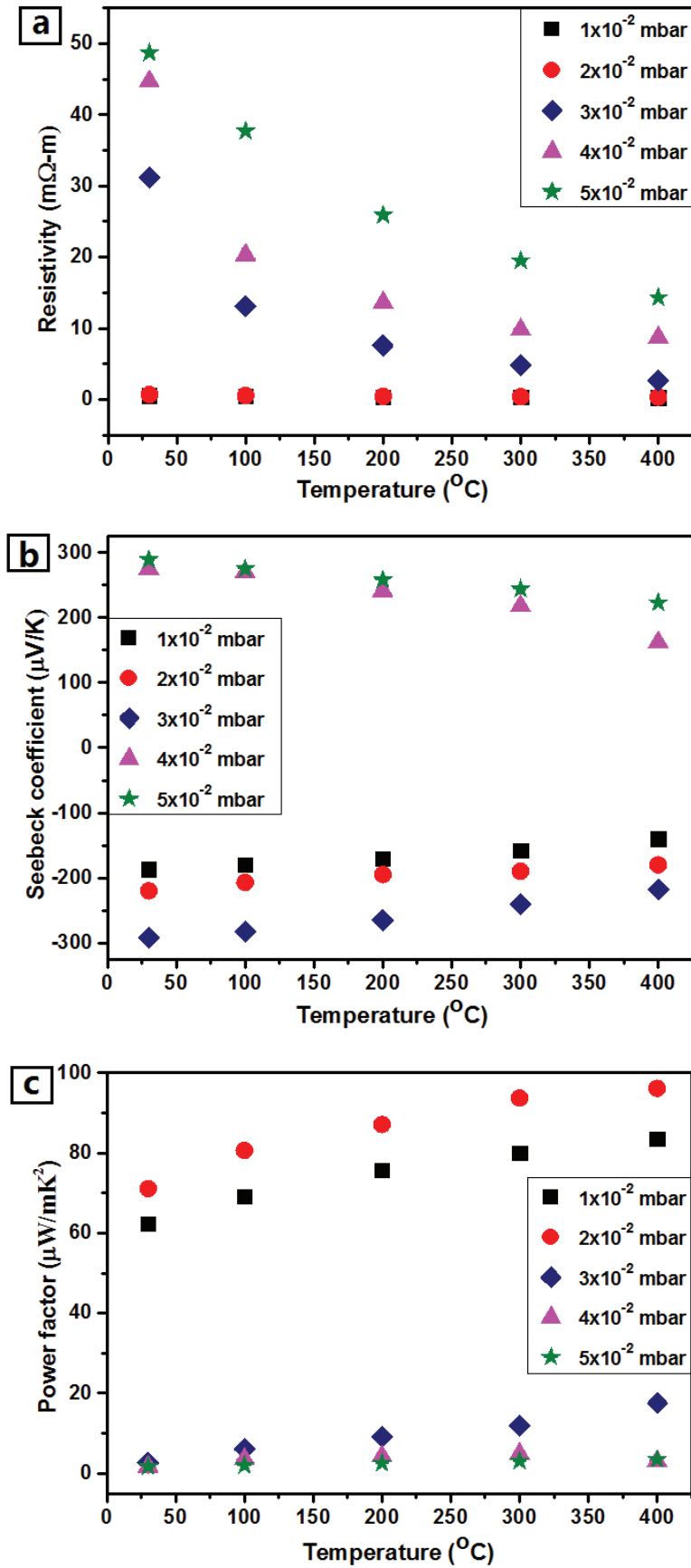


FIGURE 5.7. Temperature dependent (a) resistivity (b) Seebeck coefficient and (c) power factor of CrN thin films sputtered at different N_2 pressure

prepared at 3×10^{-2} mbar. This CrN belongs to an intermediate stage of the transition of conductivity from n- to p-type. Hence, at low temperatures the conductivity is bipolar in nature due to contributions from both electrons and holes especially in narrow bandgap semiconductors [29]. This can also be sensible from the high variations of resistivity at lower temperatures of the films sputtered at 3×10^{-2} and 4×10^{-2} mbar pressures. When the temperature increases from RT to 100°C , the presence of high majority carriers annihilates the minority carriers and its effects are vanished. The variations in power factor reflect the resistivity and Seebeck coefficient characteristics. The thermoelectric parameters of n- and p-type CrN at RT are summarized in table 5.2.

5.4 Discussion

The CrN thin films having p-type conductivity were successfully fabricated by controlling the growth kinetics during sputtering. The Cr vacancies and N antisites acceptor point defects transformed the n-type conductivity of CrN to p-type. The defect chemistry of CrN warrants the high N-rich atmosphere for the creation of these point defects. Hence, the increase in N_2 pressure enhances the working pressure of sputtering due to the presence of pressurized plasma. The energy of the sputtered and adsorbed atoms is reduced by the increased collision with plasma results in significant deterioration of the crystallinity [30]. In addition to this, the reduction of strain energy originated from the reduced energy of adsorbed atoms makes the surface energy as the main contributor to the total energy of the developing thin films. It changes the preferred orientation of the thin films from (111) to (200), a process for total energy minimization by changing the growth of crystallites from lowest strain energy orientation to lowest surface energy orientation [5,31,32]. But, the change in preferred orientation along with reduced crystallinity significantly worsens the mobility and power factor of the thin films. In NaCl type lattice systems, the highest planar density belongs to the (200) plane followed by (220) and (111). The high atomic density of (200) plane is the main reason for high resistivity of p-type CrN. This is clearly evident from the sharp increase in the resistivity of CrN having (200) PO, sputtered at 3×10^{-2} mbar. This is the reason for the absence of any reduction in resistivity of p-type CrN fabricated at 5×10^{-2} mbar even the carrier concentration was increased

TABLE 5.2. Thermoelectric parameters of CrN thin films at RT sputtered with various N₂ pressures

<i>N₂ gas pressure (mbar)</i>	<i>Preferred orientation</i>	<i>Carrier concentration (cm⁻²)</i>	<i>Mobility (cm²/V s)</i>	<i>Resistivity (mΩ m)</i>	<i>Seebeck coefficient (μV/K)</i>	<i>Power factor (μW/m K²)</i>
1 x 10 ⁻²	(111)	1.34 x 10 ¹⁸	82.4	0.57	-187	62.00
2 x 10 ⁻²	(111)	8.45 x 10 ¹⁷	109.1	0.68	-220	71.14
3 x 10 ⁻²	(200)	3.24 x 10 ¹⁷	6.2	31.21	-292	27.32
4 x 10 ⁻²	(200)	9.05 x 10 ¹⁶	15.4	44.78	275	1.69
5 x 10 ⁻²	(200)	5.01 x 10 ¹⁷	2.6	48.74	294	1.78

significantly. The keen observation of the variations in carrier concentration, mobility and resistivity clearly validates this matter. At RT, the CrN thin film having p-type conductivity shows the resistivity of 44.78 *mΩm* with hole mobility of 2.6 *cm²/V s*. It shows power factor of 1.78 *μW/m K²* with Seebeck coefficient of 294 *μV/K*. Since the effective mass of holes is very low compared with electrons in CrN, we expect a large improvement in charge carrier mobility of p-type CrN.

In order to utilize in device applications, good conductivity of p-type material is a basic requirement [33–35]. The conductivity of p-type CrN can be improved by increasing the mobility. Here, the mobility is greatly depends on crystallinity and PO. The mobility of charge carriers will be improved in CrN thin films having low dense planes. The p-type conductivity and (111) oriented crystallites can't be achieved together in point defect induced CrN. On the other hand the precise variation in surface and strain energies should develop (220) oriented crystallites in p-type conductive CrN. Normally, the transformation between lowest energy planes during the energy minimization process is through the intermediate planes. The intermediate planes have bit role in this process, hence its presence is in a narrow window. The energy variation during the reduction of pressure is high compared to that of substrate temperature and power [36,37]. So, the preparation of CrN thin films with PO along (220) plane is tedious by controlling the N₂ pressure.

When optimizing the crystallinity and PO together, the precise control of the deposition parameters is required. To transform the PO of the thin films from (200) to (220), the surface energy is reduced while increasing the strain energy. The reduction in substrate temperature along with increase in sputtering power varies the contribution of the surface and strain energies to the total energy of the system [31,38]. It should supplement the growth of the intermediate plane, (220) in CrN. Also, the increase in power improves the crystallinity of the thin films. The CrN sputtered at 4×10^{-2} mbar is chosen for further optimization because of its better performance in thermoelectric point of view. Also, the CrN deposited at 3×10^{-2} mbar shows an indication of the presence of (220) oriented crystallites. The phase, PO and crystallinity of the CrN thin films sputtered at a N_2 pressure of 4×10^{-2} mbar and substrate temperature of 400°C with different sputtering power of 175 W and 200 W are depicted in fig. 5.8.

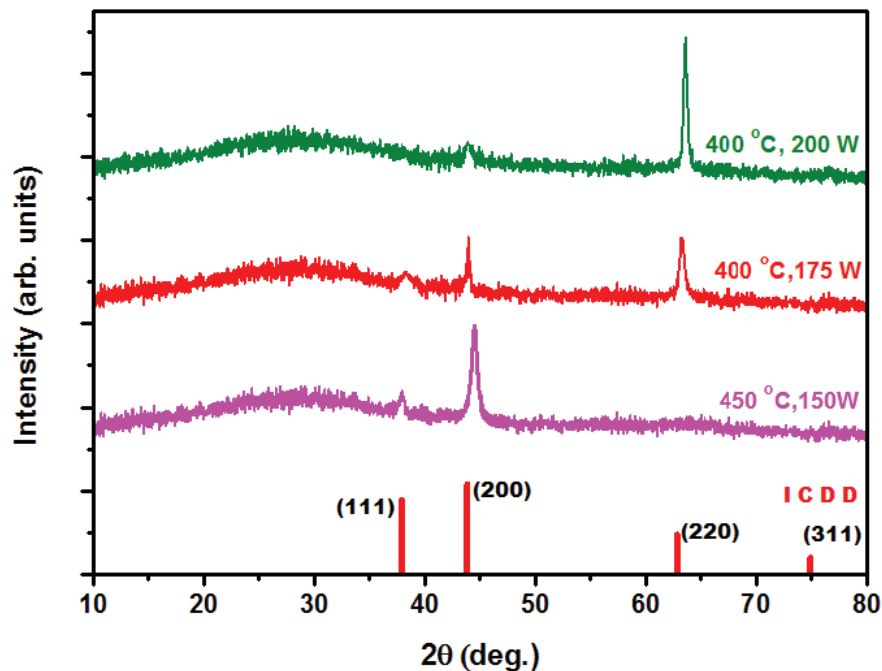


FIGURE 5.8. XRD of sputtered CrN thin films with (220) PO

The CrN thin films with crystallites having (220) orientation exhibit significant reduction in resistivity and it results in improved thermoelectric power factor. This is originated from the enhanced mobility by the change in orientation of crystallites

along low dense plane, (220) with improved crystallinity. The p-type CrN thin film improved the power factor from 1.69 to 24.43 $\mu W/m K^2$ with an increase in mobility from 15.4 to 181.7 $cm^2/V s$. The electronic and thermoelectric transport parameters are listed in table 5.3 for realizing its improvement in comparison with CrN having (200) PO.

TABLE 5.3. The TE parameters of CrN thin films at RT with different PO

<i>Deposition parameters</i>	<i>Preferred orientation</i>	<i>Mobility</i>	<i>Resistivity</i>	<i>Seebeck coefficient</i>	<i>Power factor</i>
	<i>(hkl)</i>	<i>($cm^2/V s$)</i>	<i>($m\Omega m$)</i>	<i>($\mu V/K$)</i>	<i>($\mu W/m K^2$)</i>
4 x 10 ⁻² mbar 450 ⁰ C 150 W	(200)	15.4	44.78	275	1.69
4 x 10 ⁻² mbar 400 ⁰ C 175 W	(220)	90.6	7.53	322	13.78
4 x 10 ⁻² mbar 400 ⁰ C 200 W	(220)	181.7	3.71	301	24.43

The current charging and distribution phenomena on the surface of the CrN thin films with different PO were explored by conductive atomic force microscopy (CAFM). For better understanding, the current distribution of the p-type CrN as a function of applied bias was investigated [26,39]. The current distribution of the CrN with lowest resistivity due to (200) PO (sputtered at 4x10⁻² mbar, 400⁰C and 200 W) was compared with the thin film having high resistivity with (220) PO (sputtered at 4x10⁻² mbar, 450⁰C and 150 W). The 2D images of the topographic features and current distribution with different biasing of these two thin films are shown in fig. 5.9.

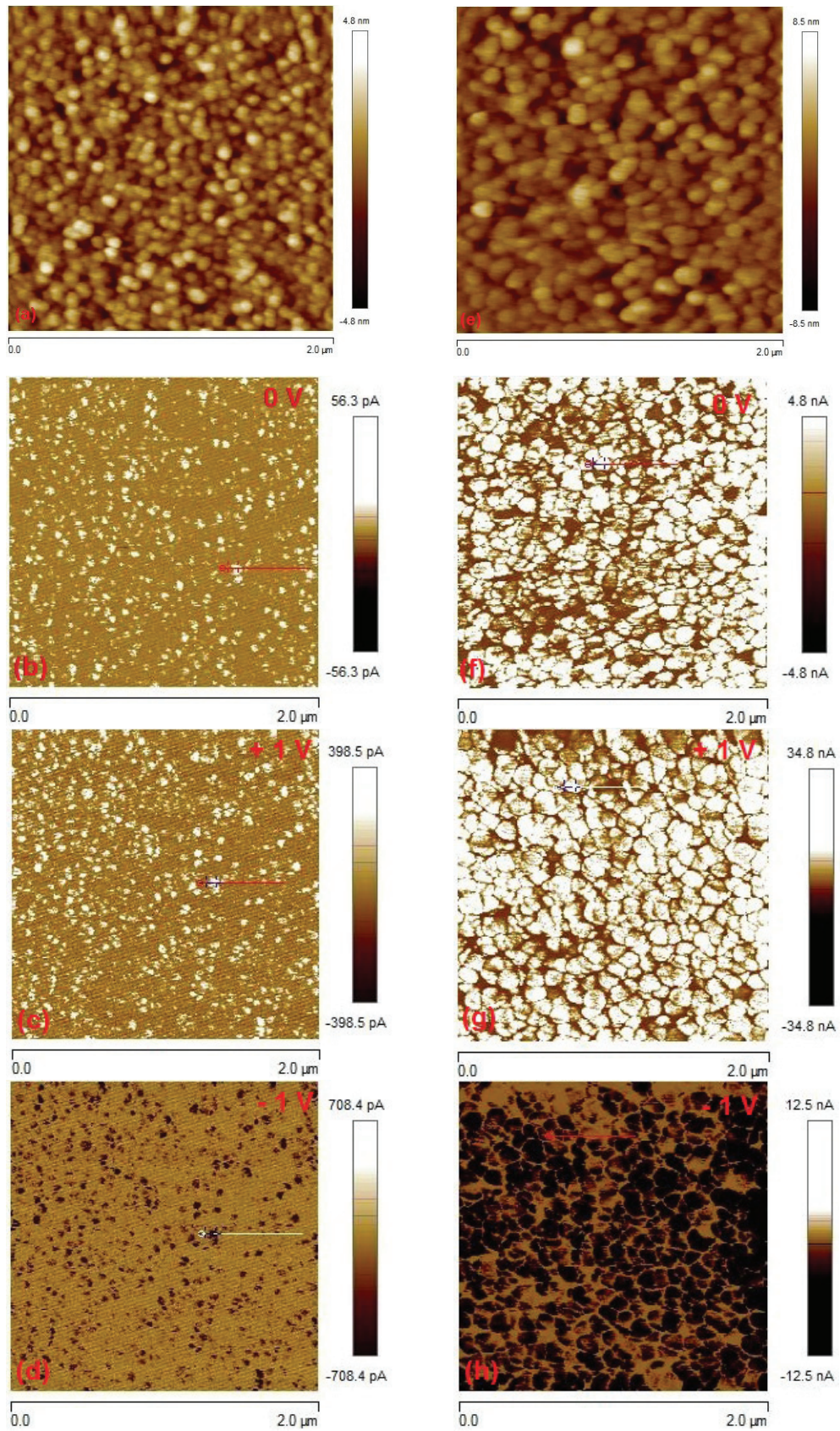


FIGURE 5.9. CAFM 2D images of topographic (a & e) and current distribution (other than a & e) profile of CrN thin films with (200) PO (sputtered at 4×10^{-2} mbar, 400°C and 200 W) (first column) and (220) PO (sputtered at 4×10^{-2} mbar, 450°C and 150 W) (second column)

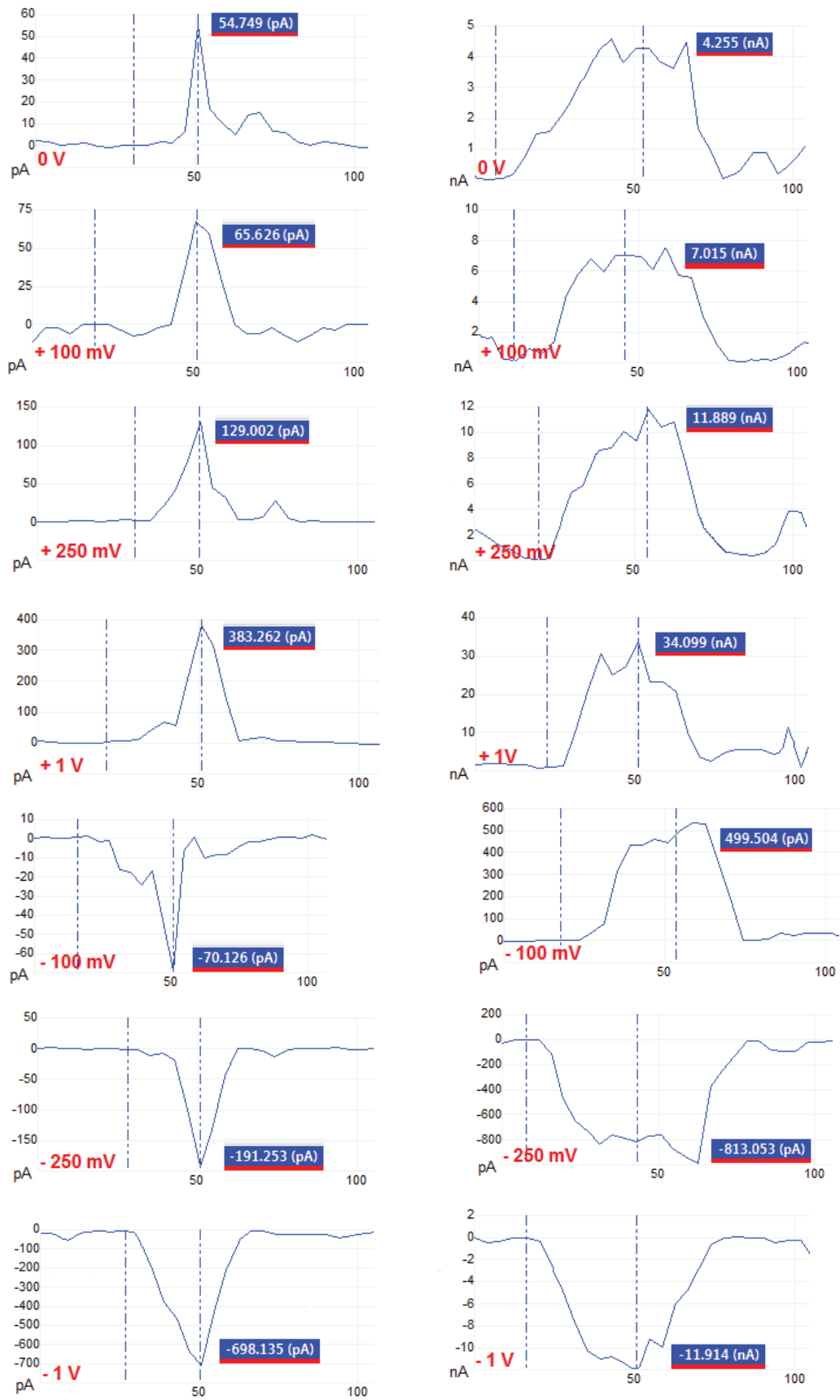


FIGURE 5.10. CAFM current distribution profile of a particle of CrN thin films with (200) PO (sputtered at 4×10^{-2} mbar, 400°C and 200 W) (first column) and (220) PO (sputtered at 4×10^{-2} mbar, 450°C and 150 W) (second column)

The remarkable increase in the spread of the charge distribution exists in the CrN having lowest resistivity. Out of various parameters which determine the charge distribution, the particle size, carrier concentration and crystallinity have minor role in this scenario. The variation in the above mentioned parameters of the CrN which have been chosen for the specific analysis is low. Hence, the spreading of the charge distribution can be attributed to the change of the PO of the crystallites from (200) to (220). The high dense planes (200) restrict the flow of charge carriers hence, the charge distribution is confined to the centre area of the particles [27,39,40]. When changing the crystallite orientation along (220) direction, the low planar density realize the smooth flow of charges resulting in the spread of the charge carriers from the centre to the periphery of the particles. For proximity to the current distribution system, the variation in current distribution of a single particle with applied bias is analyzed and given in fig. 5.10. The peak current of the particles are increasing with biasing voltage and changes its direction with reverse biasing. In low biasing conditions the peak current is small because the localized energy states involved in the charge transportation is low. When the biasing voltage increases, more localized energy states contribute to the current flow resulting in enhanced peak current [41,42]. The current profile of the low resistance CrN at a reverse bias of -100 mV exhibited a positive current of 499 pA. The reverse bias of -100 mV is not enough to charge the p-type CrN particles by electrons. Also, the value of current during the forward biasing of +1 V is very high compared with the other one. These features show the strength and stability of the p-type conductivity exhibited by the CrN thin films.

5.5 Conclusion

The efficient and stable performance of nitride based thin film devices requires intrinsic semiconductors of nitrides having n- and p-type conductivities. Thin films of earth abundant and nontoxic CrN having p-type conductivity were successfully fabricated by reactive radio frequency magnetron sputtering. The Cr vacancies and N antisites acceptor point defects transformed the n-type conductivity of CrN to p-type by creating N-rich growth condition. This fabrication condition increased the working pressure and the PO of the crystallites was changed from (111) to (200). It significantly decreased the mobility, hence conductivity of the CrN thin films due to

the high planar density of (200). For the efficient application in devices, the CrN thin films having the orientation of crystallites along (220) plane was fabricated by optimizing the deposition parameters. These thin films showed improved p-type conductivity along with moderate thermoelectric power factor. The p-type CrN thin film showed a power factor of $24.43 \mu W/m K^2$ with Seebeck coefficient of $301 \mu V/K$ and resistivity of $3.71 m\Omega m$ at RT. Also, the root cause behind the improvement in conductivity of CrN thin films with orientation of crystallites along (220) plane was explored by surface charge density mapping. The remarkable increase in the spread of the charge carriers in each particle increased the mobility and hence, conductivity of the thin films. Thus, this study greatly support the investigations on p-type conductive intrinsic semiconductors of nitride thin films and physical properties of thin films having preferred orientations.

References

- [1] P. Eklund, S. Kerdsonpanya, B. Alling, J. Mater. Chem. C. 4 (2016) 3905–3914.
- [2] S. Tan, X. Zhang, X. Wu, F. Fang, J. Jiang, Thin Solid Films. 519 (2011) 2116–2120.
- [3] L. Hultman, Thermal stability of nitride thin films, Vacuum 57 (2000) 1–30.
- [4] L. Zhou, F. Kormann, D. Holec, M. Bartosik, B. Grabowski, J. Neugebauer, P.H. Mayrhofer, Phys. Rev. B 90 (2014) 184102.
- [5] <https://materialsproject.org/materials/mp-1000440/>.
- [6] B. Subramanian, K. Prabakaran, M. Jayachandran, Bull. Mater. Sci. 35 (2012) 505–511.
- [7] M.A. Gharavi, S. Kerdsonpanya, S. Schmidt, F. Eriksson, N.V. Nong, J. Lu, B. Balke, D. Fournier, L. Belliard, A. Febvrier, C. Pallier, P. Eklund, J. Phys. D: Appl. Phys. 52 (2018) 355302.
- [8] D. Holec, L. Zhou, Z. Zhang, P.H. Mayrhofer, Impact of point defects on the electronic structure of paramagnetic CrN, arXiv preprint (2018) arXiv:1410.0758.
- [9] E. Mozafari, B. Alling, P. Steneteg, I.A. Abrikosov, Phys. Rev. B. 91 (2015) 094101.
- [10] X.F. Zheng, C.X. Liu, Y.Y. Yan, Q. Wang, Renew. Sustain. Energy Rev. 32 (2014) 486–503.

- [11] B. Cai, H. Hu, H. Zhuang, J. Li, *J. Alloys Compd.* 806 (2019) 471–486.
- [12] M. Kemell, M. Ritala, M. Leskela, *Crit. Rev. Solid State Mater. Sci.* 30 (2005) 1–31.
- [13] J. Nelson, *The Physics of Solar Cells*, Imperial College Press, London (2008).
- [14] N. Lu, I. Ferguson, *Semicond. Sci. Tech.* 23 (2013) 74023.
- [15] N. Lu, I. Ferguson, *Semicond. Sci. Tech.* 23 (2013) 74023.
- [16] J. Linnera, G. Sansone, L. Maschio, A.J. Karttunen, *J. Phys. Chem. C* 122 (2018) 15180-15189.
- [17] S. Joshi, M. Mudigere, L. Krishnamurthy, G.L. Shekar, *Chem. Papers-Slovak Acad. Sci.* 68 (2015) 1484-1592.
- [18] T. Rojas, S.E. Ulloa, *Phys. Rev. B.* 98 (2018) 214111.
- [19] G. Shugar and J. Ballinger, *Chemical technicians' ready reference handbook*, Tata Mc-Graw Hill, U.S.A. (1996).
- [20] International Centre for Diffraction Data, PDF Card Number 01-074-8390, (2010) 1-4.
- [21] J.A. Thornton, *J. Vac. Sci. Tech.* 11 (1974) 666–670.
- [22] M. Pelliccione, T. Karabacak, C. Gaire, G. Wang, T. Lu, *Phys. Rev. B.* 74 (2006) 125420.
- [23] A. Febvrier, N. Van Nong, G. Abadias, P. Eklund, *Appl. Phys. Express* 11 (2018) 051003.
- [24] K.D. Leaver, B.N. Chapman, *Thin Films*, Wykeham Publication, London (1971).
- [25] C.I. Zanetti, A. Mechler, *Applications of conductive atomic force microscopy*, Wiley Analytical Science, 2005.
- [26] R. Wu, S.L. Zhang, J.H. Lin, Z.M. Jiang, X.J. Yang, *Nanotechnology* 22 (2011) 095708.
- [27] Y. Zhang, F. Ye, J. Lin, Z. Jiang, X. Yang, *Nanoscale Res. Lett.* 7 (2012) 278.
- [28] C. Kittel, *Introduction to solid state physics*, John Wiley & Sons, U.S.A. (2005).
- [29] T. Yamamoto, H. Fukuyama, *J. Phys. Soc. Jpn.* 87 (2018) 114710.
- [30] B.D. Cullity, *Elements of X-ray diffraction*, Addison-Wesley, U.S.A. (1956).
- [31] H.H. Yang, J.H. Je, and K.B. Lee, *J. Mater. Sci. Lett.* 14 (1995) 1635–1637.
- [32] E. Iborra, M. Clement, J. Sangrador, A. S. Hervas, L. Vergara, M. Aguilar, *IEEE Trans. Ultrason. Ferroelectr. Freq. Control* 51 (2004) 352-358.
- [33] X. Zhang, L. Zhao, *J. Mater.* 1 (2015) 92–105.
- [34] R.A. Kishore, S. Priya, *Materials* 11 (2018) 1433.
- [35] L. Fraas, L. Partain, *Solar cells and their applications*, John Wiley & Sons, U.S.A. (2010).
- [36] C. Ratsch, J.A. Venables, *J. Vac. Sci. Technol.* 21 (2016) S96–S109.

- [37] D. Das, R.N. Singh, *Int. Mater. Rev.* 52 (2007) 29–64.
- [38] R. Carel, C.V. Thompson, H.J. Frost, *Acta mater.* 44 (1996) 2479–2494.
- [39] R.K. Singha, S. Manna, R. Bar, S. Das, S.K. Ray, *Appl. Surf. Sci.* 407 (2017) 418–426.
- [40] C. Pan, Y. Shi, F. Hui, E. Grustan-Gutierrez, M. Lanza, *History and Status of the CAFM*, Wiley-VCH Verlag GmbH & Co. KGaA, Germany (2017).
- [41] I. Beinik, *Electrical characterization of semiconductor nanostructures by conductive probe based atomic force microscopy techniques*, Ph.D. thesis, University of Leoben, Austria (2011).
- [42] R.A. Oliver, *Rep. Prog. Phys.* 71 (2008) 076501.

Chapter-6

NANOCRYSTALLINE NICKEL OXIDE THIN FILMS: A p-TYPE THERMOELECTRIC MATERIAL WITH WIDE BANDGAP

Contents

- 6.1 Introduction
- 6.2 Fabrication of thin films
- 6.3 Results
- 6.4 Discussion
- 6.5 Conclusion

The strategy of nanostructuring for the concurrent enhancement of thermoelectric power factor and optical bandgap of NiO thin films is described in this chapter. It discusses the transformation of the energy band structure as a result of reduced particle size and its effect on the physical properties of the NiO thin films.

6.1 Introduction

The realization of transparent conducting thermoelectric materials opens new trends in transparent devices such as hybrid photovoltaic-thermoelectric power generators, energy harvesting smart window and thermal sensing and cooling of optoelectronic devices. Since most of the efficient thermoelectric materials are optically opaque due to narrow bandgap, the investigations on wide bandgap thermoelectric materials have promising opportunities in modern device industries. Apart from this, the p-n junction and p-n couple transparent devices warrant p-type transparent thermoelectric materials [1,2]. Even though few optically transparent thermoelectric materials have been reported recently, the studies on p-type transparent conducting thermoelectric materials are very limited. In addition to this, p-type thermoelectric materials usually exhibit high electrical resistivity due to low carrier concentration [3,4]. Hence, the realization of efficient transparent thermoelectric devices was greatly hindered by the low performance of p-type thermoelectric materials.

Nickel oxide has been considered as an interesting compound due to its p-type semiconducting property along with wide bandgap. Moreover, it is an earth abundant, non-toxic and low cost transition metal oxide with moderate electrical conductivity and high chemical stability. Nickel oxide crystallizes in the cubic rock salt structure of

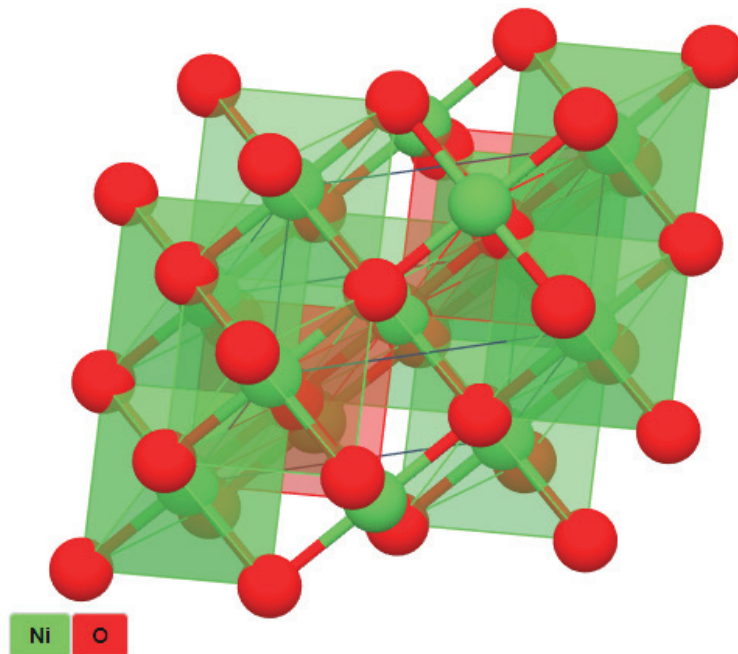


Figure 6.1 Crystal structure of NiO compound

NaCl with octahedral Ni^{2+} and O^{2-} sites as shown in fig. 6.1 [5]. It is a paramagnetic material with space group $Fm\bar{3}m$. It has one molecule per primitive cell and a lattice constant of 4.18 Å. At low temperatures, it transforms into slightly distorted rhombohedral structure with antiferromagnetic properties [6]. The melting point of NiO is 1955°C and has a refractive index of 2.18. It is a direct bandgap semiconductor with an energy bandgap of 3.5–4 eV. The stoichiometry of NiO usually deviates from 1:1 resulting in nitrogen sub-stoichiometric thin films. This can be attributed to the lowest formation energies of acceptor point defects. Hence, the physical properties of thin films associated with stoichiometry show wide variations [7,8]. According to various theoretical and experimental investigation reports, carrier concentration, electrical resistivity and Seebeck coefficient of NiO show large deviations with its various material aspects such as particle size, composition and defects. Hence, these material properties of NiO can be precisely tuned by controlling the growth parameters during the fabrication of thin films [3].

The transparency along with p-type conductivity makes the NiO thin films as an important material in the field of optoelectronics and photovoltaics. Moreover, when integrating these capabilities of NiO with its thermoelectric properties, it can be considered as potential candidate for the investigation of transparent thermoelectric materials. But, its application in transparent thermoelectric devices is limited due to very low power factor originated from high electrical resistivity. Since the charge carriers of intrinsic p-type semiconductors are usually generated by intrinsic point defects, the high electrical resistivity of NiO can be attributed to the low hole concentration. In addition to this, the very low thickness requirement for the high transparency of thin films is another source of high electrical resistivity [9,10]. The optimization of resistivity and Seebeck coefficient in order to get higher power factor along with increased bandgap can resolve these challenges. Even though the thin film deposition temperature is high, the crystallinity and the grain size of NiO are low due to high activation energy of its crystalline phases [11]. In this scenario, nanostructuring can be effectively employed in NiO thin films for the simultaneous enhancement of thermoelectric power factor and optical bandgap. The fabrication of NiO thin films having nanoparticles and the optimization of its size to transform the thin films as an efficient wide bandgap thermoelectric material is reported in this chapter.

6.2 Fabrication of nanocrystalline NiO thin films

The NiO thin films were deposited on quartz substrates with dimension 10x10x1 mm using reactive RF magnetron sputtering with a 99.99% pure nickel target of 50 mm in diameter and 3 mm thick. Before the deposition, the quartz substrates were cleaned by standard solution cleaning method followed by ultrasonic cleaning in acetone and finally dried in an oven. We carried out different analysis based on the various deposition parameters which determine the physical properties of the thin film. The effect of sputtering power and working pressure on structural and electrical properties of the NiO thin film was investigated. These studies provided a precise picture of the optimized sputtering parameters to deposit the NiO thin films for the investigation of p-type thermoelectric material with wide bandgap. Oxygen gas with 99.999% pure was used as both sputtering and reactive gas. The separation distance between the substrate and the target was fixed as 80 mm. The base pressure was about 6×10^{-6} mbar before the entry of oxygen gas into the chamber. For all the deposited films, sputtering power of 200W, the base pressure of 6×10^{-6} mbar, the working pressure of 3×10^{-2} mbar and thickness of 100 nm were kept constant while substrate temperature was set to different values. Table 6.1 shows the optimized deposition parameters for NiO reactive sputtering. The decrease in substrate temperature from 450°C to different values up to 50°C decreases the energy of adsorbed atoms obtained as surface energy. It greatly restricts the mobility of adatoms results in development of thin films with small crystallites and low crystallinity [12].

TABLE 6.1. Deposition parameters optimized for NiO reactive sputtering

Parameter	Specification
Fabrication Technique	Reactive RF magnetron sputtering
Target	99.99% pure Ni
Substrate	Quartz with 99.99% pure and 10x10x1mm size
Plasma	99.999% pure Oxygen
Target-Substrate Distance	8 cm
Sputtering Power	200 W
Substrate Temperature	50 – 450°C
Ultimate Vacuum	6×10^{-6} mbar
Working Pressure	3×10^{-2} mbar
Film Thickness	~100 nm

6.3 Results

6.3.1 Phase and crystallographic features

The phase and crystallographic features of nanocrystalline thin films of NiO deposited at different substrate temperature were investigated by X-ray diffraction analysis. The X-ray diffractograms with ICDD data (ICDD No. 00-004-0835) are shown in fig. 6.2. It is shown that the thin films were polycrystalline and all the peaks were indexed with the cubic phase of NiO with space group $Fm\bar{3}m$. The major XRD peaks were observed with diffractions of (111) and (200) planes. The decrease in total intensity and increase in full width at half maximum of the reflections from all planes with decreasing substrate temperature ensure the decrease in crystallinity and crystallite size respectively.

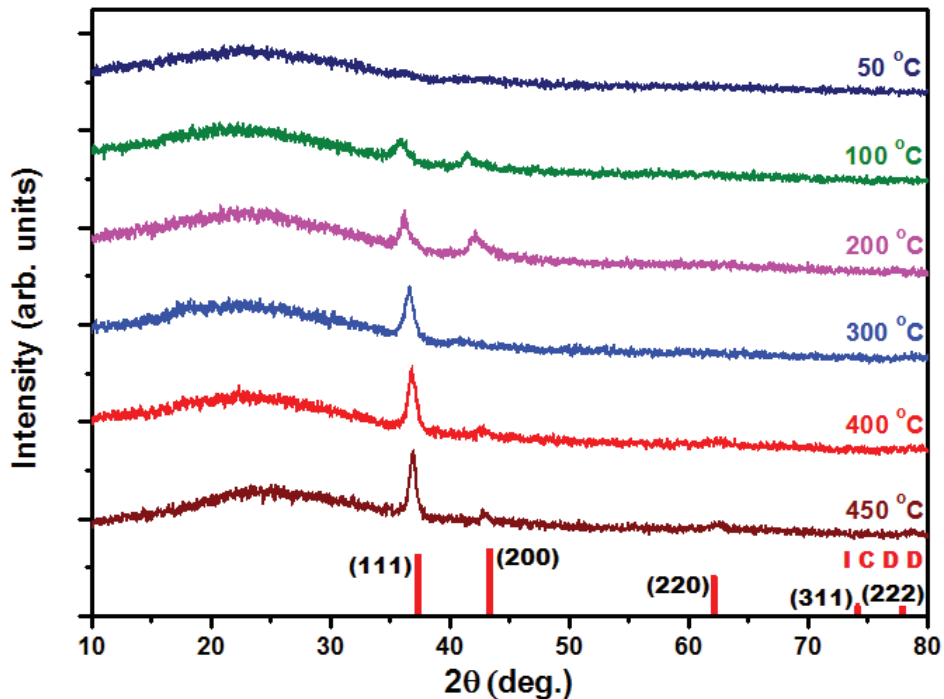


FIGURE 6.2. XRD of nanocrystalline NiO thin films sputtered at different substrate temperature

6.3.2 Thickness

The thickness of the NiO thin films was estimated by analysing the surface topography of the partially coated samples using AFM. AFM measures the height of the step which is created by partially covering the surface of the quartz substrate by kapton tape as shown in fig. 6.3. The estimated thickness of all the sputtered thin films is ~ 100 nm.

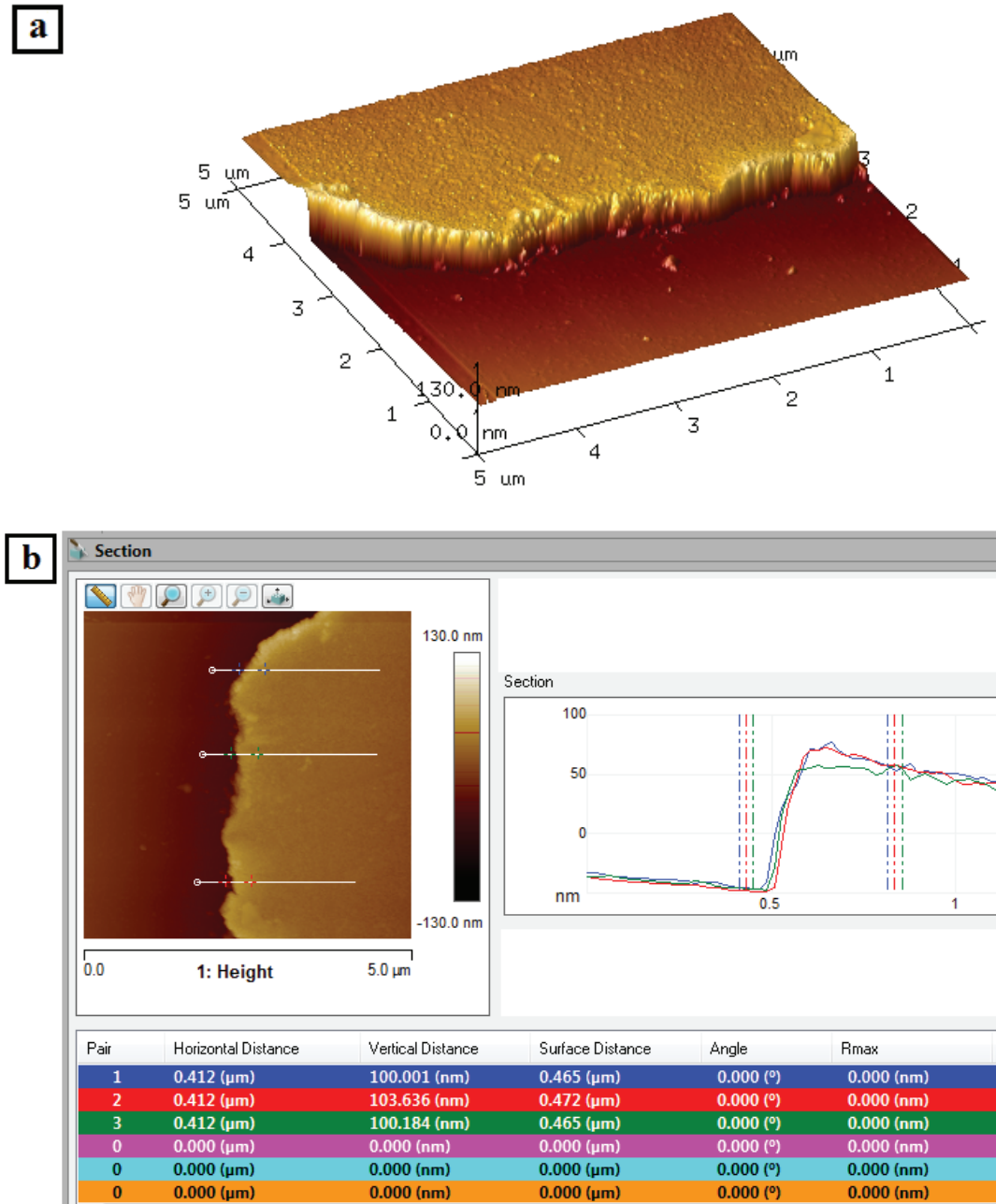


FIGURE 6.3. (a) Surface topography and (b) step parameters of partially coated NiO thin film

6.3.3 Surface features

The formation of nanostructured thin films on the surface of substrates normally adopts the techniques such as self assembly or diffusion limited aggregation. The growth process in these techniques is originated by the balancing of the mobility characteristics and the corresponding lateral interactions. The surface mobility of adsorbed particles comprises thermal and chemical potential driven transport features.

Since both factors are strongly influenced by temperature, the higher the temperature, the more active the adsorbate motion and faster the gradient decay. In this situation, the effect of energetically favorable adsorption sites on the substrate and growing film surface is very small. Hence, substrate temperature during the deposition of thin film has remarkable influence on nucleation and growth of crystallites [13].

The surface features of the deposited NiO thin films were investigated by atomic force microscopy in tapping mode. The scan was performed on area of $2 \times 2 \mu\text{m}$ with 256×256 pixel resolution. The 3D and 2D images of the topographic features of NiO thin films with varying substrate temperature are shown in fig. 6.4. The reduction in particle size and small increase in surface roughness with decrease in substrate temperature are clearly observable from these profiles. It can be elucidated by analysing the surface grain distribution maps and corresponding length and volume histograms which are shown in fig. 6.5. At higher substrate temperatures, the grain density is low and the grain size is large. The size of the grains is mostly in between 40-80 nm for the thin films sputtered at substrate temperature of 450°C and 400°C . At higher substrate temperatures, the particles condensed on the surface have enough energy to overcome the energy barrier of the nucleation sites and inter grain migration of the particles are predominated. It reduces the embryo nuclei density and aids the growth of the crystallites, hence the number of grains is decreased and size of the grains is increased [14]. When the substrate temperature decreases to lower values, the thermal energy supplement from the substrate to the adatoms is low results in weak surface diffusion. The migration of adatoms between the grains is hindered due to inefficiency to overcome the energy barrier. The adsorbed particles lie on the adsorption sites as a consequence of the significant reduction in the surface mobility. It increases the nucleation density and prevents the growth of the crystallites [15]. Hence, the NiO thin films fabricated at lower substrate temperatures consist of large number of nanocrystalline particles having the size below 20 nm. Also, the resistivity of these thin films will be high due to the presence of large number of voided intercrystalline boundaries. All the thin films show very low surface roughness and it increases with decreasing substrate temperature due to the increase in particle density and grain boundaries.

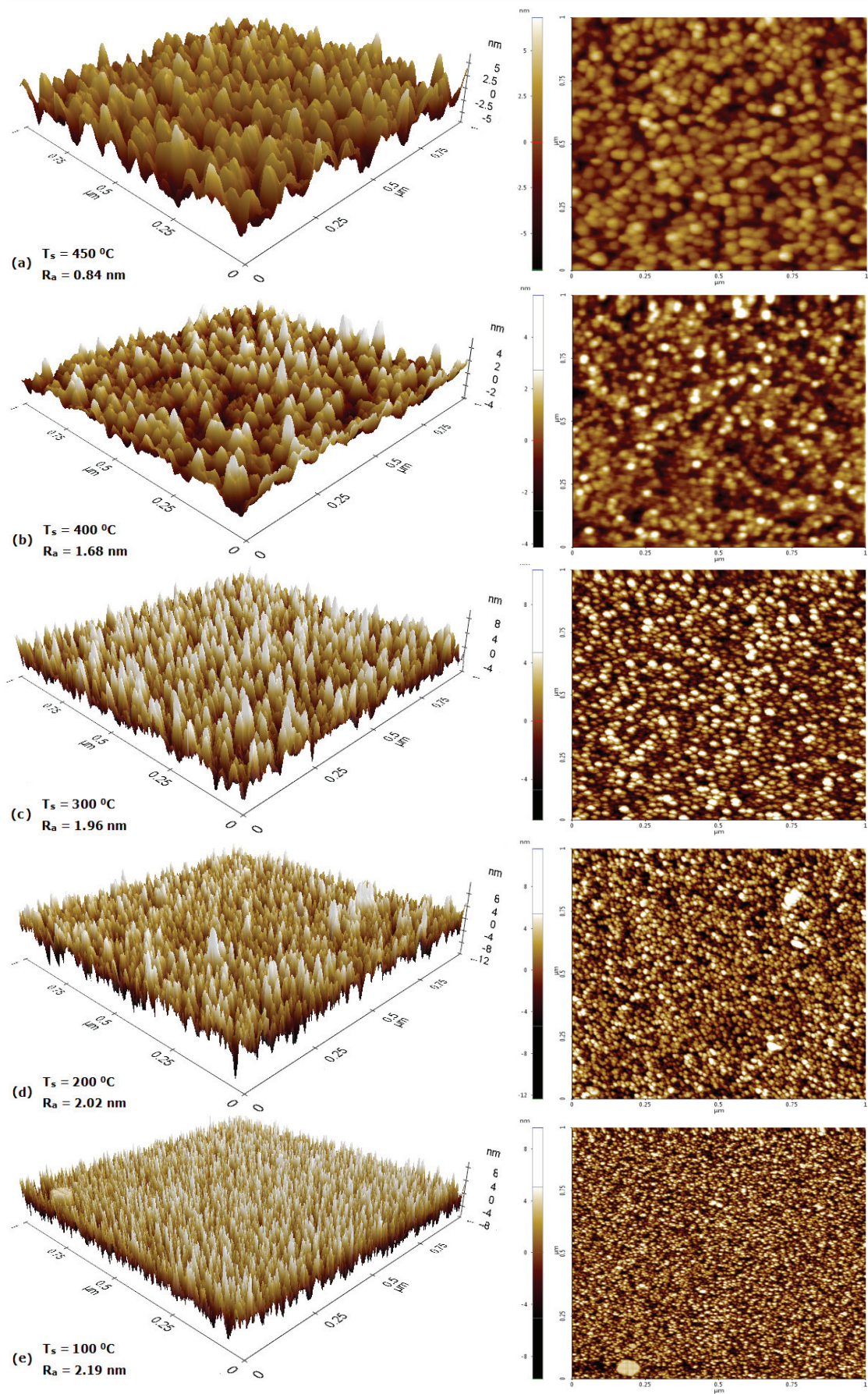
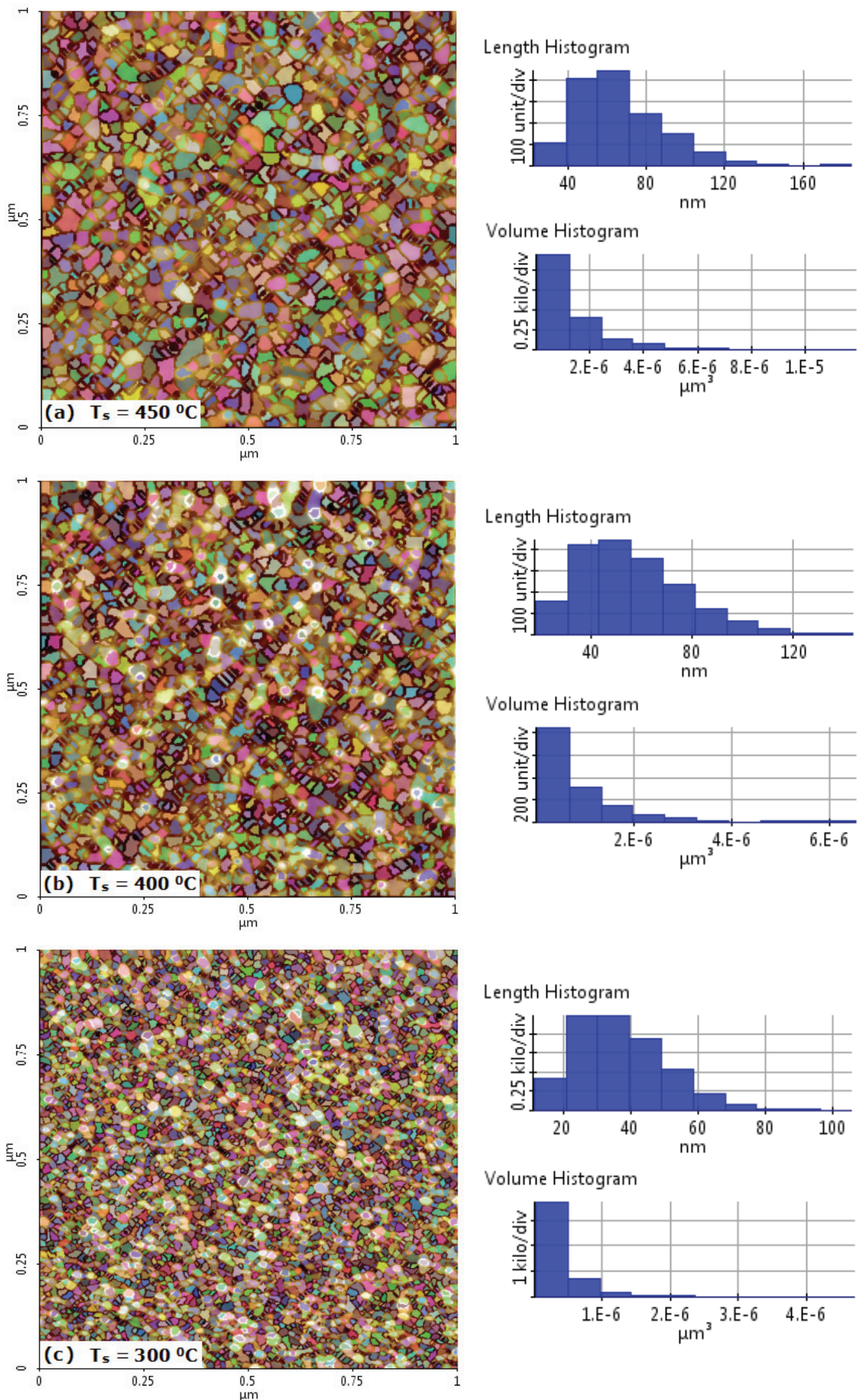


FIGURE 6.4. AFM 3D with average surface roughness (left) and 2D (right) topography of NiO thin films sputtered with different substrate temperature



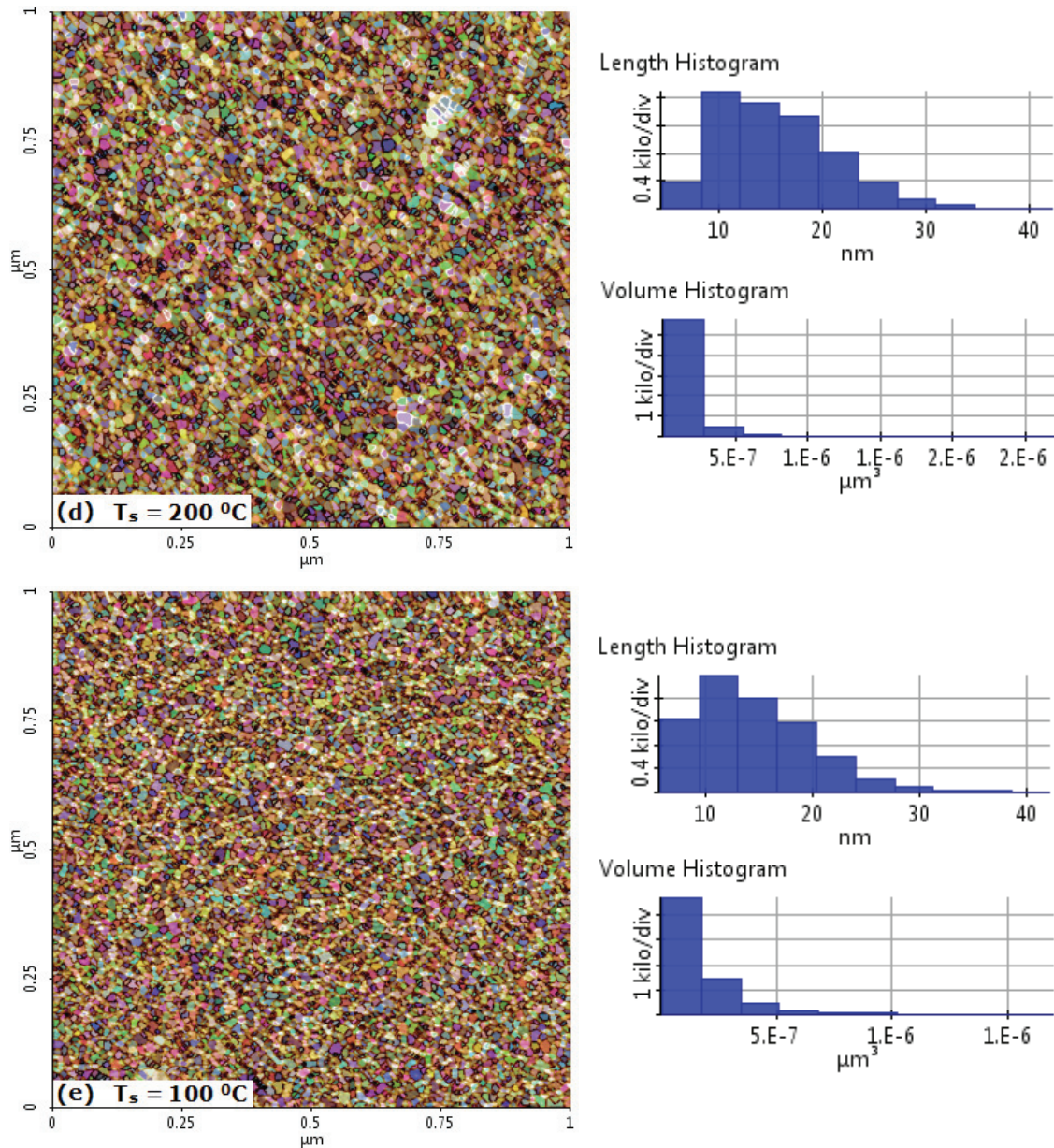


FIGURE 6.5. AFM 2D grain distribution (left) and grain length and volume histograms (right) of NiO thin films sputtered with different substrate temperature

6.3.4 Thermoelectric properties

The Seebeck coefficient and electrical conductivity determine the thermoelectric power factor of the thin films. The conductivity (σ) is the reciprocal of resistivity (ρ) and can be determined by the relation, $\sigma = (1/\rho)$. The temperature depended thermoelectric properties of the prepared NiO thin films from RT to $400\text{ }^\circ\text{C}$ are shown in fig. 6.6. The resistivity and Seebeck coefficient increase with decreasing substrate temperature. The rate of variation of these parameters is almost constant up

to the substrate temperature of 300°C and at 200°C, it exhibits remarkable increase. The resultant of the variations in resistivity and Seebeck coefficient increases the power factor. The positive Seebeck coefficient indicates that all the prepared NiO thin films have p-type conductivity, hence holes are the majority carriers in thermoelectric transport.

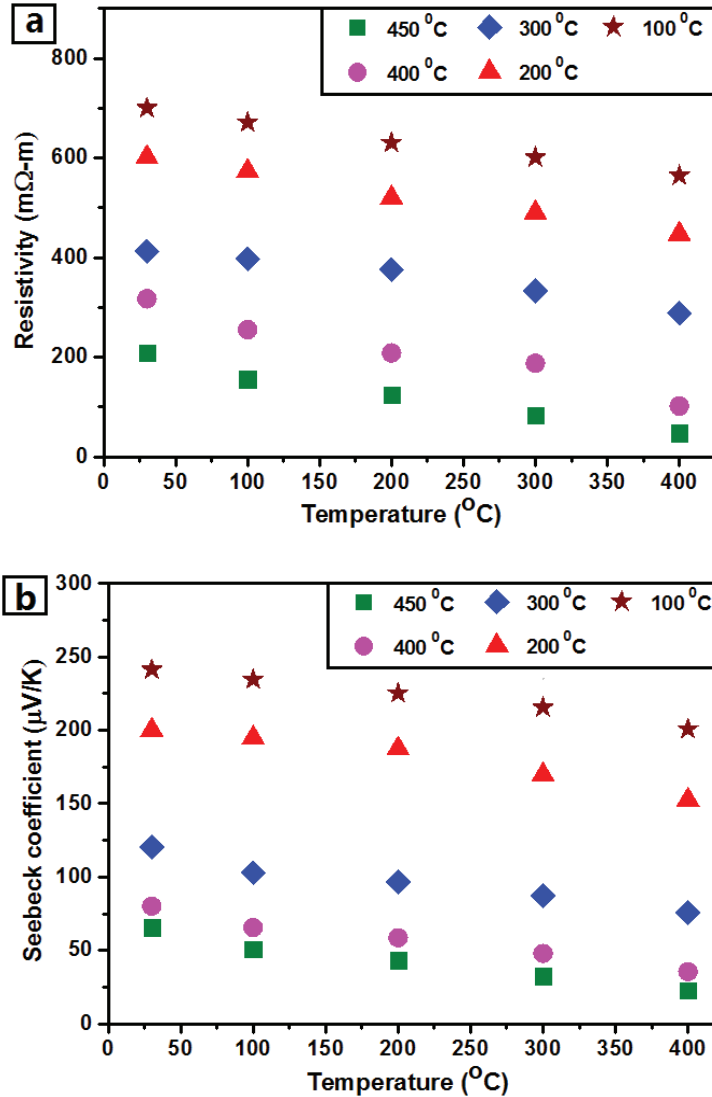


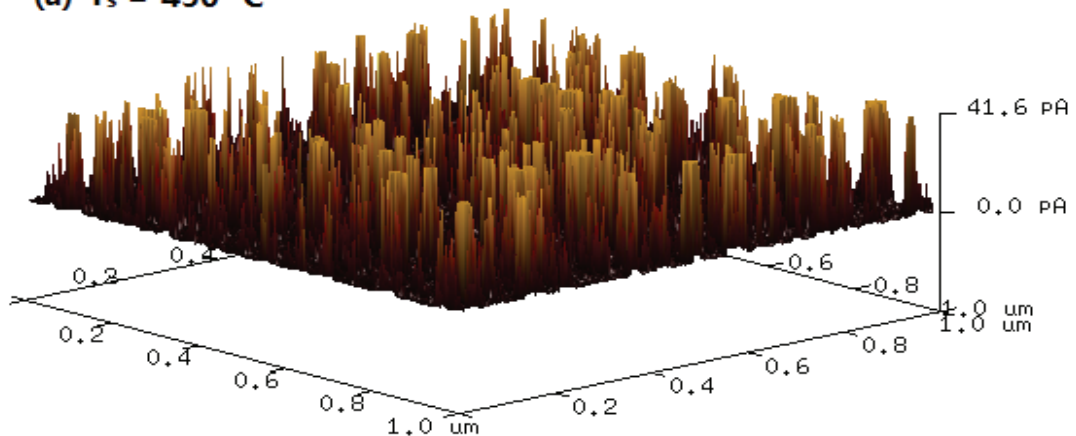
FIGURE 6.6. Temperature dependent (a) resistivity and (b) Seebeck coefficient of NiO thin films sputtered with different substrate temperature

6.3.5 Surface charge distribution

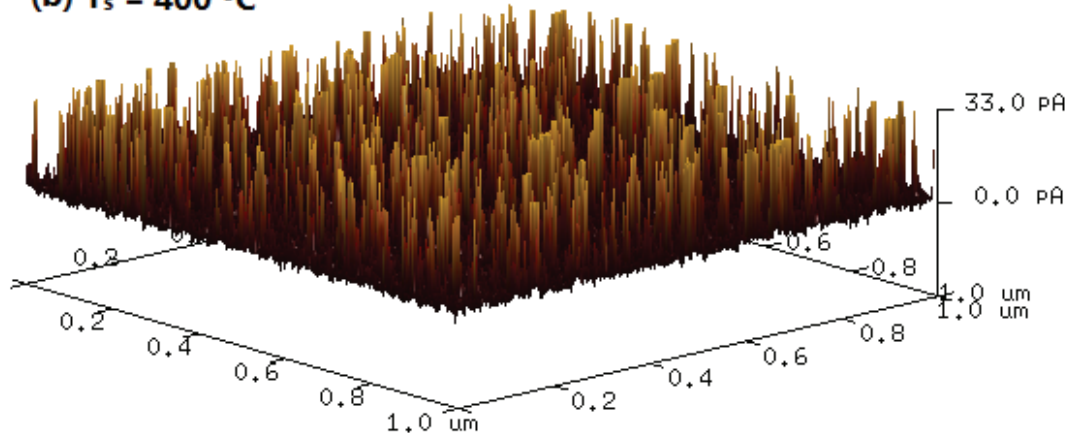
In thin films, the surface charge density has considerable role in the total conductivity of the material. The charge carrier density on the surface of the NiO thin films were mapped by conductive atomic force microscopy (CAFM). The intensity of the charge distribution at a bias voltage of 0V is depicted in fig. 6.7. The strength of

the current distribution decreases with the decreasing substrate temperature which is directly related to the resistivity that obtained from the thermoelectric characterization. The current flowing through the surface particles is positive for all the prepared NiO thin films. Since the current flowing from sample to probe is considered as positive by convention, the positive current detected by the probe tip which is shown as upward in 3D images ensures that positive charges are stored within the particles and the thin film having p-type conductivity [16,17]. These factors have already been obtained from Seebeck coefficient.

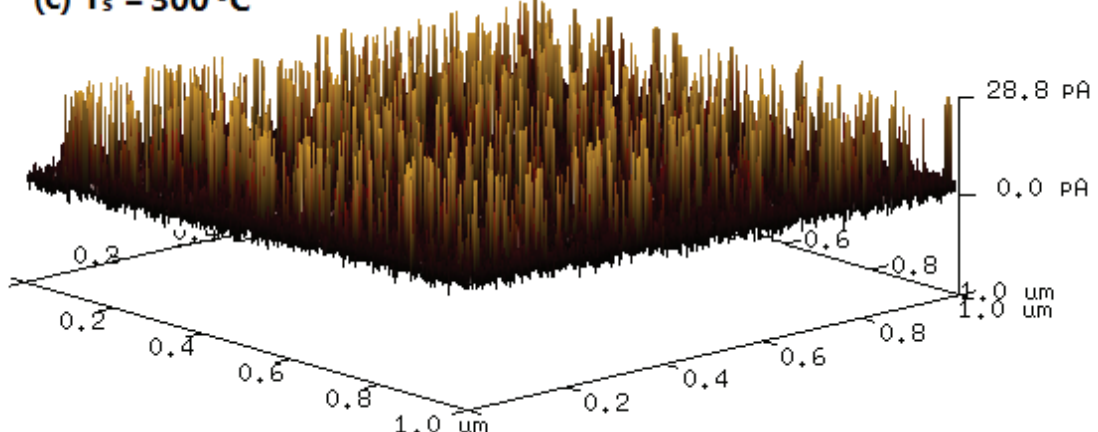
(a) $T_s = 450\text{ }^\circ\text{C}$



(b) $T_s = 400\text{ }^\circ\text{C}$



(c) $T_s = 300\text{ }^\circ\text{C}$



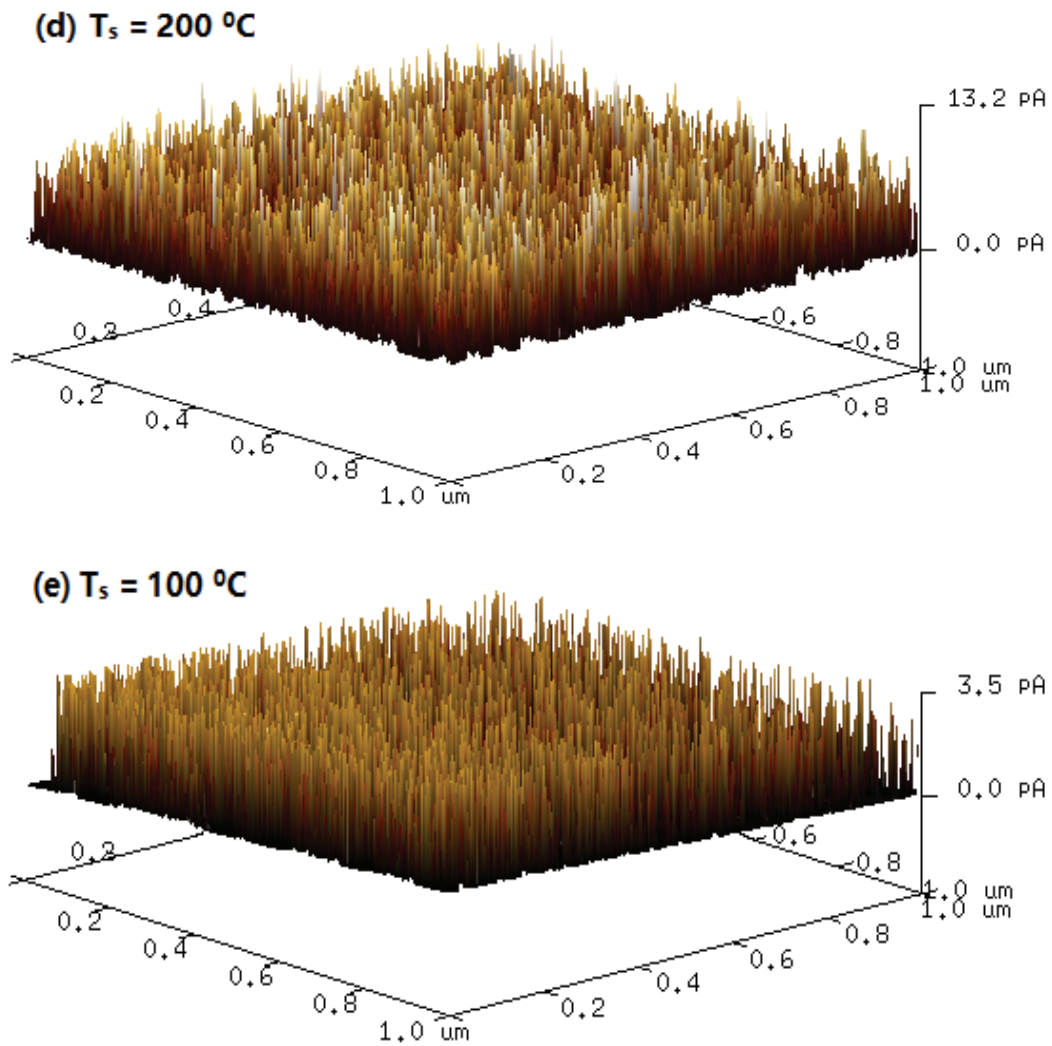


FIGURE 6.7. CAFM 3D current distribution profile of NiO thin films sputtered with different substrate temperature

6.3.6 Optical properties

The spectral distributions of transmission (%T) and reflection (%R) of NiO thin films are shown in fig. 6.8. As substrate temperature decreases, the transmittance decreases and reflectance has small variations. The bandgap of the thin films is estimated by Tauc's relationship for the direct transition semiconductors. The thin films sputtered at lowest substrate temperatures exhibit significant enhancement in bandgap as shown in fig. 6.10. Since the absorptance of the thin films sputtered at 200°C and 100°C show sharp increment, the reduction in transmittance of these thin films can be attributed to the resultant of the variations in absorptance and reflectance.

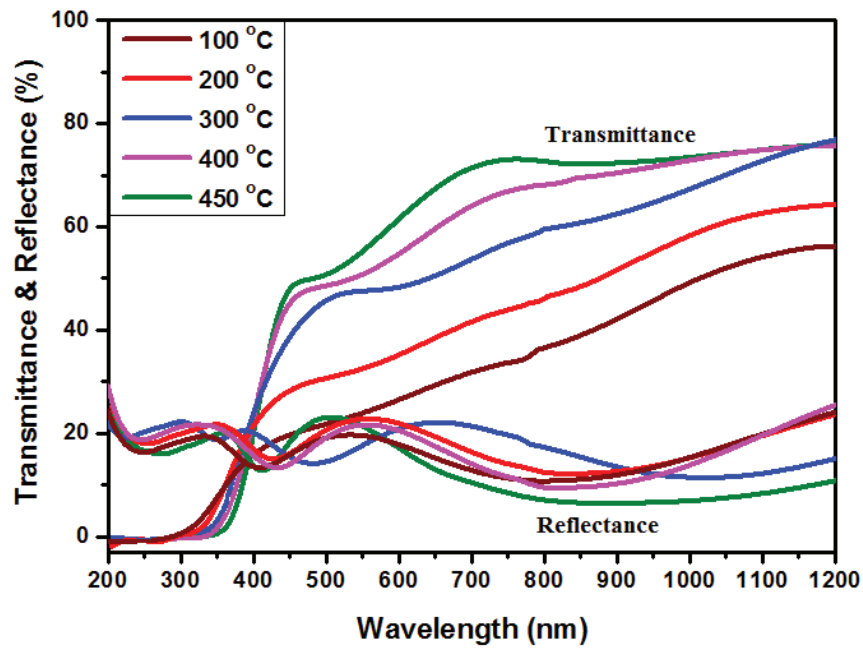


FIGURE 6.8. Transmittance and reflectance of spectra as functions of wavelength of NiO thin films sputtered with different substrate temperature

6.4 Discussion

The preparation of thin films having nanostructured morphologies has been considered as an efficient approach to enhance the thermoelectric properties of the materials. This strategy was adopted to realize simultaneous enhancement in thermoelectric power factor and optical bandgap of NiO thin films. The reduction of substrate temperature during the fabrication of thin films gradually improved the power factor and widened the optical bandgap as shown in fig. 6.9 and fig. 6.10 respectively.

The thin films sputtered at 200⁰C and 100⁰C exhibit remarkable enhancement in power factor and bandgap. At lowest substrate temperatures, the growth of the crystallites are limited due to low surface diffusion of adatoms as discussed in AFM analysis and nanocrystalline thin films are formed. When the size of the particles approaches to the de Broglie wavelength of electrons of the material, the holes are confined inside the space of the particles. The consequence of this confinement in space is the quantization of their energy and momentum. It is known as quantum confinement effect [18]. It can be modelled by the motion of a particle in a potential

well with infinite walls. Hence, the confined holes in the valence band can be considered as, it is in an inverted potential well with infinite wall with the maximum

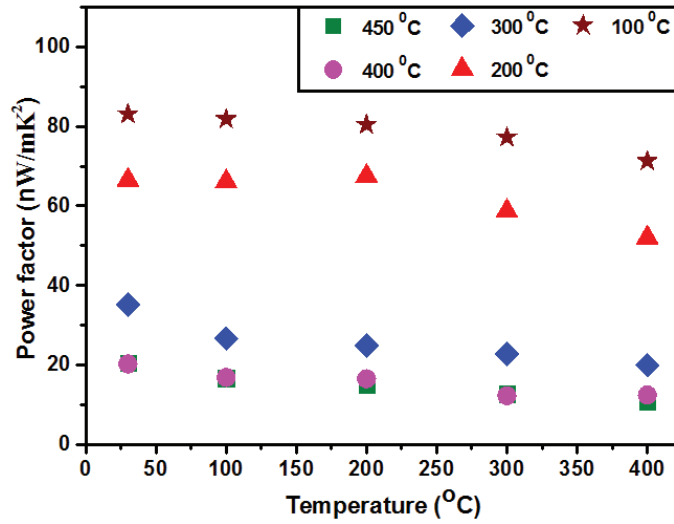


FIGURE 6.9. Temperature dependent power factor of NiO thin films

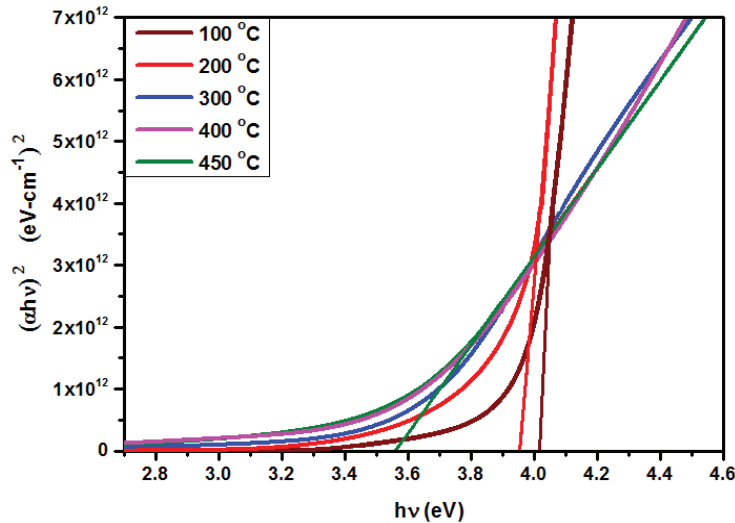


FIGURE 6.10. The variation of bandgap of NiO thin films with substrate temperature

energy level is that of the valence band. The quantum confinement alters the atomic structure of the material leading to the transition of energy levels from continuous to discrete [19,20]. The energy levels below the valence band are given by

$$E_n = \frac{h^2 n^2}{8 m_h^* d^2} \dots\dots\dots (6.1)$$

where h is the Planck's constant, n is the quantum number for the valence states, it can take the values 1, 2, 3, and so on, m_h^* is the effective mass of holes and d is the diameter of the particle. Since these holes having the specific energies can still free to move in the directions parallel to the layers in quantum well, the corresponding density of states, $g(E)$ becomes constant with energy for each sub bands. Hence the density of states with energy takes a step like feature having sharp variations [21].

According to the Mott expression [22],

$$S = \frac{\pi^2 k_B^2 T}{3 q} \left[\frac{1}{n(E)} \frac{dn(E)}{dE} + \frac{1}{\mu(E)} \frac{d\mu(E)}{dE} \right] \dots\dots\dots (6.2)$$

where k_B is the Boltzmann constant, T is the temperature, q is the carrier charge, $n(E)$ is the carrier density at energy level E , $\mu(E)$ is the mobility, an increased energy dependence of $n(E)$ or an increased energy dependence of $\mu(E)$ can enhance the Seebeck coefficient. Since the $n(E)=g(E)f(E)$, where $f(E)$ is Fermi function, increasing the dependence of the density of states on energy, $dg(E)/d(E)$ enhances the $dn(E)/d(E)$.

The step like feature of density of states having sharp variations with energy as a consequence of quantum confinement effect significantly improves its energy dependence [23]. Thus, the nanostructured NiO thin films sputtered at lower substrate temperatures exhibited remarkable enhancement in Seebeck coefficient. During the formation of nanocrystallites in NiO thin films, the grain boundary density increases with decreasing crystallite size and the crystallinity decreases due to the reduction in substrate temperature. Since these variations enhance the scattering of the charge carriers, the resistivity of the NiO thin films increases with the decreasing particle size. However the resultant of the variations in Seebeck coefficient and electrical resistivity significantly enhanced the power factor to 83 nW/m K^2 with Seebeck coefficient of $241 \text{ } \mu\text{V/K}$ and resistivity of $700 \text{ m}\Omega \text{ m}$ at RT. When considering the equation 6.1 and the same for the conduction band, the highest valence band and lowest conduction band energy levels change significantly with the diameter of the particle resulting in a size dependent tunable bandgap. Hence the reduction in the size of the particles causes the widening of the bandgap of the thin films. The NiO thin film having smallest nanoparticles sputtered at a substrate temperature of 100°C

exhibited a bandgap of 4.02 eV which has a blue shift of 0.46 eV from the bandgap of the thin film having larger particles.

6.5 Conclusion

The realization of transparent thermoelectric material based hybrid devices requires efficient p-type thermoelectric materials with wide bandgap. The concurrent enhancement in thermoelectric power factor and bandgap of NiO thin films was achieved by quantum confinement effect. The thin films of NiO particles were successfully fabricated by reactive radio frequency magnetron sputtering. The size of the nanoparticles was decreased by reducing the substrate temperature during the deposition of thin films. The quantum confinement effect originated from the reduced particle size transformed the variation of density of states with energy as a step like feature having sharp variations. It improved the density of states energy dependence and hence enhanced the Seebeck coefficient. The nanostructured NiO thin films exhibited a four-fold enhancement in thermoelectric power factor as compared with that having larger crystallites. It attained a power factor to 83 nW/m K^2 with Seebeck coefficient of $241 \text{ } \mu\text{V/K}$ and resistivity of $700 \text{ m}\Omega \text{ m}$ at RT. Moreover, the quantum confinement blue shifted the optical band gap of NiO from 3.56 to 4.02 eV. Hence, various aspects of the nanostructuring strategy can be effectively employed to tune the properties of the thin films for hybrid device applications.

References

- [1] X. Wang, A. Suwardi, S.L. Lim, F. Wei, J. Xu, *npj Flex. Electron.* 19 (2020) 1–9.
- [2] M. Ferreira, J. Loureiro, A. Nogueira, A. Rodrigues, R. Martins, I. Ferreira, *Mater. Today Proc.* 2 (2015) 647–653.
- [3] J. Linnera, G. Sansone, L. Maschio, A.J. Karttunen, *J. Phys. Chem. C* 122 (2018) 15180-15189.
- [4] K.O. Ukoba, A.C. E. Eboka, F.L. Inambao, *Renew. Sustain. Energy Rev.* 82 (2018) 2900–2915.
- [5] <https://materialsproject.org/materials/mp-19009/>.
- [6] J.E. Keem, J.M. Honig, Selected electrical and thermal properties of undoped

- nickel oxide, U.S. Department of Defense U.S.A. (1978).
- [7] S. Lany, J. Osorio-guillén, A. Zunger, *Phys. Rev. B* 75 (2007) 241203.
- [8] J. Osorio-guillén, S. Lany, A. Zunger, *AIP Conf. Proc.* 1199, (2010) 128-129.
- [9] H. Sun, S. Chen, W. Peng, C. Wen, X. Wang, T. Chuang, *Coatings* 8 (2018) 168.
- [10] F. Hajakbari, S. Rashvand, A. Hojabri, *J. Theor. Appl. Phys.* 13 (2019) 365-373.
- [11] I. Petrov, P.B. Barna, L. Hultman, J.E. Greene, *J. Vac. Sci. Technol. A* 21 (2003) S117–S128.
- [12] E. Alfonso, J. Olaya, and G. Cubillos, *Crystallization-Science and technology: Thin film growth through sputtering technique and its applications*, IntechOpen (2011) 397-432.
- [13] P.B. Barna, M. Adamik, *Thin Solid Films* 317 (1998) 27–33.
- [14] T. Karabacak, *J. Nanophotonics* 5 (2011) 1–18.
- [15] R.F. Bunshah, *Handbook of deposition technologies for films and coatings*, Elsevier, U.S.A. (1994).
- [16] R.A. Oliver, *Rep. Prog. Phys.* 71 (2008) 076501.
- [17] I. Beinik, *Electrical characterization of semiconductor nanostructures by conductive probe based atomic force microscopy techniques*, Ph.D. thesis, University of Leoben, Austria (2011).
- [18] P.M. V Raja, A.R. Barron, *Physical methods in chemistry and nano science*, Rice University, U.S.A. (2020).
- [19] A.I. Onyia, H.I. Ikeri, A.N. Nwobodo, *J. Ovonic Res.* 14 (2018) 49–54.
- [20] G. Ramalingam, P. Kathirgamanathan, G. Ravi, T. Elangovan, B.A. Kumar, N. Manivannan, K. Kasinathan, *Quantum Dots-Fundamental and Applications: Quantum confinement effect of 2D nanomaterials*, IntechOpen (2020) 1-12.
- [21] D.A.B. Miller, *Quantum dynamics of simple systems: Optical physics of quantum wells*, Institute of Physics, London (1996).
- [22] J.P. Heremans, B. Wiendlocha, A.M. Chamoire, *Energy Environ. Sci.* 5 (2012) 5510–5530.
- [23] J. He, T.M. Tritt, *Science* 357 (2017) 1-10.

THIN FILM THERMOELECTRIC GENERATORS

Contents

- 7.1 Introduction
- 7.2 Fabrication and Characterizations
- 7.3 Results and discussion
- 7.4 Conclusion

This chapter describes the fabrication and electrical characterizations of the thermoelectric generators made up of different couples of the thin film leg materials which have been already discussed in the previous chapters. The evaluation of open circuit voltage, short circuit current, output power and maximum operating power to validate the thermoelectric properties of the thin films and the energy conversion capability of the devices are briefly discussed.

7.1 Introduction

Thermoelectric generator (TEG) is a solid state device that converts waste heat into electrical power by Seebeck effect. It is a very reliable power generation technique due to its solid state nature. The absence of moving parts makes it as silent, light weight, long lifetime and low maintenance device. It is environmental friendly as well as reduces the environmental pollution by using waste heat as input power. The TEGs can find out the input power from any scenario which produces waste heat. Since the output power spans from very low to high values, the TEGs can be utilized in wide applications, from wrist watches to satellites [1,2].

The thermoelectric properties of Sn_3N_4 and ZnSnN_2 as n-type and CrN and NiO as p-type thin film materials were investigated and discussed in previous chapters. The thermoelectric properties of the each material were investigated by estimating the power factor from electrical resistivity and Seebeck coefficient. The thermoelectric generator is constructed by alternatively attaching n-type and p-type semiconductor materials that are electrically connected in series and thermally in parallel [3]. Hence, the output power of the TEG is greatly depends on the figure of merit of the individual materials. The thermoelectric measurement of the individual materials was performed in helium atmosphere by using highly sophisticated thermoelectric measurement system. But, the working environment of TEGs is entirely different from that of measuring conditions. In addition to this, the individual materials are subjected to temperature mismatch due to operating conditions. These factors will greatly affect the output power of TEG. Hence, to ensure the energy conversion performance of these thin films in a device form, the electrical characterizations of TEGs made up of different couples of the materials are necessary [4].

7.2 Fabrication and characterization of thin film thermoelectric generators

The four TEGs of different couples of the thin film materials, (1) $\text{Sn}_3\text{N}_4/\text{CrN}$, (2) $\text{Sn}_3\text{N}_4/\text{NiO}$, (3) $\text{ZnSnN}_2/\text{CrN}$ and (4) $\text{ZnSnN}_2/\text{NiO}$ were fabricated by radio frequency magnetron sputtering. The thin film of each material for TEGs was selected based on the highest power factor obtained from the thermoelectric characterizations.

The fabricated TEGs consist of two couples of thermoelectric legs. The appropriate masking of the substrates by kapton tape was employed to deposit the individual leg materials. These individual legs are electrically connected in series by using silver contacts and thermally in parallel. The schematic representation of prototype thin film TEG is shown in fig. 7.1. The sputtering parameters of each n- and p-type thin films for the fabrication of TEGs are given in table 7.1.

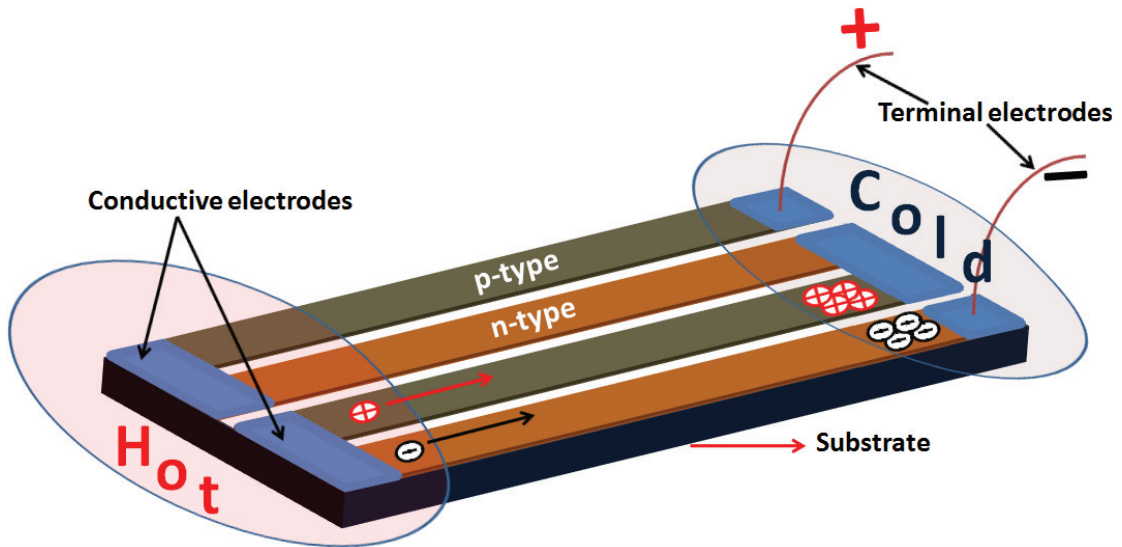


FIGURE 7.1. The schematic representation of prototype thin film thermoelectric generator

TABLE 7.1. The sputtering parameters of p-type and n-type thin films as thermoelectric legs for the fabrication of TEGs

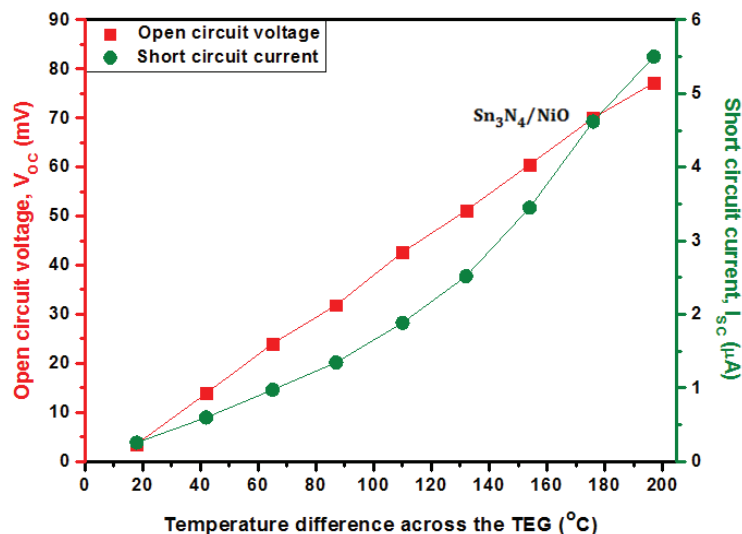
Thin film	Sputtering & reactive gas	Working pressure (mbar)	Reactive gas partial pressure (mbar)	Substrate temperature ($^{\circ}\text{C}$)	Power (W)
Sn₃N₄ (n-type)	Nitrogen	4×10^{-3}	4×10^{-3}	250	150
ZnSnN₂ (n-type)	Nitrogen + Argon	3×10^{-2}	1×10^{-2}	300	150
CrN (p-type)	Nitrogen	4×10^{-2}	4×10^{-2}	400	200
NiO (p-type)	Oxygen	3×10^{-2}	3×10^{-2}	100	200

The power output performance of the TEGs was evaluated by analyzing the temperature gradient v/s current, voltage and power (ΔT -V, I and P) characteristics [5]. The temperature difference was created by varying the hot side temperature from 50-250⁰C while maintaining the cold side at room temperature. The device operating voltage and operating power (P_{MAX}) as a function of electrical current (I-V and P) at matched load were estimated by varying the external load resistance [6]. These characterizations were performed by a customized instrumental setup. It continuously senses the temperatures by thermocouples and it can be monitored by the temperature display system. The measurement leads are connected to multimeter by spring loaded copper probes to estimate the voltages and currents. The details of the measuring setup were described in chapter-2 under ‘thermoelectric generator characteristics’.

7.3 Results and discussion

7.3.1 Electrical characteristics with temperature gradient

The TEGs of different couples of the thin films as leg materials, $\text{Sn}_3\text{N}_4/\text{CrN}$, $\text{Sn}_3\text{N}_4/\text{NiO}$, $\text{ZnSnN}_2/\text{CrN}$ and $\text{ZnSnN}_2/\text{NiO}$ were fabricated for the evaluation of the electrical characteristics. The open circuit voltage (V_{OC}) and short circuit current (I_{SC}) generated from the devices were investigated by varying the temperature difference across the TEGs as shown in fig. 7.2. The temperature gradient was created by gradually increasing the temperature of the hot side while the cold side kept constant by ambient air. The fig. 7.3 exhibits the increase in output power (P_{OUT}) with temperature difference estimated from the output voltage and current.



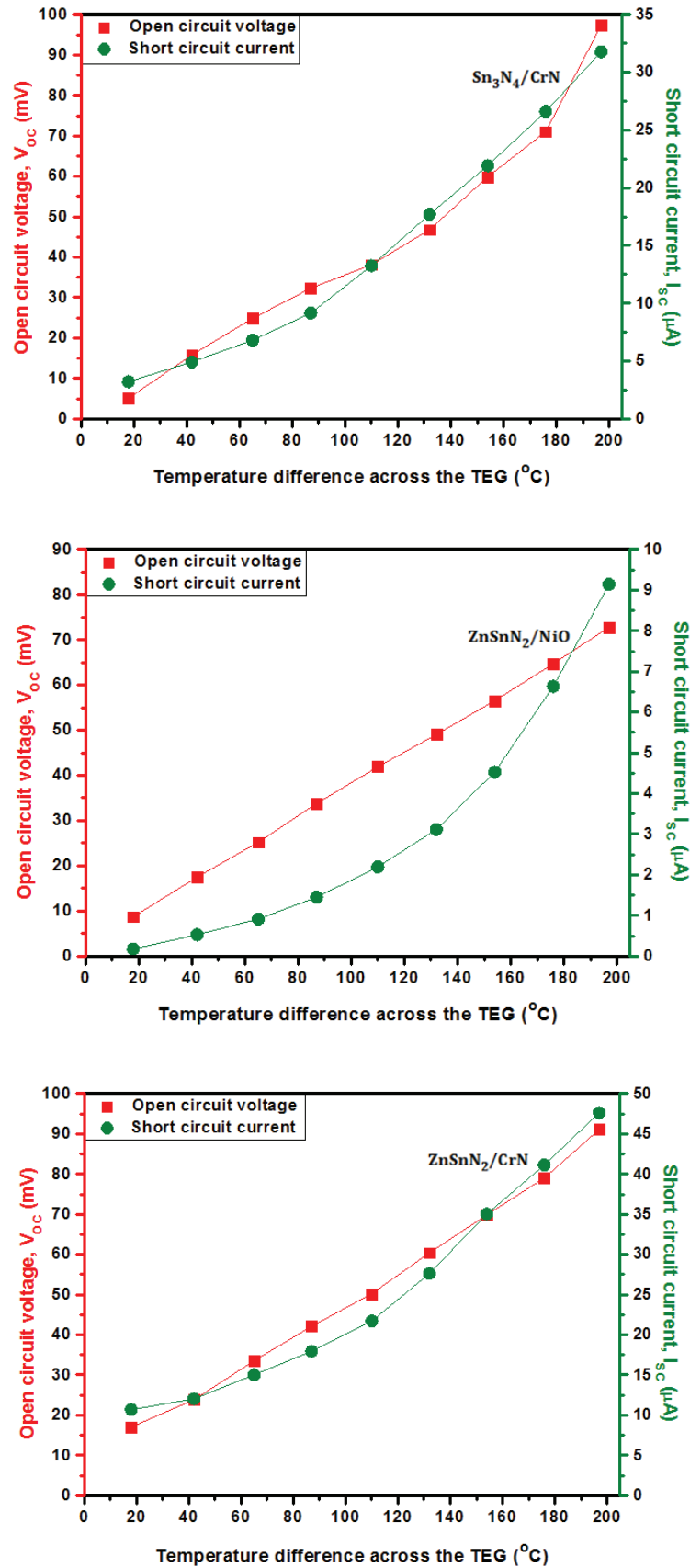


FIGURE 7.2. The variation of open circuit voltage and short circuit current with temperature gradient of TEGs

The V_{OC} is proportional to the Seebeck coefficient, which increases with the operating temperature and temperature difference [7]. This trend is seen in the characteristics of all TEGs. The increase in operating temperature decreases the internal resistance of the devices and hence the I_{SC} increases. The output power of the devices clearly reflects the variations of V_{OC} and I_{SC} generated in the TEGs. The maximum V_{OC} , I_{SC} and P_{OUT} at a temperature gradient of 200°C are given in Table 7.2. The maximum value of V_{OC} is depends on the Seebeck coefficient of the individual n- and p-type materials used for the fabrication of each TEGs. The $\text{Sn}_3\text{N}_4/\text{CrN}$ device shows the highest V_{OC} of 97 mV.

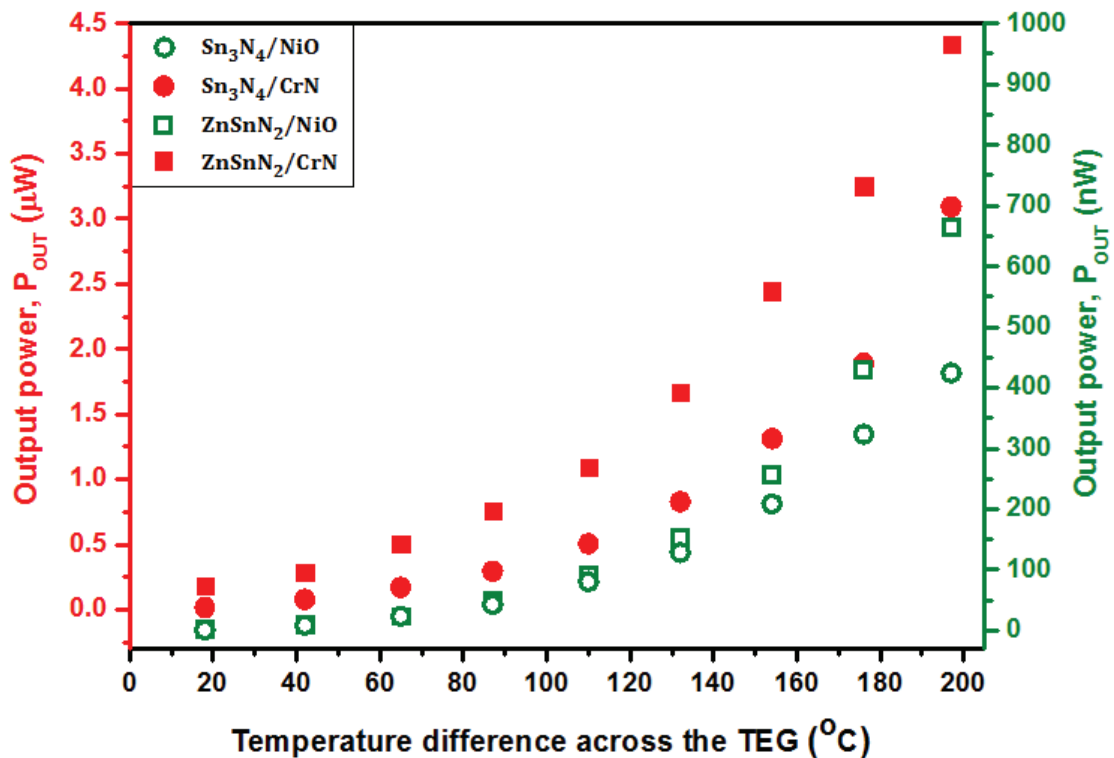


FIGURE 7.3. The variation of output power of TEGs with temperature gradient

The maximum value of I_{SC} greatly influenced by the internal resistance of the device which is the resistivity of the individual material and $\text{ZnSnN}_2/\text{CrN}$ device shows the highest value of $47 \mu\text{A}$. The larger currents through the device would results in higher P_{OUT} [8]. Hence, the highest P_{OUT} of $4.3 \mu\text{W}$ is also shown by the $\text{ZnSnN}_2/\text{CrN}$. Thus, the resistivity of the thermoelectric material has great importance in the P_{OUT} of TEGs.

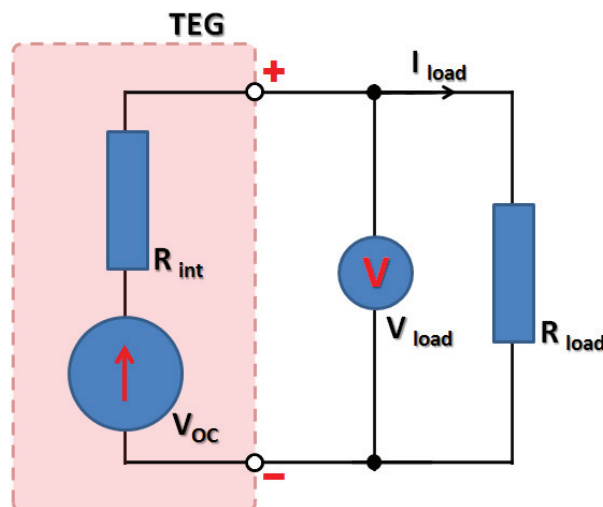
TABLE 7.2. The maximum V_{OC} , I_{SC} , P_{OUT} and P_{MAX} of TEGs at a temperature gradient of 200°C

TEG	Open circuit voltage	Short circuit current	Output power	Operating power
	V_{OC}	I_{SC}	P_{OUT}	P_{MAX}
	(mV)	(μA)	(μW)	(μW)
Sn ₃ N ₄ /NiO	77	5.5	0.42	0.10
Sn ₃ N ₄ /CrN	97	32.0	3.14	0.70
ZnSnN ₂ /NiO	72	9.0	0.66	0.16
ZnSnN ₂ /CrN	91	47.0	4.31	1.09

7.3.2 Electrical characteristics with load resistance

The TEG having direct current output can be considered as a voltage source with a source resistance and the electrical equivalent circuit is shown in fig. 7.4. The operating voltage when a load resistance is connected at the output terminal of the TEG can be determined as:

$$V_{load} = \frac{V_{OC} \cdot R_{load}}{R_{int} + R_{load}} \quad \dots\dots\dots (7.1)$$

**FIGURE 7.4.** The electrical equivalent circuit of a TEG

and the operating current is:

$$I_{load} = \frac{V_{OC}}{R_{int} + R_{load}} \dots\dots\dots (7.2)$$

The output circuit current reaches maximum when the load resistance is zero, that is the short circuited condition and the current is known as short circuit current (I_{SC}) [8].

The operating power that can be utilized by the external load is [9]:

$$P_{load} = V_{load} \cdot I_{load} = \frac{V^2_{OC}}{(R_{int} + R_{load})^2} R_{load} \dots\dots\dots (7.3)$$

The maximum power is delivered from the TEG to the external circuit when the load resistance is matched with the device internal resistance [10]. That is:

$$P_{MAX} = \frac{V^2_{OC}}{4 R_{int}} \dots\dots\dots (7.4)$$

The P_{MAX} of the fabricated TEGs was determined from operating voltages and operating currents obtained by varying the load resistance and is given in fig. 7.5. The P_{MAX} of all TEGs is listed in Table 7.2.

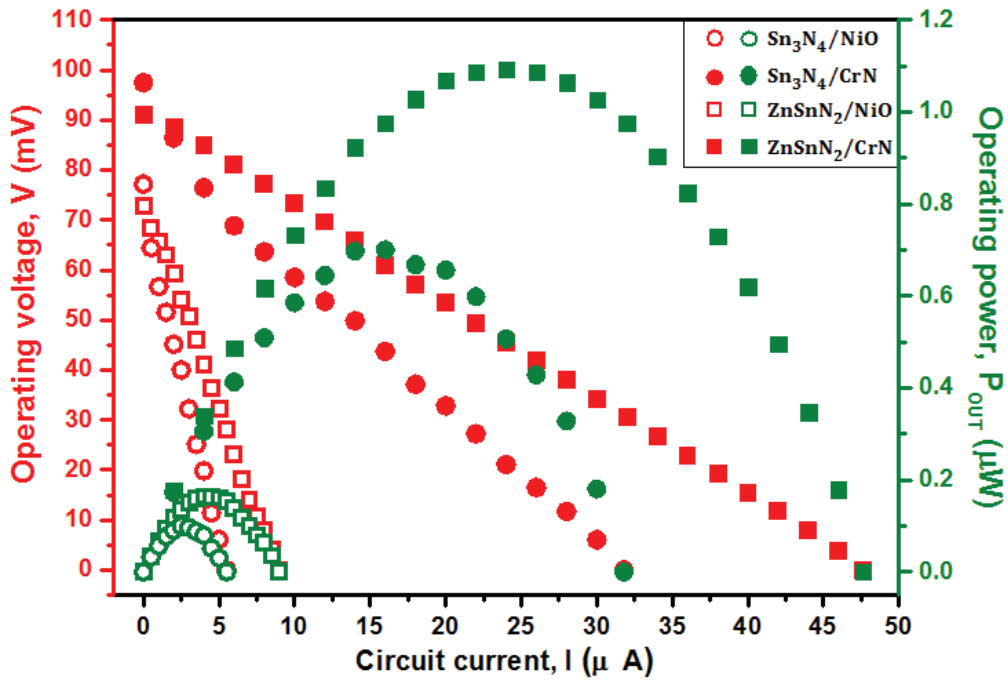


FIGURE 7.5. The variation of operating voltage and power of TEGs with circuit current

7.4 Conclusion

The TEGs made up of different couples of thin film leg materials, $\text{Sn}_3\text{N}_4/\text{CrN}$, $\text{Sn}_3\text{N}_4/\text{NiO}$, $\text{ZnSnN}_2/\text{CrN}$ and $\text{ZnSnN}_2/\text{NiO}$ were fabricated by reactive radio frequency magnetron sputtering. The dependence of temperature gradient on output power of the devices was investigated by estimating the open circuit voltage and short circuit current by varying the temperature difference across the TEGs. The aforementioned parameters were increased with temperature gradient and the maximum values were obtained at a temperature difference of 200°C . The maximum value of open circuit voltage is depended on the resultant of Seebeck coefficients of the individual p-type and n-type leg materials, hence $\text{Sn}_3\text{N}_4/\text{CrN}$ device showed the highest open circuit voltage of 97 mV. The maximum value of short circuit current greatly influenced by the internal resistance of the device which is the resistivity of the individual material and $\text{ZnSnN}_2/\text{CrN}$ device showed the highest value of $47\ \mu\text{A}$. Since the output power is the resultant of the open circuit voltage and short circuit current, the highest output power of $4.3\ \mu\text{W}$ is also shown by the $\text{ZnSnN}_2/\text{CrN}$ device with V_{OC} of 91 mV. The maximum operating power of this TEG at matched load is $1.09\ \mu\text{W}$. Hence, the evaluation of the various electrical parameters of the TEGs validated the thermoelectric properties of n-type Sn_3N_4 and ZnSnN_2 and p-type NiO and CrN thin films and stable output power of the devices made up of these thin films

References

- [1] R. Freer, A. V Powell, J. Mater. Chem. C 8 (2020) 441–463.
- [2] N. Jaziri, A. Boughamoura, J. Müller, B. Mezghani, F. Tounsi, M. Ismail, Energy Reports (article in press).
- [3] R. He, G. Schierning, K. Nielsch, Adv. Mater. Techno. 3 (2018) 1700256.
- [4] A. Montecucco, J. Siviter, A.R. Knox, Appl. Energy 123 (2014) 47-54.
- [5] B.M.M. Faustino, D. Gomes, J. Faria, T. Juntunen, G. Gaspar, C. Bianchi, A. Almeida, A. Marques, I. Tittonen, I. Ferreira, Sci. Rep. 8 (2018) 6867.
- [6] F. Cheng, Y. Hong, W. Li, X. Guo, H. Zhang, F. Fu, B. Feng, G. Wang, C. Wang, H. Qinc, Energy. 121 (2017) 545-560.
- [7] L. Kütt, J. Millar, A. Karttunen, M. Lehtonen, M. Karppinen, Renew. Sustain. Energy Rev. 98 (2018) 519–544.

- [8] I. Petsagkourakis, K. Tybrandt, X. Crispin, I. Ohkubo, T. Mori, *Sci. Technol. Adv. Mater.* 19 (2018) 836–862.
- [9] J. Chen, K. Li, C. Liu, M. Li, Y. Lv, L. Jia, S. Jiang, *Energies* 10 (2017) 1329.
- [10] X. Yu, Y. Wang, Y. Liu, T. Li, H. Zhou, X. Gao, F. Feng, T. Roinila, Y. Wang, *J. Micromech. Microeng.* 22 (2012) 105011.

SUMMARY AND FUTURE SCOPE

Contents

- 8.1 Introduction
- 8.2 Summary of the thesis
- 8.3 Future scope

This chapter presents the summary of the important results and conclusions of the studies conducted on nitride and oxide thin films for thermoelectric device applications. It also provides a precise direction for the future research works.

8.1 Introduction

The various types of energy requirements and applications are to be fulfilled to meet the needs of smart living world. While we need high power supplies for the development and economic well being of a modern society, we also need miniaturized instant low power supply especially in the age of Internet of Things and Internet of Everything [1]. Such power supplies must meet some more demands such as reliability, safety and affordability. In this regard, thermoelectric power generators have great importance since it converts waste heat into electricity having the power span from very low to high values by using miniaturized solid state devices [2]. In this thesis, we reported the power output characteristics of the thermoelectric generators (TEGs) made up of earth abundant and non-toxic semiconductor thin films. Since the output power of the TEGs is greatly influenced by the thermoelectric properties of the individual leg materials, the enhancement of thermoelectric power factor of the n- and p-type materials by advanced techniques was also investigated.

8.2 Summary of the thesis

The thesis mainly focused on the transformation of earth abundant and non-toxic nitrides and oxide semiconductor thin films as efficient n- and p-type thermoelectric materials for device applications. Initially, the compounds having the capability to be transformed as an efficient thermoelectric material were identified by the keen analysis of the crystallographic and electronic band structures and basic physical properties. The sputtering parameters for the specific properties of the thin films according to the requirements were optimized by various characterizations. The n-type of tin nitride (Sn_3N_4) and zinc tin nitride (ZnSnN_2) and p-type of chromium nitride (CrN) and nickel oxide (NiO) thin films were fabricated by reactive radio frequency magnetron sputtering and enhanced its thermoelectric power factor by advanced techniques like point defects, band convergence, resonant levels and nanostructuring. The energy conversion capability of the investigated thin films was validated by analyzing the electrical output power of the TEGs made up of these thin films. The four TEGs of different couples of the thin film materials, (1) $\text{Sn}_3\text{N}_4/\text{CrN}$, (2) $\text{Sn}_3\text{N}_4/\text{NiO}$, (3) $\text{ZnSnN}_2/\text{CrN}$ and (4) $\text{ZnSnN}_2/\text{NiO}$ were fabricated by radio frequency magnetron sputtering and the electrical output characteristics were

analyzed. The achievements of this research work have been published/communicated in peer reviewed international journals. The important results and conclusions from the present thesis can be summarized as follows.

8.2.1 Investigations of n-type thermoelectric thin films

The electronic band structure of spinel Sn_3N_4 greatly supplements the convergence of the higher conduction bands at a point with the bottom conduction band by tuning band parameters. Hence, the strategy of conduction band convergence was effectively employed to enhance the thermoelectric power factor of Sn_3N_4 thin films. This was achieved by decreasing the nitrogen gas pressure of sputtering from 4×10^{-2} mbar and 4×10^{-3} mbar during the deposition of thin films. The Sn_3N_4 thin film fabricated at lowest nitrogen gas pressure showed the highest power factor of $390 \mu\text{W}/\text{m K}^2$ at 250°C with Seebeck coefficient of $-144 \mu\text{V}/\text{K}$ and resistivity of $53.11 \mu\Omega \text{ m}$ [3].

- The Sn_3N_4 thin films changed the preferred orientation from (311) to (222) with decreasing nitrogen pressure of sputtering.
- The carrier concentration was increased and the bandgap was decreased with decreasing nitrogen pressure due to the increase in density of donor type nitrogen vacancy and tin interstitial defects.
- The enhancement in effective mass with decrease in bandgap in the absence of drastic reduction in mobility confirmed the conduction band convergence [4].
- The increased valley degeneracy originated from the conduction band convergence decoupled the interdependence of Seebeck coefficient and electrical conductivity and enhanced the thermoelectric power factor [5].
- The preferred orientation has great influence on various physical properties of the thin films.
- The experimental strategy of simultaneous control over multiple sputtering parameters can be effectively employed to tune the various physical properties of the thin films.

The defect chemistry of ZnSnN_2 greatly supports the formation of donor type defects than acceptor defects. The donor defects have significantly lower formation

energies and the corresponding energy states span from few hundreds of meV below to that of above the conduction band minimum. Hence, the resonant energy states were successfully developed in ZnSnN₂ thin films by intrinsic point defects instead of conventional resonant impurity doping. For this, the partial pressure of nitrogen during the fabrication of thin films decreases from 3×10^{-2} mbar to different values up to 1×10^{-2} mbar while the working pressure of sputtering held constant at 3×10^{-2} mbar. The ZnSnN₂ thin film exhibited the power factor of 1 mW/m K^2 at 300°C with Seebeck coefficient of $-145 \mu\text{V/K}$ and resistivity of $20 \mu\Omega \text{ m}$. The power factor is more than doubled as compared to the thin films without resonant energy states.

- The carrier concentration of ZnSnN₂ thin films was increased with decreasing nitrogen partial pressure as a consequence of the increased density of intrinsic nitrogen vacancy donor defects.
- The increase in Seebeck coefficient with carrier concentration in presence of increased resistivity and bandgap along with sharp reduction in mobility confirmed that the Seebeck coefficient is enhanced due to the formation of resonant energy states.
- The large density of states and the strong dependence of mobility on energy through energy depended relaxation time stem from the presence of resonant states enhanced the seebeck coefficient of ZnSnN₂ thin films.
- The strategy of inducing resonant levels by intrinsic point defects instead of resonant impurity doping is a simple and reliable method for thin films to improve the various physical properties.
- The earth abundant nitride thin films can be transformed as efficient thermoelectric materials by band modification using advanced techniques.

8.2.2 Investigations of p-type thermoelectric thin films

The chromium vacancies and nitrogen antisite are the most favorable intrinsic point defects in experimental samples of CrN in a nitrogen rich growth condition. The chemical potential environment to form these point defects was created by increasing the nitrogen pressure of deposition process from 1×10^{-2} to 5×10^{-2} mbar. It transformed the n-type conductivity of CrN into p-type but the variation of preferred orientation from (111) to (200) significantly decreased the mobility. The thin film

having preferred orientation along (220) exhibited remarkable improvement in conductivity resulted in the enhancement of thermoelectric power factor and the p-type CrN thin film showed a power factor of $24.43 \mu W/m K^2$ with Seebeck coefficient of $301 \mu V/K$ and resistivity of $3.71 m\Omega m$ at RT.

- The mobility of CrN thin films having (200) preferred orientation was significantly decreased due to the high planar density of (200) oriented crystallites.
- The (220) oriented p-type CrN thin films showed remarkable improvement in mobility hence, the conductivity and thermoelectric power factor was enhanced.
- The variation of mobility of charge carriers with preferred orientation can be attributed to the spreading of charge distribution in particles which was obtained from the conductive atomic force microscopy analysis.
- The type of majority carriers of CrN semiconductor was identified by the direction of current distribution in the surface charge density maps.
- The study greatly supports the investigations on p-type conductive intrinsic semiconductors of nitride thin films and physical properties of thin films having preferred orientations.

The nanocrystalline NiO thin films were successfully fabricated by reactive radio frequency magnetron sputtering. Since the crystallinity and the grain size of NiO are low even in presence of high substrate temperature due to high activation energy of its crystalline phases, the thin films of nanoparticles were fabricated by reducing the substrate temperature from $450^{\circ}C$ to different values up to $50^{\circ}C$. The quantum confinement effect originated from the reduced particle size enhanced the Seebeck coefficient and widened the optical bandgap. The nanostructured NiO thin films exhibited a four-fold enhancement in thermoelectric power factor as compared with that having larger crystallites. It attained a power factor to $83 nW/m K^2$ with Seebeck coefficient of $241 \mu V/K$ and resistivity of $700 m\Omega m$ at RT. Moreover, the quantum confinement blue shifted the optical band gap of NiO from 3.56 to 4.02 eV.

- The size of the nanoparticles in NiO thin films decreased with decreasing substrate temperature during deposition which was obtained from grain distribution mapping of atomic force microscopy.

- The quantum confinement effect transformed the variation of density of states with energy of nanocrystalline NiO thin film as a step like feature having sharp variations and hence improved the density of states energy dependence and the corresponding Seebeck coefficient.
- The quantum confinement effect concurrently enhanced the thermoelectric power factor and bandgap of NiO thin films.
- The various aspects of the nanostructuring strategy can be effectively employed for the simultaneous tuning of the multiple physical properties of thin films.

8.2.3 Thermoelectric generator characteristics

The thermoelectric generators made up of different couples of the investigated thin film leg materials, $\text{Sn}_3\text{N}_4/\text{CrN}$, $\text{Sn}_3\text{N}_4/\text{NiO}$, $\text{ZnSnN}_2/\text{CrN}$ and $\text{ZnSnN}_2/\text{NiO}$ were fabricated by radio frequency magnetron sputtering. The electrical output characteristics of the TEGs validated the energy conversion performance of the investigated n- and p-type thin films in a device form. The dependence of temperature gradient on output power of the devices was investigated by estimating the open circuit voltage and short circuit current from temperature gradient v/s current, voltage and power (ΔT -V, I and P) characteristics. The device operating voltage and operating power (P_{MAX}) as a function of electrical current (I-V and P) at matched load were estimated by varying the external load resistance.

- The maximum value of open circuit voltage was depended on the resultant of Seebeck coefficients of the individual p-type and n-type leg materials and $\text{Sn}_3\text{N}_4/\text{CrN}$ device showed the highest open circuit voltage of 97 mV.
- The maximum value of short circuit current greatly influenced by the internal resistance of the device which is the resistivity of the individual material and $\text{ZnSnN}_2/\text{CrN}$ device showed the highest value of 47 μA .
- Since the output power is the resultant of the open circuit voltage and short circuit current, the highest output power of 4.3 μW was also shown by the $\text{ZnSnN}_2/\text{CrN}$ device with V_{OC} of 91 mV. The maximum operating power of this TEG at matched load is 1.09 μW .
- The evaluation of the various electrical parameters of the TEGs validated the thermoelectric properties of n-type Sn_3N_4 and ZnSnN_2 and p-type NiO and CrN

thin films and stable thermoelectric output power of the devices made up of these thin films.

8.3 Future scope

- In this work, the thermoelectric power factor of oxide and nitride thin films were enhanced by advanced techniques like band convergence, resonant levels, point defects and nanostructuring. Since the efficiency of all these techniques has direct positive correlation with defect density, it can significantly suppress the thermal conductivity of the thin films. Moreover, the knowledge about thermal conductivity hence, the figure of merit of thin films aids to determine many performance related parameters which provide more insights in to the design and output characteristics of the thermoelectric generators. Thus, the thermal conductivity of these thin films has to be accurately investigated [6].
- The thermoelectric generators fabricated in this study exhibited low output power due to the high resistivity of chromium nitride and nickel oxide p-type thin films. The continuing effort to improve the p-type conductivity of these thin films will transformed the thermoelectric generators as good candidates for commercial low power applications [7].
- The enhancement of thermoelectric power factor of the thin films by the advanced techniques is mainly based on the modification of density of states by tuning the band parameters. Hence these modifications greatly influence the optical properties of the thin films. Moreover, in the present study, the optical property analysis was effectively employed to elucidate the precise mechanism behind the band modification. During the enhancement of thermoelectric power factor, the tin nitride and zinc tin nitride thin films exhibited bandgap narrowing and enhancement in absorption coefficient. The optimized bandgap of ~ 1.5 eV and absorption coefficient of more than $10^4/\text{cm}$ transformed the thin films as good photovoltaic materials. Hence, the fabrication of solar cells by using these thin films as absorber layer and its photovoltaic characterizations have to be performed [8].

- The thin films investigated in this study consist of n-type and p-type materials as well as it exhibited thermoelectric and photovoltaic properties concurrently. Hence these films have potential applications in hybrid photovoltaic-thermoelectric power generators. The designing and fabrication of the hybrid power generators by these thin films and the output power characterizations have to be performed [9].

References

- [1] R.A. Kishore, S. Priya, *Materials*. 11 (2018) 1-45.
- [2] R. Freer, A. V Powell, *J. Mater. Chem. C* 8 (2020) 441–463.
- [3] N.A.M. Sabeer, A. Paulson, P.P. Pradyumnan, *J. Appl. Phys.* 124 (2018) 185107.
- [4] N.A.M. Sabeer, A. Paulson, P.P. Pradyumnan, *J. Phys. Chem. Solids* 138 (2020) 109294.
- [5] N.A.M. Sabeer, A. Paulson, P.P. Pradyumnan, *AIP Conf. Proc.* 1942 (2018) 110054.
- [6] R. He, G. Schierning, K. Nielsch, *Adv. Mater. Technol.* 3 (2018) 1700256.
- [7] Y. Du, J. Xu, B. Paul, P. Eklund, *Appl. Mater. Today* 12 (2018) 366–388.
- [8] M.A. Green, *Prog. Energy* 1 (2019) 013001.
- [9] X. Wang, A. Suwardi, S.L. Lim, F. Wei, J. Xu, *npj Flex. Electron.* 19 (2020) 1–9.

